Stochastic Geometry for Modeling, Analysis and Design of Future Wireless Networks

Jing Guo

August 2016

A thesis submitted for the degree of
Doctor of Philosophy of
The Australian National University

Research School of Engineering
College of Engineering and Computer Science
The Australian National University

Declaration

The contents of this thesis are the results of original research and have not been submitted for a higher degree to any other university or institution.

Much of the work in this thesis has been published or has been submitted for publication as journal papers or conference proceedings.

The research work presented in this thesis has been performed jointly with Dr. Salman Durrani (The Australian National University), Dr. Xiangyun Zhou (The Australian National University) and Prof. Halim Yanikomeroglu (Carleton University). The substantial majority of this work was my own.

Jing Guo
Research School of Engineering,
College of Engineering and Computer Science,
The Australian National University,
Canberra, ACT 2601,
AUSTRALIA

Acknowledgments

The work presented in this thesis would not have been possible without the support of a number of individuals and organizations and they are gratefully acknowledged below:

- First of all, I would like to express my heartfelt gratitude to my supervisors and friends Drs. Salman Durrani and Xiangyun Zhou, for their guidance, support and encouragement throughout my PhD studies. Their rigor and conciseness shaped my style and improved my skills in presenting complex technical ideas in papers. It is my pleasure and honor to be their student.

- I would like to thank Prof. Halim Yanikomeroglu from Carleton University for kindly welcoming me to visit his research group for four months, i.e., Dec. 2014 to Apr. 2015. It was a valuable experience in my PhD, where I learnt about the industry perspective of future wireless communications. Prof. Halim has been very helpful during my visit to Carleton University and helped me to strengthen my research skills.

- It is my great pleasure to study in the communications group at the Research School of Engineering. I would like to thank everyone for making the group a friendly and relaxing research environment. Special thanks to Drs. Nan Yang, Wen Zhang, Profs. Parastoo Sadeghi, Rodney A. Kennedy and Thushara D. Abhayapala. I would also like to thank my colleagues Wanchun Liu, Hanchi Chen, Biao He, Yirui Cong, Xiaohui Zhou, Yifei Huang and Alice Bates for providing a friendly environment and stimulating company.

- Thanks must go to The Australian National University for providing the PhD scholarship, stipend, and a 2014 ANU Vice Chancellor's Travel Grant for supporting my conference attendance, living expenses, and Carleton University visit, respectively.

- I would like to give my most sincere gratitude to my parents for their continuous support in general. My every little success would not have been possible without their encouragement. I would like to give my special thanks to my boyfriend Xiao Li for his encouragement and understanding. Finally, I would like to thank my friends in Canberra, who provided me with a homely environment overseas.

Abstract

This thesis focuses on the modeling, analysis and design of future wireless networks with smart devices, i.e., devices with intelligence and ability to communicate with one another with/without the control of base stations (BSs). Using stochastic geometry, we develop realistic yet tractable frameworks to model and analyze the performance of such networks, while incorporating the intelligence features of smart devices.

In the first half of the thesis, we develop stochastic geometry tools to study arbitrarily shaped network regions. Current techniques in the literature assume the network regions to be infinite, while practical network regions tend to be arbitrary. Two well-known networks are considered, where devices have the ability to: (i) communicate with others without the control of BSs (i.e., ad-hoc networks), and (ii) opportunistically access spectrum (i.e., cognitive networks). First, we propose a general algorithm to derive the distribution of the distance between the reference node and a random node inside an arbitrarily shaped ad-hoc network region, which helps to compute the outage probability. We then study the impact of boundary effects and show that the outage probability in infinite regions may not be a meaningful bound for arbitrarily shaped regions. By extending the developed techniques, we further analyze the performance of underlay cognitive networks, where different secondary users (SUs) activity protocols are employed to limit the interference at a primary user. Leveraging the information exchange among SUs, we propose a cooperation-based protocol. We show that, in the short-term sensing scenario, this protocol improves the network's performance compared to the existing threshold-based protocol.

In the second half of the thesis, we study two recently emerged networks, where devices have the ability to: (i) communicate directly with nearby devices under the control of BSs (i.e., device-to device (D2D) communication), and (ii) harvest radio frequency energy (i.e., energy harvesting networks). We first analyze the intra-cell interference in a finite cellular region underlaid with D2D communication, by incorporating a mode selection scheme to reduce the interference. We derive the outage probability at the BS and a D2D receiver, and propose a spectrum reuse ratio metric to assess the overall D2D communication performance. We demonstrate that, without impairing the performance at the BS, if the path-loss exponent on cellular link is slightly lower than that on D2D link, the spectrum reuse ratio can have negligible decrease while the average number of successful D2D transmissions increases with the increasing D2D node density. This indicates that an increasing level of D2D communication is beneficial in future networks. Then we study an ad-hoc network with simultaneous

wireless information and power transfer in an infinite region, where transmitters are wirelessly charged by power beacons. We formulate the total outage probability in terms of the power and channel outage probabilities. The former incorporates a power activation threshold at transmitters, which is a key practical factor that has been largely ignored in previous work. We show that, although increasing power beacon's density or transmit power is not always beneficial for channel outage probability, it improves the overall network performance.

List of Publications

The work in this thesis has been published or has been submitted for publication as journal papers. These papers are:

Journal articles

J1. **J. Guo**, S. Durrani and X. Zhou, "Outage Probability in Arbitrarily-Shaped Finite Wireless Networks," *IEEE Trans. Commun.*, vol. 62, no. 2, pp. 699–712, Feb. 2014.

J2. **J. Guo**, S. Durrani, and X. Zhou, "Performance Analysis of Arbitrarily-Shaped Underlay Cognitive Networks: Effects of Secondary User Activity Protocols," *IEEE Trans. Commun.*, vol. 63, no. 2, pp. 376–389, Feb. 2015.

J3. **J. Guo**, S. Durrani, X. Zhou and H. Yanikomeroglu, "Outage Probability of Ad Hoc Networks with Wireless Information and Power Transfer," *IEEE Wireless Commun. Lett.*, vol. 4, no. 4, pp. 409–412, Aug. 2015.

J4. **J. Guo**, S. Durrani, X. Zhou and H. Yanikomeroglu, "Device-to-Device Communication Underlaying a Finite Cellular Network Region," submitted to *IEEE Trans. Wireless Commun.*, Oct. 2015 (revised Mar. 2016 and Aug. 2016).

The following publications are also the results from my PhD study but not included in this thesis:

Journal articles

J5. Z. Khalid, S. Durrani and **J. Guo**, "A Tractable Framework for Exact Probability of Node Isolation and Minimum Node Degree Distribution in Finite Multi-hop Networks," *IEEE Veh. Tech.*, vol. 63, no. 6, pp. 2836–2847, Jul. 2014.

J6. X. Zhou, **J. Guo**, S. Durrani and I. Krikidis, "Performance of Maximum Ratio Transmission in Ad Hoc Networks with SWIPT," *IEEE Wireless Commun. Lett.*, vol. 4, no. 5, pp. 529–532, Oct. 2015.

Conference papers

C1. **J. Guo**, S. Durrani and X. Zhou, "Characterization of Aggregate Interference in Arbitrarily-shaped Underlay Cognitive Networks," in *Proc. IEEE GLOBECOM*, Dec. 2014, pp. 961–966 (selected as one of best 50 papers at GLOBECOM 2014).

C2. C. Wang, S. Durrani, **J. Guo** and X. Zhou, "Call Completion Probability in Heterogeneous Networks with Energy Harvesting Base Stations," in *Proc. ICT*, Apr. 2015, pp. 191–197.

C3. D. Marshall, S. Durrani, **J. Guo**, and N. Yang, "Performance Comparison of Device-to-Device Mode Selection Schemes," in *Proc. IEEE PIMRC*, Aug. 2015, pp. 1536–1541.

List of Acronyms

AWGN	additive white Gaussian noise
BPP	Binomial point process
BS	base station
CDF	cumulative distribution function
CUE	cellular user
D2D	device-to-device
DRx	D2D receiver
DUE	potential D2D user in underlay D2D mode
FT	Fourier transform
ICIC	inter-cell interference coordination
IT	information transmission
i.i.d.	independently and identically distributed
i.u.d.	independently and uniformly distributed
MGF	moment generating function
PB	power beacon
PDF	probability density function
PPP	Poisson point process
PT	power transfer
PU	primary user
PU-Rx	PU receiver
PU-Tx	PU transmitter
p-DUE	potential D2D user
QoS	quality-of-service
RF	radio frequency
RLPG	reference link power gain
Rx	receiver
SINR	signal-to-interference-plus-noise ratio
SIR	signal-to-interference ratio
SNR	signal-to-noise ratio
SU	secondary user

SWIPT	simultaneous wireless information and power transfer
Tx	transmitter

Notations

$\mathcal{A}$	network region
$\lvert\mathcal{A}\rvert$	area of network region
M	number of nodes
$\mathcal{R}$	radius of disk
P_{out}	outage probability
γ_{th}	SINR or SIR threshold
α	path-loss exponent
ρ	receiver sensitivity of Rx
P	transmit power
G, H	fading power gain
$\mathcal{N}$	additive white Gaussian noise power
γ_0	average SNR
I	interference
$\mathbb{R}^2$	two-dimensional Euclidean domain
$\mathbb{N}$	set of natural numbers
$\setminus$	set exclusion operator
λ	node density
Φ	point process
$\Pr(\cdot)$	probability measure
$\Pr(\cdot\lvert\cdot)$	conditional probability measure
$f_X(x)$	PDF of a random variable X
$F_X(x)$	CDF of a random variable X
$\mathbb{E}_X\{\cdot\}$	expectation operator with respect to X
$\mathbb{E}_X^{pt}\{n,l,u\}$	n-th order partial moment of X calculated within the interval $[l,u]$
$\mathcal{L}_x(s)$, $\mathcal{L}_{f_X(x)}(s)$	Laplace transform of the PDF $f_X(x)$
$\mathcal{L}_{F_X(x)}(s)$	Laplace transform of the CDF $F_X(x)$
$\mathcal{M}_X(s)$	MGF of a random variable X with PDF $f_X(x)$
$\mu_X(n)$	n-th moment of X
$\kappa_X(n)$	n-th cumulant of X
$\mathbf{i}$	imaginary number $\sqrt{-1}$

$\mathrm{Re}\{\cdot\}$	real part of a complex-valued number
$\mathrm{Im}\{\cdot\}$	imaginary part of a complex-valued number
$\mathrm{abs}(\cdot)$	absolute value
$\mathbf{1}(\cdot)$	indicator function
$\min(\cdot,\cdot)$	the minimum value
$[f(x)]_a^b$	$f(b)-f(a)$
$\Gamma[x]$	complete Gamma function, $\int_0^\infty t^{x-1}\exp(-t)\,\mathrm{d}t$
$\Gamma[a,x]$	incomplete upper Gamma function, $\int_a^\infty t^{x-1}\exp(-t)\,\mathrm{d}t$
$\Gamma[a,x_1,x_2]$	generalized incomplete Gamma function, $\Gamma[a,x_1]-\Gamma[a,x_2]$
${}_2F_1\left[\cdot,\cdot;\cdot;\cdot\right]$	Gaussian or ordinary hypergeometric function
$\mathrm{MeijerG}[\{\cdot\},\cdot]$	Meijer G-function
$\delta(\cdot)$	Dirac function

Contents

List of Figures

List of Tables

Chapter 1

Introduction

1.1 Motivation

Recent years have witnessed the exponential growth in the number of wireless mobile devices and the resulting mobile data traffic [1]. It has been reported by Cisco that there are 7.4 billion mobile devices world wide in 2014, which will increase to 11.5 billion mobile devices in 2019 [2]. In addition, the average data traffic generated by fourth generation (4G) network is 2.2 GB per month in 2014, which is expected to increase to 5.5 GB per month in 2019 [2]. To meet this demand in the future, fifth generation (5G) networks are envisioned to provide [1, 3]:

- higher data rate (i.e., 1000$\times$ increase from 4G to 5G);
- low end-to-end latency (i.e., supporting a roundtrip latency of about 1 ms, compared to current 4G roundtrip latencies of the order of about 15 ms);
- higher energy efficiency (i.e., about 100$\times$ decreasing in Joules per bit and cost per bit for each data link);

Presently there is a broad consensus in academic and industry that these requirements simply cannot be achieved by a mere evolution of current network systems [4], e.g., strategies such as cell densification and cell shrinking resulting in small cells, will play an important part in 5G, but need to be supplemented by other solutions. As a result, novel technology directions have been envisioned for 5G. Among these novel technologies is the concept of smart devices, which is the focus of this thesis. In traditional 2G-3G-4G cellular networks, the base station (BS) infrastructure takes control of communication and has complete control over mobile devices. In 5G systems, it is expected that the devices will be endowed with intelligence. This intelligence has major implications for the modeling, analysis and design of future wireless networks.

The simplest form of intelligence is perhaps the ability to bypass BSs completely and communicate with other devices without any central control. This gives rise to the concept

of ad-hoc networks, the basic idea of which has been around for a few decades. The recent proliferation of wireless devices and technologies for short range communication (such as Bluetooth) indicates that ad-hoc networks are attractive for 5G system, especially for the development of small cell scenarios [5, 6]. In ad-hoc networks, users are equipped with wireless transceivers which can directly communicate with each other [7, 8], which implies that these smart devices are no longer under the control of BSs. Without the infrastructure set up and administration, the users can create and join networks anytime and anywhere [9].

A more sophisticated form of intelligence can be the ability to flexibly use the licensed spectrum, i.e., cognitive networks. In cognitive networks, unlicensed secondary users (SUs) access the licensed spectrum band in an efficient and opportunistic fashion, without impairing the performance of licensed primary users (PUs) [10, 11, 12, 13]. In order to achieve this, the SUs are equipped with cognitive capability so that they can adjust their operating system parameters, e.g., transmission power, frequency, modulation type, according to the surrounding wireless environment [10, 11].

Besides opportunistic accessing the spectrum band as in cognitive networks, a smart wireless device can also explore its co-location with other devices for local communication, under the control of the BS. An evolution of the concept of ad-hoc networks and cognitive networks is device-to-device (D2D) communication networks [14]. In traditional cellular networks, the communication between any two mobile devices is established by traversing through the BS or core network, even if these two mobile devices are very close to each other, which can be very inefficient if high data rate applications such as video games or virtual reality are involved. Allowing direct communication established between nearby users, under the control of the BS, is envisioned as a key aspect of smart devices in 5G networks [15, 16].

Beyond the 5G networks, smart devices are predicted to evolve even further and incorporate more sophisticated intelligence in the form of ability to harvest energy from radio frequency (RF) signals. Devices with RF energy harvesting capability can lead to the establishment of truly perpetual wireless networks, eliminating the need to replace batteries for devices. Such intelligent capability is treated as a promising solution to address the critical issue of prolonging the life time of nodes in wireless networks, especially in energy-constrained wireless networks [17, 18].

The introduction of smart devices in future wireless networks, possibly together with the requirements for such devices to operate in smaller size cells, poses significant challenges for the modeling, analysis and design of such networks. These challenges are discussed in the next subsections.

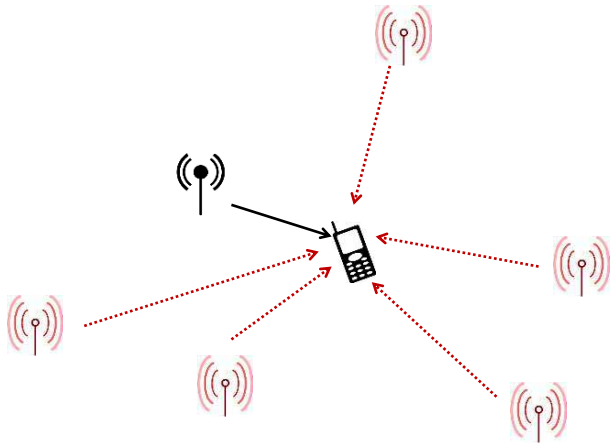

Figure 1.1: Illustration of the multiple-access network model. The desired link is connected by solid line and interfering links are connected by dashed lines.

1.1.1 Research Challenges

Consider a smart device operating in a multiple access network (i.e., a wireless network with multiple links sharing the same spectrum band), as illustrated in Figure 1.1. In such a multiple access network, a smart device can receive not only the signal from its desired transmitter (Tx), but also the unwanted signal from other Txs using the same spectrum band. These unwanted signal powers are called interference. For the purpose of correct information recovery, the signal-to-interference-plus-noise ratio (SINR) at the receiver (Rx) side should exceed a certain level. It is noteworthy that the SINR at the Rx is not merely determined by the location and surrounding environment of the Tx and Rx pair itself. The location and surrounding environment of other interfering Txs also impact the SINR. Thus the SINR is a function of the locations of all Txs, the transmit powers for all Txs and fading channels. Under such a scenario, the network performance, which is mainly determined by the SINR, becomes quite challenging, as discussed below.

1.1.1.1 Network Modeling

The first challenge for performance analysis is network modeling, i.e., how to model the physical location of smart devices, the fading channels and so on. Several analytical modeling approaches have been proposed in the literature to analyze wireless network performance, particularly large-scale cellular networks. One popular model is the Wyner model [19], in which the channel gains between the interfering BS and users are usually assumed to be constants.

The Wyner model can simplify the analysis and provide tractable analytical results in wireless networks, however since the SINR is always fixed and deterministic, sometimes it is not suitable to model certain network scenarios, for example for the case with one or two strong interferers [20, 21].

Another well-known model is the traditional grid-based model, i.e., the hexagonal grid model. This deterministic model allows for the modeling of large-scale cellular networks. However, it has been shown that in practice the locations of BSs do not exactly follow the grid-based model and this type of modeling leads to the optimistic assessment of system performance [21]. At the same time, the grid-based model cannot properly capture the network properties for those networks with inherently random topologies, such as ad-hoc networks. Additionally, it does not lead to tractable results and has to be used in conjunction with the exhaustive Monte Carlo simulations, which can be quite time consuming.

To better model the network and to avoid the exhaustive Monte Carlo simulations, the point process model was proposed in [22]. Under the point process model, the wireless network is abstracted to be a set of nodes, where the appearance at each location is subject to a certain distribution. With the help of stochastic geometry, tractable analytical expressions for the network performance in such random topologies, can be derived. The detailed discussion of the point process model and stochastic geometry will be given in Section 1.2. In this thesis, we will employ the point process model to analyze the network performance with smart devices.

1.1.1.2 Network Geometry

The second challenge that impacts the performance analysis is the network geometry. Network geometry is known as the geometric pattern formed by network devices (i.e., Txs and/or Rxs). With the stochastic geometry, the difficulty in investigating the random geometric pattern is reduced.

For analytical convenience, most works in the literature considered large-scale wireless networks (e.g., [23, 24, 25, 26, 27, 28, 29, 30, 31, 32, 33, 34, 35] in ad-hoc networks, [36, 37, 38, 39, 40] in cognitive radio networks, [41, 42, 43, 44, 45, 46, 47, 48, 49, 50] in D2D communication networks and [51, 52, 53, 54, 55, 54, 56] in energy harvesting networks), in which the locations of network devices are modeled as a homogeneous Poisson Point Process (PPP) in an infinite region. This homogeneous PPP shares some nice properties such as the stationary property where the node distribution is invariant under translation, and the isotropic property where the node distribution is rotationally invariant with respect to the origin. These give rise to the location-independent performance. For example, the typical Rx is generally assumed to be at the origin and the statistical characteristics (such as mean aggregate interference and average outage probability) derived at this typical node are the same for all nodes. This reduces

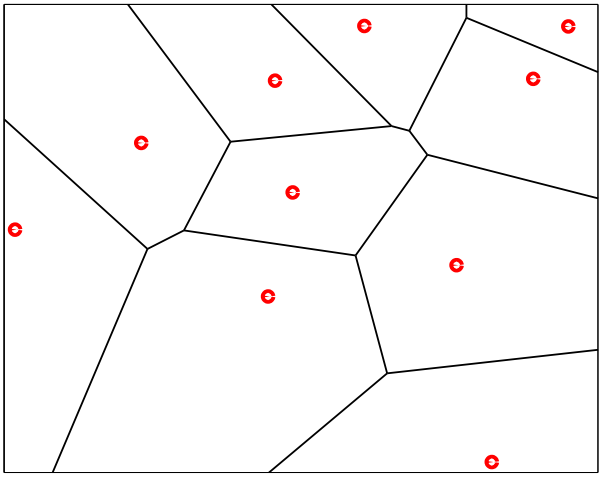

Figure 1.2: An example of the shape of Voronoi cells (• = base station).

the analysis complexity resulting from the network geometry. Some other works concentrated on the finite region [39, 57, 58, 59, 60, 61, 62, 63]. However, to utilize the isotropic property, the network region is typically assumed to be a disk and the reference node[1] is placed at the center.

In practice, the shape of the network can be arbitrary and need not be a disk only. A typical example is the shape of Voronoi cells, which is generally an arbitrarily shaped convex polygon as shown in Figure 1.2. Note that the consideration of an arbitrarily shaped network region is especially relevant for emerging ultra-dense small cell deployment scenarios [64].

When mobile devices are confined in a finite region, the network performance is strongly affected by the network geometry (e.g., the shape of the network region and the location of the reference node). For example, the nodes located close to the physical boundaries of the wireless network experience different network characteristics (such as mean aggregate interference and average outage probability) as compared to the nodes located near the center of the network. Such phenomenon is known as the boundary effect and it has been ignored by homogeneous PPP model, since infinite region is not impacted by the boundary effect. Hence, the results derived under the homogeneous PPP model cannot accurately capture the network performance in a finite region. Deriving general results in finite wireless networks is challenging because the performance metric (e.g., outage probability) is determined by the distance distribution of a node to the reference node. This distance distribution, in turn, depends on the shape of the network region as well as the location of the reference node. Unlike the homogeneous PPP

[1] Throughout the thesis, we use the words "typical/reference" to indicate the object that we are interested in and will be analyzed.

assumption, the distance distribution is the key hurdle in applying stochastic geometry to the analysis of finite wireless networks. Hence, we will come up with an algorithm, which is based on finding the overlap region of a disk and the arbitrarily shaped network region as inspired from [65, 66], to accurately compute the distance distribution for an arbitrarily shaped network region with an arbitrarily located reference node.

1.1.1.3 Network Complexity

The introduction of smart devices with intelligence, which results in the special requirements, is a key challenge and increases the network analysis complexity. This is in contrast to traditional cellular networks, where BSs play the dominant role in communication systems and are in charge of handling traffic and signaling, etc. As such, the analysis of traditional cellular networks is relatively simple.

For example, in the underlay cognitive networks, since secondary users share the same spectrum with license users, which can impact the performance of license users, the secondary users must ensure that they will not generate severe interference and the primary network can work normally [67]. With the interference threshold requirement, the locations of SUs are related to the location of the primary user, which introduces the distance-correlation to the system analysis. Similarly, in D2D communication networks, additional protocols are needed to protect the BS and D2D users from the interference between cellular users and D2D users. In energy harvesting networks, it is important to ensure that the energy can activate the energy harvesting circuit, which has been ignored in most works for analytical convenience. The incorporation of such aspects into the network model increases the overall complexity and makes performance analysis very complicated.

This thesis aims to address the challenges identified above and apply the stochastic geometry to model, analyze and design future wireless networks (i.e., ad-hoc networks, cognitive networks, D2D communication networks and energy harvesting networks). In the remainder of this chapter, we first provide background information on the point process model and stochastic geometry. Then we discuss relevant existing results in the literature on the networks with smart devices. Finally, the scope and contributions of the thesis are summarized.

1.2 Background

1.2.1 Point Process Model and Stochastic Geometry

Point process models circumvent the inadequacy of the existing network models (e.g., Wyner model and deterministic grid-based model), when dealing with topological randomness. In a point process model, the network is abstracted to be a collection of nodes residing in a certain

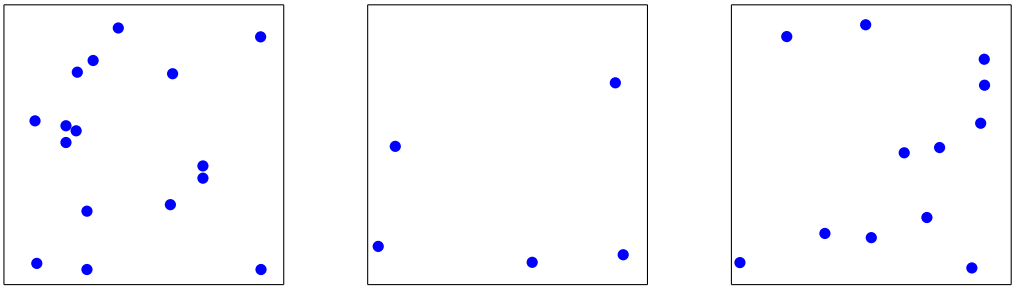

Figure 1.3: Illustration of a homogeneous PPP in a square region for three different realizations.

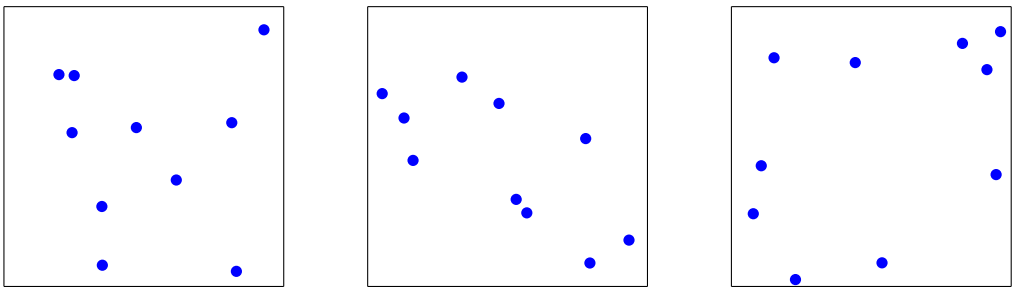

Figure 1.4: Illustration of a uniform BPP in a square region for three different realizations.

place (generally in two-dimensional space), which comprises of Txs and Rxs. The locations of these nodes are not fixed but subject to uncertainty [22]. From the modeling perspective, although it is reasonable to assume that users are randomly located due to their mobility, the BSs' locations are generally fixed and it is less acceptable to assume that the locations of BSs come from a point process. However, as established in [68], the results from the point process model are quite accurate when compared to an actual 4G network deployment. More importantly, compared with previous models, the point process model allows for the computation of tractable results, which can provide design insights.

Clearly, in the point process model, the performance metrics (i.e., interference and SINR) are changing from one realization to another realization. As a result, the distribution or average result of them can better highlight their characterizations. Stochastic geometry, as a powerful mathematical tool dealing with random spatial patterns, permits the computation of the distribution and spatial average of such quantities [21]. Note that the spatial average indicates that the average is taken over a large number of realizations of nodes, whose occurrences follow certain probabilities [32, 69].

In the stochastic geometry analysis, there are several types of point processes that have been employed in the literature to capture the main features of wireless networks. The two most famous processes are the Poisson Point Process and Binomial Point Process (BPP) [70].

In the PPP, a set of nodes is randomly and independently distributed in an infinite region and the number of nodes inside a compact region is following the Poisson distribution. When

the node density is constant (i.e., nodes are randomly, independently and uniformly distributed (i.u.d.) in the entire region), the PPP is known as the homogeneous PPP. An example of a homogeneous PPP is given in Figure 1.3. Note that for any disjoint area in a PPP, the number of nodes is independent. This independence property in stochastic geometry also brings about other nice properties and well-known theorems, which makes the PPP easy to analyze and provides tractable results [70, 71].

The BPP model is closely related to the PPP [71]. In the BPP, rather than a random number of nodes, there are a fixed number of nodes that are randomly and independently distributed within a finite region. Similarly, when the node density is constant, the general BPP reduces to the uniform BPP. An example of a uniform BPP in a square region is given in Figure 1.4. The BPP is an appropriate model for the finite region when the number of nodes is known. For example, a fixed number of sensor nodes are dropped from an aircraft [21]. Similar to the PPP model, it maintains the analytical tractability of the analysis. In this thesis, both the PPP and BPP will be considered.

1.2.2 Key Performance Metrics

In the stochastic geometry analysis, the SINR (or signal-to-interference ratio, SIR, under interference-limited scenarios) is the most fundamental and important metric to evaluate the network performance, as it is closely related to the channel capacity according to Shannon's theorem. In the following, we define two basic SINR-related performance metrics or quantities that are employed in this thesis.

- **Outage probability:** It is the probability that the SINR at the Rx is below a certain threshold γ_{th}. The mathematical definition of outage probability is given by $P_{\text{out}} = \Pr\left(\text{SINR} < \gamma_{\text{th}}\right)$. It can also be viewed as the cumulative distribution function (CDF) of SINR.

- **Moment generating function of aggregate interference:** It is an alternative interpretation of aggregate interference's distribution. Its mathematical formulation is given as $\mathcal{M}_I(s) = \mathbb{E}_I[\exp(-sI)]$, where the I is aggregate interference from all interferers sharing same spectrum. The general expressions of $\mathcal{M}_I(s)$ under different point processes are available in [32, 71]. When it is not easy to find the distribution of the aggregate interference, the moment generating function (MGF) can provide other available information. For example,

  - The statistics of aggregate interference, such as the mean and variance. The MGF

is related to the n-th cumulant of the aggregate interference by

$$\kappa_I(n) = (-1)^n \left. \frac{d^n \ln I}{ds^n} \right|_{s=0}. \tag{1.1}$$

– The outage probability. When the reference link experiences Rayleigh fading, it is well known that the outage probability can be derived using MGF [70], i.e.,

$$P_{\text{out}} = \Pr\left(\frac{G_0 \bar{P}}{I + \mathcal{N}} < \gamma_{\text{th}}\right) = 1 - \exp\left(-\frac{\gamma_{\text{th}} \mathcal{N}}{\bar{P}}\right) \mathcal{M}_I\left(\frac{\gamma_{\text{th}}}{\bar{P}}\right), \tag{1.2}$$

where $\bar{P}$ is average received power from the typical Tx, G_0 is the fading power gain on the reference link and $\mathcal{N}$ is the additive white Gaussian noise (AWGN) power.

In this thesis, we will use the outage probability and the MGF of the aggregate interference to analyze the effect of system parameters and the network performance.

1.2.3 Techniques for Performance Analysis

As summarized in [21], there are generally five techniques used in the literature to analyze the network performance, when dealing with the point process model. These five techniques are listed as follows [21]:

Technique 1: Resort to Rayleigh fading assumption

By assuming that the reference link experiences Rayleigh fading, the outage probability can be directly linked to the MGF of the aggregate interference as shown in (1.2). The computation of MGF is relatively easy compared to the computation of the distribution of interference, through exploiting the properties of point process models.

Technique 2: Resort to dominant interferers by region bounds or nearest n interferers

Rather than including all interferers, a lower bound on the outage probability can be derived by only considering the dominant interferers. This kind of technique can reduce the complexity of the analysis.

Technique 3: Inversion

The distribution function of the interference can be derived using the inverse Fourier transform of the Fourier transform (FT) of the interference's distribution. Note that the MGF of the interference $\mathcal{M}_I(s)$ is closely related to the FT of the distribution of the interference $\mathcal{L}_I(s)$. Because, from the definition,

$\mathcal{M}_I(s) = \mathbb{E}_I[\exp(-sI)]$, $s \in$ real number, while $\mathcal{L}_I(s) = \mathbb{E}_I[\exp(-sI)]$, $s \in$ complex number.

Technique 4: Resort to the approximation of the probability density function (PDF) of the aggregate interference

When it is not easy to find the closed-form distribution for the aggregate interference, the distribution can be approximated by one of the known distributions instead. The parameters for certain distribution are generally determined by the statistics (i.e., moments and cumulants).

Technique 5: Resort to the Plancherel-Parseval theorem

This technique is an alterative way to find the exact distribution of the interference through integrating FT of interference's distribution, based the Plancherel-Parseval theorem [72].

The techniques adopted and developed in this thesis advance the knowledge in the domain of **Techniques 1** and **3**. In particular, for **Technique 1**, rather than limiting the fading on reference link being Rayleigh fading, we extend it to the more general fading scenario. The details will be presented in Chapters 2, 3 and 4.

1.3 Related Work

In this section, we review the relevant work in the literature on the performance analysis of smart device networks using stochastic geometry, divided into four main categories, i.e., ad-hoc networks, cognitive networks, D2D communication networks and energy harvesting networks.

1.3.1 Ad-hoc Networks

In ad-hoc networks, users are free to move and this property renders the point process model as suitable for this network. There has been a lot of works done in the literature to investigate the performance of ad-hoc networks from different perspectives. For example, the distribution of interference and/or outage probability in large scale ad-hoc networks were studied in [23, 24, 25, 26], especially the exact PDF of the aggregate interference under the path-loss exponent $\alpha = 4$ and the location of interfering nodes being the homogeneous PPP was derived in [23] for deterministic fading gain and [24] for Rayleigh fading channel model. This aggregated interference distribution was shown to be the Lévy distribution. The transmission capacity, which measures the spatial intensity of successful transmissions per unit area, subject to a constraint on the outage probability, was investigated in [27, 28, 29]. Therein, the upper

and lower bounds on the transmission capacity for wireless ad-hoc networks without/with random channels were derived in [27, 28], respectively. The basic mathematical framework was provided in [29] to investigate the outage probability and transmission capacity. Their work has been further extended to incorporate different aspects such as the interference cancellation technology in [30] and spatial diversity in [31]. Other works targeted to improve the ad-hoc network performance with the consideration of opportunistic medium access scheme [73], and power control [33, 34, 35], and so on. Note that afore-mentioned works considered the large scale wireless network (i.e., infinite network region) and homogeneous PPP for the sake of analytical convenience and tractability.

However, in practical wireless networks, the network region tends to be arbitrarily shaped. Unlike infinite wireless networks, deriving general results on the outage probability in finite wireless networks is a very difficult task because the outage performance depends strongly on the shape of the network region as well as the location of the reference receiver.

Since it is difficult to derive general results on the outage probability in arbitrarily shaped finite wireless networks, most prior works focused on a specific shape (such as a disk) and computed the outage probability at a specific location (such as the center of the network region). A few recent studies presented outage characterizations at the center of a uniform BPP network with more general shapes [57, 58, 59]. Specifically, the analytical expression for the moment generating function of the aggregate interference seen at the center of a uniform BPP network was presented in [57]. The results were extended for the case of spatial multiplexing with the maximal ratio combining and zero forcing schemes in [59]. Using the PDF of the nearest neighbor in a uniform BPP, a lower bound on the outage probability at the center of the wireless network for a simple path-loss model was computed in [58]. The exact closed-form outage probability in a class of networks with isotropic node distribution (i.e., the node distribution is invariant under rotation) was derived in [74]. For finite networks, the results in [74] can only be applied to very limited cases preserving the isotropic node distribution, such as a disk-shaped network. The outage probability at an arbitrary location of an arbitrarily shaped finite wireless network was studied in [75]. This work focused on deriving closed-form expressions for the *conditional* outage probability, which is conditioned on the locations of all the interfering nodes in the network. For the (unconditional) outage probability averaged over the spatial distribution of nodes, the authors in [75] presented the analytical result for the special case of an annular-shaped network with the reference receiver at the center. For other shapes and receiver locations, the authors in [75] suggested the use of Monte Carlo simulations to compute the outage probability. Therefore, it is still largely an open research problem to find general frameworks for deriving the outage probability at an arbitrary location of a finite wireless network with an arbitrary shape. This thesis aims to analyze the performance of ad-hoc networks in arbitrarily shaped finite regions, which is relevant for small cell deployments in

5G networks.

1.3.2 Cognitive Networks

Cognitive networks allow unlicensed secondary users to access the spectrum of licensed primary users in an intelligent way. Depending on the spectrum access strategy, there are three main cognitive radio network paradigms: interweave, overlay and underlay [67][2].

In *interweave cognitive networks*, SUs are not allowed to cause any interference to PUs. Thus, SUs must periodically sense the environment to detect spectrum occupancy and transmit opportunistically only when PUs are silent [79, 80]. Ideally, the PU will not receive any interference from SUs. When the SU fails to detect the PU in certain spectrum bands, it is however possible that the PU is interfered by these SUs. Thus several papers studied the network performance in the case of the appearance of miss-detection in interweave case. For example, the statistical quantities of the aggregate interference from SUs were analyzed in [36] under infinite network region assumption and in [60] with disk network region assumption. By considering Nakagami-m fading channels and disk region, it was found in [61] that the distribution of the aggregate interference from SUs can be approximated by a Gamma distribution. The outage probability at the PU with different sensing techniques was further investigated in [37].

In *overlay cognitive networks*, there is tight interaction and active cooperation between PUs and SUs. Thus, SUs use sophisticated signal processing and coding to maintain or improve the PUs' transmissions while also obtaining some additional bandwidth for their own transmissions [81, 82, 83].

In *underlay cognitive networks*, SUs can concurrently use the spectrum occupied by a PU. Compared to overlay cognitive networks, underlay cognitive networks do not require SUs to facilitate the transmissions of PUs [67]. Compared to interweave cognitive networks, underlay cognitive networks have better spectrum efficiency since the concurrent transmissions are allowed. Hence, we focus on underlay cognitive networks in this work. Note that the SUs in underlay paradigm have to guarantee that the interference at the PU is below some acceptable threshold [84, 85]. That is to say, SUs must know the signal strengths to PUs and are also allowed to communicate with each other in order to sense how much interference is being created to PUs [86]. Thus, it is very important to study the interference arising from the SUs to a PU for underlay cognitive networks. The interference and outage in underlay cognitive networks have been recently investigated in the literature [38, 39, 62, 63], especially from the perspective of reducing the interference at PU. Specifically, the aggregate interference at a typical PU and a typical SU inside an infinite area cognitive network, taking the exclusion region around PUs into account, were presented in [38] and bounds on the outage probability were

[2]Note that hybrid spectrum access strategies, appropriately combining the above three paradigms, have also been proposed [76, 77, 78].

also derived. The closed-form results for the MGF of the aggregate interference and the mean interference at an annulus-center-located PU were derived in [39]. A framework for characterizing the aggregate interference in cognitive networks was proposed in [62] for the disk region under Rayleigh fading channel assumption. Therein, closed-form results were obtained for the special case that the path-loss exponent is 2 or 4 with an arbitrary location of PU inside a disk region. However, in practice the shape of network can be arbitrary and need not be a disk only. This is especially relevant for emerging ultra-dense small cell deployment scenarios [64]. In addition, the PU may be located anywhere inside the network region. When SUs are confined within an arbitrarily shaped finite region, the aggregate interference and the outage probability are strongly influenced by the shape of region and the position of the PU. In this context, a method of calculating the approximation of n-th cumulant inside a non-circular region by dividing the areas into infinitesimal circular sections was suggested in [63] but no explicit formulation was provided. Therefore, it is still largely an open research problem to find general frameworks for analyzing the interference and outage probability in arbitrarily shaped finite underlay cognitive networks.

For underlay cognitive networks, there are several ways proposed in the literature to control the interference generated by SUs in order to satisfy the interference threshold, e.g., using multiple antennas to guide the SU signals away from the PU [86], using resource (i.e., rate and power) allocation among the SUs [84] or using spread spectrum techniques to spread the SU signals below the noise floor [85]. Perhaps the simplest solution to control the interference generated by the SUs is to employ the SU activity protocols, i.e., to simply limit the number of active SUs [38, 39, 63]. In this context, an exclusion or guard zone around PUs was considered in [38, 39] and SUs within the exclusion/guard zone are not allowed to transmit. A threshold-based protocol was proposed in [63], where the activity of each SU depends on the instantaneous power received at the SU from the PU. Note that if no activity constraint is imposed on SUs then this is equivalent to the well-studied case of wireless ad-hoc networks where all users can transmit [57, 87, 88]. In this thesis, we aim to study the network performance (both primary network and secondary network) in an arbitrarily shaped region with the incorporation of SU activity protocols.

1.3.3 Device-to-Device Communication Networks

D2D communication is generally established under the control of the BS, which is fundamentally different from ad-hoc networks and cognitive radio networks [89]. In cellular networks with D2D communication, the cellular and D2D users can share the spectrum resources in two ways: *in-band* where D2D communication utilizes the cellular spectrum and *out-of-band* where D2D communication utilizes the unlicensed spectrum [90]. In-band D2D communica-

tion can be further divided into two categories: *overlay* where the cellular and D2D users use orthogonal (i.e., dedicated) spectrum resources, and *underlay* where D2D users share the same spectrum resources occupied by cellular users, which will be considered in this thesis.

Because of the different types of users and the spectrum sharing in D2D communication, the analysis of network performance becomes challenging, especially in underlay case. Some papers have recently examined the interference and outage performance in D2D communication. For example, the spectrum sharing in both in-band and out-band scenarios was considered in [41], where the analytical expressions of the outage probability at a cellular user and a D2D user were derived. Then the work was extended to study the resource optimization in [42], the multicast of D2D communication in [43] and power control in [49]. A concept of operational region was proposed in [44] and it is defined as a set of system parameters for which the incorporation of a D2D mode can increase the network performance. The outage probability by considering the mode selection scheme was studied in [45, 46]. Therein, a user decides to operate in cellular mode or D2D mode according to the pilot signal strength received from its nearest BS in [45], while in [46], the model selection decision was based on the comparison of the cellular link and D2D link. The effect of mode selection schemes was then compared in [47]. In [48], the analytical expressions of outage probabilities were derived by considering Rician fading channel. Additionally, a framework to model the interference in D2D communication was proposed in [50], where the closed-form approximation results for SIR were obtained.

For traditional cellular networks with universal reuse frequency, where the same spectrum is used among all the cells, the inter-cell interference coordination (ICIC) and its enhancements can be used to effectively manage the inter-cell interference. Thus, dealing with intra-cell interference in D2D-enabled cellular networks becomes a key issue. Existing works have proposed many different approaches to manage the interference, which have been summarized in [15]. The main techniques include: (i) Using network coding to mitigate interference [91]. However, this increases the implementation complexity at the users. (ii) Using interference aware/avoidence resource allocation methods [48, 92, 93, 94, 95]. These can involve advanced mathematical techniques such as optimization theory, graph theory or game theory. (iii) Using mode selection which involves choosing to be in underlay D2D mode or not. In this regard, different mode selection schemes have been proposed and analyzed in infinite regions using stochastic geometry in [41, 44, 46, 47, 50]. These schemes generally require knowledge of the channel between cellular and D2D users. (iv) Using other interference management techniques such as advanced receiver techniques, power control, etc. [49, 96, 97, 98, 99].

Since D2D communication is envisaged as the short-range direct communication between nearby users, it is also very important to model D2D-enabled cellular networks as finite regions as opposed to infinite regions. The consideration of finite regions allows modeling of

the location-dependent performance of users (i.e., the users at cell-edge experience different interference compared with users in the center). In this regard, it is a highly challenging open problem to analytically investigate the intra-cell interference in a D2D-enabled cellular network and the performance of underlay D2D communication when users are confined in a finite region.

This thesis aims to investigate the outage probability at the BS and a typical D2D user, and the spectrum utilization for D2D communication in a finite cellular network region, where a mode selection scheme is included to minimize the intra-cell interference.

1.3.4 Energy Harvesting Networks

For a network with simultaneous wireless information and power transfer (SWIPT), the system can perform two functions at the same time, namely i) information transmission and ii) power transfer (i.e., devices harvest energy from radio frequency signal). The concept of SWIPT was first proposed in [100, 101] and it has emerged as an attractive solution to power devices in future wireless networks [102, 103]. There are currently three architectures for SWIPT [103]: integrated, closed-loop and decoupled.

In *integrated SWIPT*, information and power are extracted from the same signal transmitted by a base station. Some papers have employed the integrated SWIPT for cellular, ad-hoc, relay, cooperative and other communication scenarios. In the context of stochastic geometry, a cooperative network with multiple resources and sinks and one energy harvesting relay was considered in [51] and the outage probability was characterized, where the cooperation among users was modeled as a canonical game. This work was then extended to [104] by involving the multiple relays scenario and different relay schemes. The outage probability and the average harvested energy inside a large scale network with non-cooperative/cooperative relay schemes were investigated in [52], where relays receive energy and information from Txs. The authors in [53] formulated the feasibility problem of SWIPT in small cell networks and analyzed the feasibility in special and practical scenarios.

In *closed-loop SWIPT*, the downlink from BS to users is utilized for power transfer (P-T), while the uplink is used for information transmission (IT). As this structure involves the distance correlation of uplink and downlink, the analysis was mainly concentrated on the performance optimization with fixed location configuration, e.g., see [105][106] and references therein.

In *decoupled SWIPT*, traditional wireless networks are overlaid with special facilities to provide dedicated PT, such as the power beacons (PBs) which do not require backhaul links. There are several papers that studied the network performance using stochastic geometry [54, 55, 56]. Specifically, in [54] the authors considered a cognitive radio network, where SUs are

powered by PUs. Using the Markov-chain model, the outage probability at both PU and SU, under steady state, was derived. The feasibility of deployment of PBs for powering a cellular network, subject to certain outage constraint on the uplink data transmission, was analyzed in [55]. In [56], the worst-case study for both power and transmission outage probabilities was performed in a sensor network. This sensor is powered by ambient RF energy sources under the free space scenario, and then transmit information to data sink.

Among these possible structures of SWIPT, although decoupled SWIPT requires an additional infrastructure in the form of PBs, no backhaul links are required for PBs and the resultant low cost make it suitable to support efficient power transfer by the dense deployment of PBs [102, 103]. Hence, we focus on the decoupled structure in this thesis. To the best of our knowledge, the outage probability of ad-hoc networks with decoupled SWIPT has not yet been derived in the literature.

Additionally, for analytical simplicity, a common assumption made in previous work (i.e., [17, 51, 52, 93, 104, 105, 106, 107]) is that they did not take into account the power receiver activation threshold and the power outage probability. Therein, the power receiver activation threshold is known as the minimum RF energy required to activate the energy harvesting circuit and power outage is the event where the harvested energy cannot activate the energy harvesting circuit. This kind of assumption is not realistic especially in the context of point process modeling, where the received power is a random variable and generally has a large dynamic range. Ignoring the power outage probability in analysis can lead to the incomplete or even inaccurate characterization of such smarter device's performance. Thus, it is necessary to incorporate this factor into system set-up. A few papers have considered the minimum required RF energy in the system model and formulated the power outage probability. For example, the authors in [54] define the charging area as disk regions formed around the primary users and only the secondary user entering these region can perform energy harvesting. Otherwise, the secondary user without charging cannot transmit information. The power outage probability defined in [55] measures the chance of the harvested power at the mobile user being insufficient to support its transmission. And it is treated as a controlled parameter set to zero or a sufficiently small value to ensure uninterrupted transmission (and hence interference) from mobile users. The power outage probability in [56] is defined as the event that the received power at the single sensor is less than a threshold under the free space environment. In this thesis, we aim to analyze the outage performance (including both power outage and channel outage) in ad-hoc networks with decoupled SWIPT by considering practical factors (i.e., power receiver activation threshold).

1.4 Thesis Overview and Contributions

The main focus of the thesis is on the modeling, analysis and design of future wireless networks using stochastic geometry. In particular, we consider ad-hoc networks, cognitive networks, device-to-device communication networks and energy harvesting networks as examples of smart device networks with different level of device intelligence. In the first half of the thesis we use uniform BPP model and study the arbitrarily shaped ad-hoc and cognitive networks. In the second half of the thesis, we use PPP model and study D2D communication networks in disk shaped finite region and energy harvesting networks in infinite region. The specific contributions of each chapter are detailed below:

Chapter 2-Outage Probability in Arbitrarily Shaped Finite Ad-hoc Networks

Chapter 2 focuses on the outage probability analysis for a reference Tx-Rx link in the presence of M interferers and additive white Gaussian noise in a finite wireless ad-hoc network. We present analytical frameworks for computing the outage probability at an arbitrary location in an arbitrarily shaped finite wireless network. The outage probability is spatially averaged over both the fading distribution and the possible locations of interferers. The spatial averaging means that the outage probability is not tied to a particular realization of the network and the channel conditions. Specifically, we make the following contributions:

- We propose two general frameworks for the exact calculation of the outage probability in arbitrarily shaped finite wireless networks in which the reference Rx can be located anywhere.
  - The first framework, named the moment generating function-based (MGF-based) framework, is based on the numerical inversion of the Laplace transform of the CDF of an appropriately defined random variable (related to the SINR at the reference Rx). It is inspired from the mathematical techniques developed in [108, 109] and is valid for any spatial node distribution and any fading channel distribution. To the best of our knowledge, this is the first time that such an approach has been applied in the context of finite wireless networks.
  - The second framework, named the reference link power gain-based (RLPG-based) framework, exploits the distribution of the fading power gain between the reference Tx and Rx. It is based on the combination and generalization of the frameworks proposed in [57, 75] and is valid for any spatial node distribution and a general class of fading channel distribution proposed in [31].

- In order to demonstrate the use of the proposed frameworks, we consider the case where nodes are independently and uniformly distributed in a finite wireless network, with the node locations modeled by a uniform BPP. The fading channels between all links are assumed to be independently and identically distributed (i.i.d.) according to a Nakagami-m distribution. We use the probability density function of the distance of a random node from the reference Rx in uniform BPP networks [65] to accurately capture the boundary effects in the two frameworks.

  - We demonstrate the use of the two frameworks in evaluating the outage probability for the important case of a reference Rx located anywhere in a disk region. We show that the known outage probability results in the literature for the disk region arise as special cases in our two frameworks.
  - We further consider the case of an arbitrary located reference Rx in a convex polygon region and present an algorithm for accurately computing the outage probability. This fundamentally extends the prior work dealing with the outage probability analysis in finite wireless networks.
  - We show that the impact of boundary effects in finite wireless networks is location-dependent and is enhanced by an increase in the $m_0 = m$ value for Nakagami-m fading channels or an increase in the path-loss exponent. We also show that due to the boundary effects, the outage probability using PPP model does not provide any meaningful bounds for the outage probability in an arbitrarily shaped finite region. This highlights the importance of the proposed frameworks, which allow accurate outage probability computation for arbitrarily shaped finite wireless networks.

The results in this chapter have been presented in [88], which is listed again for ease of reference:

J1. **J. Guo**, S. Durrani and X. Zhou, "Outage Probability in Arbitrarily-Shaped Finite Wireless Networks," *IEEE Trans. Commun.*, vol. 62, no. 2, pp. 699–712, Feb. 2014.

Chapter 3-Performance Analysis of Arbitrarily Shaped Underlay Cognitive Networks: Effects of Secondary User Activity Protocols

In Chapter 3, we propose a general framework for analyzing the performance of arbitrarily shaped underlay cognitive networks, with arbitrary location of the PU and different SU activity protocols. We make the following major contributions:

- We utilize cooperation among SUs in underlay cognitive networks to come up with a cooperation-based SU activity protocol. This protocol utilizes the local information ex-

change among SUs and includes the threshold-based protocol as a special case. We derive approximate yet accurate expressions for the MGF and the n-th cumulant of the aggregate interference from SUs with the cooperation-based protocol.

- We derive the general expressions for the MGF and n-th cumulant of the aggregate interference at an arbitrarily located PU inside an arbitrarily shaped region for the existing SU activity protocols. We show that many existing closed-form results in the literature for the interference analysis in the primary network can be obtained as special cases in our framework. In addition, we derive a closed-form result for the average number of active SUs. To the best of our knowledge, this is the first time that such a result has been obtained in the literature for the case of underlay cognitive network.

- We study the average number of active SUs for the different SU activity protocols, subject to a given outage probability constraint at the PU. We show that the guard zone protocol supports the highest number of active SUs, followed by the proposed cooperation-based protocol and then the threshold-based protocol. The advantage of the cooperation-based protocol over the guard zone protocol is that it relies on the SUs only knowing the instantaneous signal strengths to the PUs.

The results in this chapter have been presented in [110], which is listed again for ease of reference:

J2. **J. Guo**, S. Durrani, and X. Zhou, "Performance Analysis of Arbitrarily-Shaped Underlay Cognitive Networks: Effects of Secondary User Activity Protocols," *IEEE Trans. Commun.*, vol. 63, no. 2, pp. 376–389, Feb. 2015.

Chapter 4-Device-to-Device Communication Underlaying a Finite Cellular Network Region

In Chapter 4, we model the cellular network region as a finite size disk region and assume that multiple D2D users are confined inside this finite region, where their locations are modeled as a PPP. The D2D users share the uplink resources occupied by cellular users. In this work, we do not consider the inter-cell interference and assume that it is effectively managed by the inter-cell interference coordination scheme. Since D2D users are allowed to share the cellular user's spectrum (i.e., underlay in-band D2D paradigm), the overall network performance is governed by the intra-cell interference. Hence, we focus on the intra-cell interference. In order to ensure quality-of-service (QoS) at the BS and to manage the intra-cell interference at the BS, we consider a mode selection scheme, as inspired from [111, 112], which allows a potential D2D user to be in underlay D2D mode according to its average interference generated

to the BS. In order to provide quality-of-service at the D2D users, we assume that a successful transmission occurs only if the signal-to-interference ratio at the D2D receiver is greater than a threshold. The main contributions of this work are as follows:

- Using the stochastic geometry, we derive approximate yet accurate analytical results for the outage probability at the BS and a typical D2D user, as summarized in Propositions 2 and 3, by assuming Nakagami-m fading channels, a path-loss exponent of 2 or 4 for D2D link and the full channel inversion power control (i.e., the intended receiver (BS or D2D user) has the minimum required received power which is known as the receiver sensitivity). The outage probability at the D2D user highlights the location-dependent performance in a finite region.

- Based on the derived outage probability at the D2D user, we propose and analyze two metrics to evaluate the overall quality of underlay D2D communication, namely the *average number of successful D2D transmissions*, which is the average number of successful transmissions for underlay D2D users over the finite network region, and the *spectrum reuse ratio* which is defined as the average fraction of underlay D2D users that can transmit successfully in the finite region. Using the derived analytical expressions, which are summarized in Propositions 2, 3, 4, 5, 6, we investigate the effects of the main D2D system parameters on these two metrics under the constraint of achieving certain QoS at the BS.

- Our numerical results show that when the D2D receiver sensitivity is not too small compared to the receiver sensitivity of BS, the average number of successful D2D transmissions over the finite network area increases, while the spectrum reuse ratio decreases with increasing D2D user's node density. However, if the path-loss exponent on the cellular link is slightly lower than the path-loss exponent on the D2D link, then the spectrum reuse ratio can have negligible degradation with the increase of node density. This is important since an increasing level of D2D usage is expected in future networks and our numerical results help to identify scenarios where increasing D2D node density is beneficial to underlay D2D communications, without compromising on the cellular user's performance.

The results in this chapter have been presented in [113], which is listed again for ease of reference:

J3. **J. Guo**, S. Durrani, X. Zhou and H. Yanikomeroglu, "Device-to-Device Communication Underlaying a Finite Cellular Network Region," submitted to *IEEE Trans. Wireless Commun.*, Oct. 2015 (revised Mar. 2016 and Aug. 2016).

Chapter 5-Outage Probability of Ad-Hoc Networks with Wireless Information and Power Transfer

Chapter 5 investigates the outage probabilities in a wireless ad-hoc network overlaid with power beacons. Particularly, the transmitter nodes are wirelessly powered by PBs and adopt the harvest-then-transmit protocol [102] with variable transmit power according to the amount of harvested power, i.e., Txs use the aggregate received power from PBs to transmit their data to their desired receiver node. The novel contributions are:

- We adopt a realistic model for wirelessly powered Tx nodes. Specifically, a power receiver activation threshold at Txs is incorporated into the system model to account for the minimum RF energy required to activate the energy harvesting circuit, and a maximum transmit power is also set at the Txs to account for the real power amplifier rating.

- By modeling the locations of PBs and Txs as independent homogeneous PPPs, we formulate the total outage probability at a typical Rx node, which is the combination of the power outage probability and the channel outage probability. In the proposed formulation, the newly defined power outage probability measures the probability that the received power at a typical Tx is less than a power receiver activation threshold, causing it to be inactive and the desired Rx to be in outage. The channel outage probability is defined as the probability that the SINR at a typical Rx is below a certain threshold.

- Assuming the path-loss exponent $\alpha = 4$, we derive the analytical expressions for the power outage probability, channel outage probability and total outage probability. Simulation results confirm the accuracy of the derived expression. The results provide design insights into the effect of system parameters on the outage probability of ad-hoc networks with decoupled SWIPT. When the node density for Txs is low, decreasing the power receiver activation threshold can improve the total outage probability. Moreover, increasing the power beacon density and the power beacon transmit power enhances the total outage performance.

The results in this chapter have been presented in [114], which is listed again for ease of reference:

J4. **J. Guo**, S. Durrani, X. Zhou and H. Yanikomeroglu, "Outage Probability of Ad Hoc Networks with Wireless Information and Power Transfer," *IEEE Wireless Commun. Lett.*, vol. 4, no. 4, pp. 409–412, Aug. 2015.

Finally, Chapter 6 gives a summary of results presented and suggestions for future research work.

Chapter 2

Outage Probability in Arbitrarily Shaped Finite Ad-hoc Networks

As the primitive form of a network with smart devices, the users in ad-hoc networks act independently and are not under the control of the BS. In this chapter, we focus on the outage probability at an arbitrarily located reference point in an arbitrarily shaped ad-hoc network region, which is largely different from previous works where the network region is assumed to be infinite. We firstly investigate whether there exist general frameworks that provide easy-to-follow procedures to derive the outage probability. Two general frameworks are proposed in this chapter, namely i) a moment generating function-based framework which is based on the numerical inversion of the Laplace transform of a cumulative distribution and (ii) a reference link power gain-based framework which exploits the distribution of the fading power gain between the reference transmitter and receiver. Note that the distribution of the distance between the reference point and an i.u.d. node in an arbitrarily shaped region is the key challenge in evaluating the outage performance, which has not been derived in the literature yet. Hence, we develop the general algorithm to exactly compute the distance distribution in closed-form that works for any convex shape and any location of reference node. Using the proposed frameworks and derived distance distribution function, we can calculate the exact outage probability at any location accounting for the boundary effects, whereby highlighting the location-dependent performance for the smart devices in ad-hoc networks.

This chapter is organized as follows. The system model and assumptions are presented in Section 2.1. The proposed general frameworks are described in detail in Section 2.2. For the case of the node locations modeled by a Binomial point process and i.i.d. Nakagami-m fading channels, the evaluation of the proposed frameworks for arbitrarily shaped finite wireless networks is detailed in Section 2.3. The outage probability analysis for the case of a reference receiver located anywhere in a disk and a convex polygon is presented in Section 2.4 and Section 2.5, respectively. The derived results are used to study the outage probability in Section 2.6. Finally, the chapter is summarized in Section 2.7.

2.1 Problem Formulation and System Model Assumptions

Consider a wireless network with $M+2$ nodes which are located inside an arbitrarily shaped finite region $\mathcal{A} \subset \mathbb{R}^2$, where $\mathbb{R}^2$ denotes the two-dimensional Euclidean domain. The $M+2$ nodes consist of a reference transmitter X_0, a reference receiver Y_0 and M interfering nodes. The M interfering nodes are distributed at random within the region $\mathcal{A}$. Throughout the chapter, we refer to X_i $(i = 1, 2, \ldots M)$ as both the random location as well as the ith interfering node itself. The reference receiver Y_0 is not restricted to be located at the center of the finite region but can be located *anywhere* inside the region $\mathcal{A}$. The reference transmitter X_0 is assumed to be placed at a given distance r_0 from Y_0. Let R_i $(i = 1, 2, \ldots M)$ denote the Euclidean distance between the ith interferer X_i and the reference receiver Y_0.

We focus on the performance of the reference link comprising the reference transmitter X_0 and the reference receiver Y_0, in the presence of M interfering nodes and noise. We consider a path-loss plus block-fading channel model. Let G_0 represent the instantaneous power gain due to fading only for the reference link and G_i represent the instantaneous power gain due to fading only between X_i and Y_0. The path-loss function can be expressed as

$$l(r) = r^{-\alpha}, \tag{2.1}$$

where r denotes the distance and α is the path-loss exponent, which typically lies in the range $2 \leq \alpha \leq 6$ [115]. Note that the path-loss model in (2.1) is unbounded and has a singularity as $r \to 0$. The singularity can be avoided by using a bounded path-loss model [116]. Because we consider the network from an outage perspective, the effect of the singularity in the bounded path-loss model is in fact negligible [117], as long as the SINR threshold (defined in (2.4)) is not too small. Thus, for simplicity, we can adopt the unbounded path-loss model for the purpose of outage probability computation.

Let P_0 and P_i denote the transmit powers for X_0 and X_i, respectively. The aggregate interference power at the reference receiver Y_0 is then given as

$$I = \sum_{i=1}^{M} P_i G_i R_i^{-\alpha}. \tag{2.2}$$

The instantaneous SINR at the reference receiver Y_0 is given by

$$\text{SINR} = \frac{P_0 G_0 r_0^{-\alpha}}{I + \mathcal{N}} = \frac{G_0}{\frac{I}{P_0 r_0^{-\alpha}} + \frac{1}{\gamma_0}}, \tag{2.3}$$

where $\gamma_0 = (P_0 r_0^{-\alpha})/\mathcal{N}$ is defined as the average signal-to-noise ratio (SNR) and $\mathcal{N}$ is the AWGN power.

We characterize the performance of the reference link in the presence of the aggregate interference and AWGN by using the outage probability. An outage is said to occur when the SINR falls below a given SINR threshold γ_{th}, i.e.,

$$P_{\text{out}} = \Pr(\text{SINR} < \gamma_{\text{th}}). \tag{2.4}$$

We are interested in obtaining the average outage probability in the arbitrarily shaped finite wireless network after un-conditioning with respect to the spatial node distribution and the fading distribution. This is addressed in the next section.

2.2 Proposed Frameworks

In this section, we propose two analytical frameworks to compute the outage probability in arbitrarily shaped finite wireless network. The first framework, named the moment generating function-based framework, is inspired from [108, 109]. The basic principle of this framework is the accurate numerical inversion of the Laplace transform of the cumulative distribution function for an appropriately defined random variable [108]. The second framework, named the reference link power gain-based framework, is based on the combination and generalization of the frameworks proposed in [57, 75]. The basic principle of this second framework is to find the cumulative distribution function of the reference link's fading power gain, which can then be used to find the outage probability. These frameworks are discussed in detail in the following subsections.

2.2.1 Moment Generating Function-based Framework

In this framework, it is necessary to define a suitable random variable. Substituting (2.3) into (2.4) and rearranging, we have

$$P_{\text{out}} = \Pr\left(\frac{I}{P_0 r_0^{-\alpha} G_0} + \frac{1}{\gamma_0 G_0} > \gamma_{\text{th}}^{-1}\right). \tag{2.5}$$

We define a random variable Z as

$$Z = \frac{I}{P_0 r_0^{-\alpha} G_0} + \frac{1}{\gamma_0 G_0}. \tag{2.6}$$

Hence, (2.5) can be re-written as

$$P_{\text{out}} = \Pr(Z > \gamma_{\text{th}}^{-1}) = 1 - F_Z(\gamma_{\text{th}}^{-1}). \tag{2.7}$$

In general, it is not possible to obtain a closed-form solution for $F_Z(\gamma_{\text{th}}^{-1})$. Hence, we use numerical inversion of Laplace transform to find $F_Z(\gamma_{\text{th}}^{-1})$. The CDF of a random variable Z is related to the Laplace transform of $F_Z(z)$ as

$$F_Z(z) = \frac{1}{2\pi\mathbf{i}} \int_{a-\mathbf{i}\infty}^{a+\mathbf{i}\infty} \mathcal{L}_{F_Z(z)}(s) \exp(sz) \mathrm{d}s, \tag{2.8}$$

where $\mathbf{i}$ is imaginary number $\sqrt{-1}$. Using the trapezoid rule, the above integral can be discretized to get a series and then we can truncate the infinite series to get a finite sum via the Euler summation [118]. Finally, since $\mathcal{L}_{F_Z(z)}(s) = \mathcal{L}_Z(s)/s$, (2.7) can be approximated by

$$P_{\text{out}} = 1 - \frac{2^{-B}\exp(\frac{A}{2})}{\gamma_{\text{th}}^{-1}} \sum_{b=0}^{B} \binom{B}{b} \sum_{c=0}^{C+b} \frac{(-1)^c}{D_c} \text{Re}\left\{\frac{\mathcal{L}_Z(s)}{s}\right\}, \tag{2.9}$$

where $D_c = 2$ (if $c = 0$) and $D_c = 1$ (if $c = 1, 2, \ldots$), $s = (A + \mathbf{i}2\pi c)/(2\gamma_{\text{th}}^{-1})$ and $\text{Re}\{\cdot\}$ denotes the real part. The three parameters A, B and C control the estimation error. The selection of the values for A, B and C for accurate numerical inversion will be discussed later in Section 2.6.1.

Using the definition of the Laplace transform of the probability distribution of a random variable, we can express $\mathcal{L}_Z(s)$ as

$$\begin{aligned}\mathcal{L}_Z(s) &= \mathbb{E}_{G_0,I}\left\{\exp\left(-s\left(\frac{I}{P_0 r_0^{-\alpha} G_0} + \frac{1}{\gamma_0 G_0}\right)\right)\right\} \\ &= \mathbb{E}_{G_0,G_i,R_i}\left\{\exp\left(-\frac{s}{\gamma_0 G_0}\right) \prod_{i=1}^{M} \exp\left(\frac{-sP_i G_i R_i^{-\alpha}}{P_0 r_0^{-\alpha} G_0}\right)\right\},\end{aligned} \tag{2.10}$$

where $\mathbb{E}_I\{\cdot\}$ denotes the expectation with respect to the aggregate interference and $\mathbb{E}_{G_i,R_i}\{\cdot\}$ represents the expectation with respect to G_i and R_i. Combining (2.9) and (2.10), we have the general outage probability expression resulting from the MGF-based framework as

$$P_{\text{out}} = 1 - \frac{2^{-B}\exp(\frac{A}{2})}{\gamma_{\text{th}}^{-1}} \sum_{b=0}^{B} \binom{B}{b} \sum_{c=0}^{C+b} \frac{(-1)^c}{D_c} \text{Re}\left\{\frac{\mathbb{E}_{G_i,R_i}\left\{\exp\left(\frac{-s}{\gamma_0 G_0}\right) \prod_{i=1}^{M} \exp\left(\frac{-sP_i G_i R_i^{-\alpha}}{P_0 r_0^{-\alpha} G_0}\right)\right\}}{s}\right\}. \tag{2.11}$$

2.2.2 Reference Link Power Gain-based Framework

As highlighted earlier, this framework relies on the cumulative distribution function $F_{G_0}(g_0)$ for the reference link's fading power gain G_0. We adopt the following general model[1] for the CDF [31]

$$F_{G_0}(g_0) = 1 - \sum_{n\in N} \exp(-ng_0) \sum_{k\in K} a_{nk} g_0^k, \tag{2.12}$$

where the finite sets $N, K \subset \mathbb{N}$ (where $\mathbb{N}$ is the set of natural number) and a_{nk} are the coefficients. With the proper choice of a_{nk}, N and K, $F_{G_0}(g_0)$ can represent different types of distributions for the fading power gain [31]. For example, when $N = \{1\}$, $K = \{0\}$ and $a_{nk} = 1$, then $F_{G_0}(g_0) = 1 - \exp(-g_0)$ and consequently $f_{G_0}(g_0)$ reduces to the Exponential distribution, which corresponds to the reference link undergoing Rayleigh fading [122]. Furthermore, if $N = \{m_0\}$, $K = \{0, ..., m_0 - 1\}$ and $a_{nk} = \frac{m_0^k}{k!}$, then $F_{G_0}(g_0) = 1 - \exp(-m_0 g_0) \sum_{k=0}^{m_0-1} m_0^k g_0^k / k!$ and consequently $f_{G_0}(g_0)$ reduces to the Gamma distribution [123] which corresponds to the reference link experiencing Nakagami-m fading.

We proceed by re-writing the outage probability in (2.4) as

$$P_{\text{out}} = \mathbb{E}_I \left\{ \Pr\left(\frac{G_0}{\frac{I}{P_0 r_0^{-\alpha}} + \frac{1}{\gamma_0}} < \gamma_{\text{th}} \middle| I \right) \right\} = \mathbb{E}_I \left\{ \Pr\left(G_0 < \gamma_{\text{th}} \left(\frac{I}{P_0 r_0^{-\alpha}} + \frac{1}{\gamma_0} \right) \middle| I \right) \right\}, \tag{2.13}$$

where $\Pr(\cdot|\cdot)$ is the conditional probability measure.

Using $F_{G_0}(g_0)$ shown in (2.12), (2.13) can be written as

$$\begin{aligned} P_{\text{out}} =& \mathbb{E}_I \left\{ F_{G_0} \left(\frac{\gamma_{\text{th}}}{P_0 r_0^{-\alpha}} I + \frac{\gamma_{\text{th}}}{\gamma_0} \right) \right\} \\ =& 1 - \sum_{n\in N} \exp\left(-n \frac{\gamma_{\text{th}}}{\gamma_0} \right) \sum_{k\in K} a_{nk} \mathbb{E}_I \left\{ \exp\left(-n \frac{\gamma_{\text{th}}}{P_0 r_0^{-\alpha}} I \right) \left(\frac{\gamma_{\text{th}}}{P_0 r_0^{-\alpha}} I + \frac{\gamma_{\text{th}}}{\gamma_0} \right)^k \right\}, \end{aligned} \tag{2.14}$$

where the aggregate interference I depends on the fading power gain distribution and the distance distribution. Hence, (2.14) can be further expanded in terms of G_i and R_i. First, we focus on the expansion of the term $\exp\left(-n \frac{\gamma_{\text{th}}}{P_0 r_0^{-\alpha}} I \right) \left(\frac{\gamma_{\text{th}}}{P_0 r_0^{-\alpha}} I + \frac{\gamma_{\text{th}}}{\gamma_0} \right)^k$. Based on the binomial

[1] We note that it may be possible to consider other general classes of fading channels [119, 120, 121], but this is outside the scope of this chapter.

theorem [124] and using (2.2), we have

$$\exp\left(-n\frac{\gamma_{\text{th}}}{P_0 r_0^{-\alpha}} I\right)\left(\frac{\gamma_{\text{th}}}{P_0 r_0^{-\alpha}} I+\frac{\gamma_{\text{th}}}{\gamma_0}\right)^k$$
$$=\exp\left(-n\frac{\gamma_{\text{th}}}{P_0 r_0^{-\alpha}}\sum_{i=1}^{M} P_i G_i R_i^{-\alpha}\right)\sum_{j=0}^{k}\binom{k}{j}\left(\frac{\gamma_{\text{th}}}{\gamma_0}\right)^{k-j}\left(\frac{\gamma_{\text{th}}}{P_0 r_0^{-\alpha}}\right)^{j}\left(\sum_{i=1}^{M} P_i G_i R_i^{-\alpha}\right)^{j}. \quad (2.15)$$

Following the multinomial theorem [125], we then can expand the term $\left(\sum_{i=1}^{M} P_i G_i R_i^{-\alpha}\right)^j$ into

$$\left(\sum_{i=1}^{M} P_i G_i R_i^{-\alpha}\right)^{j}=\sum_{t_1+t_2+\ldots+t_M=j}\binom{j}{t_1,t_2,\ldots,t_M}\prod_{i=1}^{M}\left(P_i G_i R_i^{-\alpha}\right)^{t_i}, \quad (2.16)$$

where t_i $(i=1,2,\ldots M)$ is a non-negative integer and the multinomial coefficient $\binom{j}{t_1,t_2,\ldots,t_M}=\frac{j!}{t_1!t_2!\ldots t_M!}$.

Combining (2.15) and (2.16) and substituting back into (2.14), we have the general outage probability expression resulting from the RLPG-based framework as

$$P_{\text{out}}=1-\sum_{n\in N}\exp\left(-n\frac{\gamma_{\text{th}}}{\gamma_0}\right)\sum_{k\in K} a_{nk}\sum_{j=0}^{k}\binom{k}{j}\left(\frac{\gamma_{\text{th}}}{\gamma_0}\right)^{k-j}\left(\frac{\gamma_{\text{th}}}{P_0 r_0^{-\alpha}}\right)^{j}$$
$$\times\sum_{t_1+t_2\ldots+t_M=j}\binom{j}{t_1,t_2,\ldots,t_M}\mathbb{E}_{G_i,R_i}\left\{\exp\left(-n\frac{\gamma_{\text{th}}}{P_0 r_0^{-\alpha}}\sum_{i=1}^{M} P_i G_i R_i^{-\alpha}\right)\prod_{i=1}^{M}\left(P_i G_i R_i^{-\alpha}\right)^{t_i}\right\}. \quad (2.17)$$

Remark 1. *The two general formulations in* (2.11) *and* (2.17) *are valid for any spatial node distribution with a fixed number of nodes in an arbitrarily shaped finite wireless network and any location of the reference receiver inside the arbitrarily shaped finite region. The MGF-based framework in* (2.11) *is valid for any fading channel distribution. The RLPG-based framework in* (2.17) *is valid for a general class of fading channel distribution defined in* (2.12)*. In general, the two formulations cannot be expressed in closed-form. The evaluation of the outage probability in* (2.11) *and* (2.17) *requires the knowledge of the joint probability density function of the distance R_i and the fading power gain G_i. For an arbitrary location of a reference point inside an arbitrarily shaped convex region, the joint probability density function can be a complex piece-wise function, which does not allow the outage probability to be computed in a closed-form. However, it must be noted that* (2.11) *and* (2.17) *give analytical expressions of the outage probability for arbitrarily shaped finite wireless networks in a general setting, which has not been demonstrated in the literature to date.*

In the next section, in order to demonstrate the evaluation and use of the proposed frame-

works, we consider the case of that the nodes are distributed at random inside an arbitrarily shaped finite wireless network according to a BPP and all fading channels are i.i.d. Nakagami-m fading channels.

2.3 Outage Probability for BPP and Nakagami-m Fading Channels

In this section, we consider the scenarios where:

A1. The M interfering nodes are independently and identically distributed at random inside an arbitrarily shaped finite wireless network, i.e. the nodes are distributed at random according to a general BPP [71, Definition 2.12] (general location assumption).

A2. The fading channels are i.i.d..

A3. The transmit powers P_0 and P_i are normalized to unity.

A4. The fading channels follow a Nakagami-m distribution. Nakagami-m distribution is widely used in the literature to model the distribution of the signal envelopes in various fading environments, such as the land-mobile and indoor-mobile multipath propagation environments [115]. The parameter m, which lies in the range $1/2$ to ∞, describes the severity of the fading channel. Note that it is not necessary for m to be an integer number only. When $m \leq 1$, Nakagami-m distribution provides a close approximation to Nakagami-q (Hoyt) distribution with parameter mapping $m = ((1+q^2)^2)/(2(1+2q^4))$. Additionally, when $m > 1$, Nakagami-m distribution closely approximates Nakagami-n (Rice) distribution with parameter mapping $m = ((1+n^2)^2)/(1+2n^2)$ [115]. It is well known that $m = \infty$ corresponds to the no-fading case, $m = 1$ represents the special case of Rayleigh fading and $m = 1/2$ represents that unilateral Gauss distribution [115], which corresponds to the most severe Nakagami-m fading.

A5. The nodes are distributed at random according to a *uniform* BPP [71, Definition 2.11]. This means that the nodes are independently and uniformly distributed inside the arbitrarily shaped finite wireless network (specific location assumption).

As a consequence of assumptions A1 and A2, the joint PDF of the distance R_i and the fading power gain G_i can be decomposed into the individual PDFs, which are denoted as $f_{R_i}(r_i)$ and $f_{G_i}(g_i)$, respectively. Due to assumption A1, the distribution of R_i is the same for all i. Similarly, due to assumption A2, the distribution of G_i is the same for all i as well. Thus, we can drop the index i in R_i, G_i, $f_{R_i}(r_i)$ and $f_{G_i}(g_i)$ and let $f_{R_i}(r_i) = f_R(r)$ and $f_{G_i}(g_i) = f_G(g)$.

Let $f_{G_0}(g_0)$ denotes the PDF of fading power gain for the reference link. From assumption A4, since the fading coefficients for both the reference link and the interference links are modeled using a Nakagami-m distribution, i.e., $f_{G_0}(g_0) = f_G(g)$, the distribution for the fading power gains G_0 and G can be modeled as a Gamma distribution with the following PDF [123]

$$f_G(g) = \frac{g^{m-1}m^m}{\Gamma[m]} \exp(-mg), \tag{2.18}$$

where $\Gamma[\cdot]$ is the complete Gamma function. Note that we will represent Nakagami-m fading parameter for the reference and interfering links as m_0 and m, respectively. Even though the fading power gain distributions are identical, we will still use m_0 and m to distinguish the reference link from the interference link for the sake of analytical convenience.

2.3.1 MGF-based Framework

Using assumptions A1$-$A3, i.e., i.i.d. random nodes and i.i.d. fading channels, the general outage probability expression in (2.11) for the MGF-based framework can be simplified to

$$\begin{aligned} P_{\text{out}} =& 1 - \frac{2^{-B}\exp(\frac{A}{2})}{\gamma_{\text{th}}^{-1}} \sum_{b=0}^{B} \binom{B}{b} \\ & \times \sum_{c=0}^{C+b} \frac{(-1)^c}{D_c} \text{Re}\left\{ \frac{\mathbb{E}_{G_0}\left\{ \exp\left(-\frac{s}{\gamma_0 G_0}\right) \left(\mathbb{E}_{G,R}\left\{\exp\left(\frac{-sGR^{-\alpha}}{r_0^{-\alpha}G_0}\right)\right\}\right)^M \right\}}{s} \right\}. \end{aligned} \tag{2.19}$$

Using assumption A4 and substituting (2.18) in (2.19), the outage probability in (2.19) can be expressed as

$$\begin{aligned} P_{\text{out}} =& 1 - \frac{2^{-B}\exp(\frac{A}{2})}{\gamma_{\text{th}}^{-1}} \sum_{b=0}^{B} \binom{B}{b} \sum_{c=0}^{C+b} \frac{(-1)^c}{D_c} \\ & \times \text{Re}\left\{ \frac{\int_0^\infty \exp\left(-\frac{s}{\gamma_0 g_0}\right) \left(\mathbb{E}_{G,R}\left\{\exp\left(\frac{-sGR^{-\alpha}}{r_0^{-\alpha}G_0}\right)\right\}\right)^M \frac{g_0^{m_0-1}m_0^{m_0}}{\Gamma[m_0]} \exp(-m_0 g_0) \text{d}g_0}{s} \right\}, \end{aligned} \tag{2.20}$$

where the expectation in (2.20) can be expressed as

$$\mathbb{E}_{G,R}\left\{\exp\left(\frac{-sGR^{-\alpha}}{r_0^{-\alpha}G_0}\right)\right\} = \int_0^{r_{\max}} m^m \left(m + \frac{r^{-\alpha}r_0^{\alpha}s}{g_0}\right)^{-m} f_R(r)\,\text{d}r, \tag{2.21}$$

where $r_{\max}$ denotes the maximum range of the random variable R, which depends on the ar-

bitrarily shaped finite region $\mathcal{A}$ and the location of the reference node. Note that m_0 and m in (2.20) can take any values (whether integer or non-integer).

2.3.2 RLPG-based Framework

Using assumptions A1−A3, i.e., i.i.d. random nodes and i.i.d. fading channels, the general outage probability expression in (2.17) for the RLPG-based framework can be simplified to

$$P_{\text{out}} = 1 - \sum_{n\in N} \exp\left(-n\frac{\gamma_{\text{th}}}{\gamma_0}\right) \sum_{k\in K} a_{nk} \sum_{j=0}^{k} \binom{k}{j} \left(\frac{\gamma_{\text{th}}}{\gamma_0}\right)^{k-j} (\gamma_{\text{th}} r_0^{\alpha})^{j} \times \sum_{t_1+t_2\ldots+t_M=j} \binom{j}{t_1, t_2, \ldots, t_M} \prod_{i=1}^{M} \mathbb{E}_{G,R}\left\{\Omega_{t_i}\right\}, \tag{2.22}$$

where $\Omega_{t_i} = \exp\left(-n\gamma_{\text{th}} r_0^{\alpha} G R^{-\alpha}\right) \left(G R^{-\alpha}\right)^{t_i}$ is defined for analytical convenience.

Using assumption A4, the outage probability in (2.22) can be expressed for the case of Nakagami-m fading with integer m_0 as

$$P_{\text{out}} = 1 - \exp\left(-m_0\frac{\gamma_{\text{th}}}{\gamma_0}\right) \sum_{k=0}^{m_0-1} \frac{m_0^k}{k!} \sum_{j=0}^{k} \binom{k}{j} \left(\frac{\gamma_{\text{th}}}{\gamma_0}\right)^{k-j} (\gamma_{\text{th}} r_0^{\alpha})^{j} \times \sum_{t_1+t_2\ldots+t_M=j} \binom{j}{t_1, t_2, \ldots, t_M} \prod_{i=1}^{M} \mathbb{E}_{G,R}\left\{\Omega_{t_i}\right\}, \tag{2.23}$$

where the expectation in (2.23) can be expressed using (2.18) as

$$\mathbb{E}_{G,R}\left\{\Omega_{t_i}\right\} = \int_0^{r_{\max}} \frac{m^m (r^{-\alpha})^{t_i} \Gamma[m+t_i]}{\Gamma[m]\left(m + \gamma_{\text{th}} r_0^{\alpha} m_0 r^{-\alpha}\right)^{m+t_i}} f_R(r)\, \mathrm{d}r, \tag{2.24}$$

where $r_{\max}$ is defined below (2.21).

Remark 2. *For the RLPG-based framework, m_0 is constrained to take integer values only, while m can take any value. The restriction on m_0 is because $m_0 - 1$, as an upper limit for the summation in* (2.23)*, can only be integer. This is in contrast with* (2.20) *where both m_0 and m can take any (integer or non-integer) value for the MGF-based framework.*

Summarizing, (2.11) and (2.17) take the form of (2.20) and (2.23), respectively, for M interfering nodes i.i.d. at random inside an arbitrarily shaped finite wireless network with i.i.d. Nakagami-m fading channels.

2.3.3 Need for the Two Frameworks

The proposed two frameworks complement each other. On one hand, as highlighted in Remark 2, the MGF-based framework can be used in scenarios with non-integer m_0 while the RLPG-based framework can only be used in scenarios with integer m_0. On the other hand, the RLPG-based framework is more capable of yielding closed-form analytical expressions than the MGF-based framework. For the MGF-based framework, the outage probability in (2.20) involves a double integration (an integration with an expectation term in the integrand). In general, it is not possible to obtain a closed-form for the integration part in (2.20) because the expectation term is raised to a power factor of M ($M \geq 2$). However, in certain cases, the expectation term can be expressed in closed-form. For the RLPG-based framework, the outage probability in (2.23) involves a single integration which admits closed-form results in a much larger number of cases.

Note that both (2.20) and (2.23) require the knowledge of the distance distribution $f_R(r)$, i.e. the PDF of the distance of a random node from the reference receiver Y_0, for their evaluation. The distance distribution $f_R(r)$ is dependent on the underlying random model for the node locations. For the uniform BPP (assumption A5), which is considered in this work, the distance distribution $f_R(r)$ is derived in [58] for the special case when the reference receiver is located at the center of a convex regular polygon. Recently, the result in [58] was generalized in [65] for the case when the reference receiver is located anywhere inside a convex regular polygon. It was shown in [65] that for an arbitrary location of the reference receiver inside convex regular polygon, the distance distribution $f_R(r)$ can be a complicated piece-wise function because of the boundary effects. We note that the approach in [65] is also applicable for arbitrarily shaped convex polygons (see Appendix A.1 for details). Once $f_R(r)$ is given, both (2.20) and (2.23) and can be accurately evaluated.

In the next two sections, we show how (2.20) and (2.23) can be evaluated in disk and polygon regions, which are commonly used in the literature for the modeling of wireless networks. We also illustrate how the proposed frameworks can be applied in the case of arbitrarily shaped finite wireless networks with arbitrary location of the reference receiver.

2.4 Outage Probability in a Disk Region

Consider the scenario that the region $\mathcal{A}$ is a disk of radius $\mathcal{R}$, as shown in Figure 2.1. The reference receiver is assumed to be located at a distance d from the center of the disk. Then,

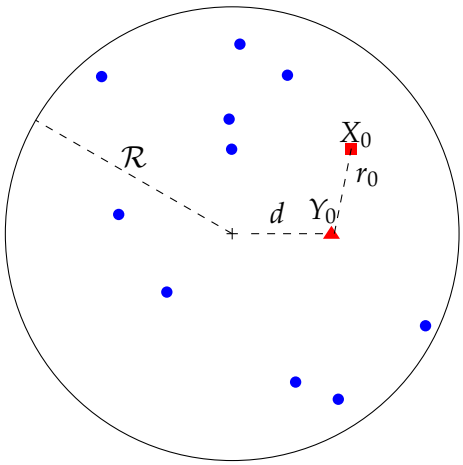

Figure 2.1: Illustration of a finite wireless network with arbitrary location of reference receiver Y_0 in a disk region of radius $\mathcal{R}$ ($+$ = center of disk, $\bullet$ = interfering node, $\blacktriangle$ = reference receiver, $\blacksquare$ = reference transmitter).

the distance distribution $f_R(r)$ can be exactly expressed as [65]

$$f_R(r) = \frac{1}{|\mathcal{A}|} \begin{cases} 2\pi r, & 0 \le r \le \mathcal{R} - d; \\ 2r \arccos\left(\frac{r^2+d^2-\mathcal{R}^2}{2rd}\right), & \mathcal{R} - d \le r \le \mathcal{R} + d. \end{cases} \tag{2.25}$$

Note that substituting $d = 0$ in (2.25) gives the distance distribution for the special case that Y_0 is located at the center of the disk. Similarly, substituting $d = \mathcal{R}$ in (2.25) gives the distance distribution for the special case that Y_0 is located anywhere on the circumference of the disk.

2.4.1 MGF-based Framework

Substituting (2.25) in (2.21), we find that the expectation has a closed-form only for the first part of the range $(0 \le r \le \mathcal{R} - d)$ in (2.25). For the second-part of the range $(\mathcal{R} - d \le r \le \mathcal{R} + d)$, the integration does not have a closed-form due to the $\arccos(\cdot)$ function. The result is shown in (2.26).

$$\mathbb{E}_{G,R}\left\{\exp\left(\frac{-sGR^{-\alpha}}{r_0^{-\alpha}G_0}\right)\right\} = \Psi_1\left(2\pi, \mathcal{R} - d\right) + \frac{2m^m}{|\mathcal{A}|}\int_{\mathcal{R}-d}^{\mathcal{R}+d}\left(m + \frac{r^{-\alpha}r_0^{\alpha}s}{g_0}\right)^{-m} r \arccos\left(\frac{r^2+d^2-\mathcal{R}^2}{2rd}\right) \mathrm{d}r, \tag{2.26}$$

where

$$\Psi_1\left(\omega, v\right) = \frac{\omega m^m g_0^m v^{2+\alpha m}}{|\mathcal{A}|(2+\alpha m)\left(r_0^{\alpha}s\right)^m} {}_2F_1\left[m, \frac{2}{\alpha} + m; 1 + \frac{2}{\alpha} + m; -\frac{g_0 m v^{\alpha}}{r_0^{\alpha}s}\right], \tag{2.27}$$

and ${}_2F_1\left[\cdot,\cdot;\cdot;\cdot\right]$ is the ordinary hypergeometric function.

Substituting (2.26) in (2.20), the outage probability can be numerically evaluated.

2.4.2 RLPG-based Framework

Substituting (2.25) in (2.24) and after some manipulations, we get

$$\mathbb{E}_{G,R}\left\{\Omega_{t_i}\right\} = \Psi_2\left(2\pi, \mathcal{R}-d, t_i\right) + \frac{2m^m\Gamma[m+t_i]}{|\mathcal{A}|\Gamma[m]}\int_{\mathcal{R}-d}^{\mathcal{R}+d}\frac{(r^{-\alpha})^{t_i}r}{\left(m+\gamma_{\text{th}}r_0^{\alpha}m_0r^{-\alpha}\right)^{m+t_i}}\arccos\left(\frac{r^2+d^2-\mathcal{R}^2}{2rd}\right)\mathrm{d}r, \tag{2.28}$$

where

$$\Psi_2\left(\omega,\upsilon,\tau\right) = \frac{\omega m^m\upsilon^{2+\alpha m}\Gamma[m+\tau]}{|\mathcal{A}|\left(\gamma_{\text{th}}r_0^{\alpha}m_0\right)^{m+\tau}(2+\alpha m)\Gamma[m]}\,{}_2F_1\left[\frac{2}{\alpha}+m, m+\tau; 1+\frac{2}{\alpha}+m; \frac{-m\upsilon^{\alpha}}{\gamma_{\text{th}}r_0^{\alpha}m_0}\right]. \tag{2.29}$$

In general, the integration in (2.28) also does not have a closed-form due to the $\arccos(\cdot)$ function. It is possible to use the Gauss-Chebyshev integration technique [126] to further express the integration in an approximate closed-form expression. However, in our investigations, we found that a summation over a large number of terms (> 1000) was required in our case for accurate evaluation. Hence, we do not pursue approximations and instead directly substitute (2.28) in (2.23) to obtain the outage probability.

Special case: For the case of the reference receiver Y_0 located at the center of the disk, $d = 0$. Substituting this value in (2.28) and then substituting the result in (2.23), the final expression for the outage probability simplifies to

$$P_{\text{out}}^{\text{center}} = 1 - \exp\left(-m_0\frac{\gamma_{\text{th}}}{\gamma_0}\right)\sum_{k=0}^{m_0-1}\frac{m_0^k}{k!}\sum_{j=0}^{k}\binom{k}{j}\left(\frac{\gamma_{\text{th}}}{\gamma_0}\right)^{k-j}\left(\gamma_{\text{th}}r_0^{\alpha}\right)^j \times \sum_{t_1+t_2\ldots+t_M=j}\binom{j}{t_1,t_2,\ldots,t_M}\prod_{i=1}^{M}\Psi_2\left(2\pi,\mathcal{R},t_i\right), \tag{2.30}$$

where $\Psi_2(\cdot,\cdot,\cdot)$ is defined in (2.29).

Remark 3. *The outage probability for a finite number of nodes i.u.d. in a disk region has been widely considered in the recent literature. Our proposed frameworks reproduce the available outage results in the literature as special cases. For the MGF-based framework, with* $m_0 = 1$*, the result from* (2.26) *is equivalent to the result in [57, eq.(24)]. For the RLPG-based framework, with the reference receiver located at the center of the network,* (2.30) *is identical*

to the result in [75, eq.(44)].

2.5 Outage Probability in Regular Polygons and Arbitrarily Shaped Convex Polygons

In this section, we illustrate the exact computation of the outage probability in both regular and arbitrarily shaped convex polygon regions. We will consider the following two cases (i) reference receiver Y_0 located at the center of a regular L-sided polygon and (ii) reference receiver Y_0 located at an arbitrary location in an arbitrarily shaped region.

2.5.1 Center of Polygon

Consider the finite region $\mathcal{A}$ to be a regular L-sided convex polygon which is inscribed in a circle of radius $\mathcal{R}$. Then, the area and the interior angle between two adjacent sides are given by

$$|\mathcal{A}| = \frac{1}{2} L \mathcal{R}^2 \sin\left(\frac{2\pi}{L}\right), \tag{2.31a}$$

$$\theta = \frac{\pi(L-2)}{L}. \tag{2.31b}$$

In general, polygon regions are non-isotropic. Hence, there is no single expression for the distance distribution $f_R(r)$ for an arbitrary location of the reference receiver inside a convex regular polygon. For the special case that the reference receiver Y_0 is located at the center of an L-sided convex regular polygon, the distance distribution $f_R(r)$ can be expressed as [58, 65]

$$f_R(r) = \frac{1}{|\mathcal{A}|} \begin{cases} 2\pi r, & 0 \le r \le \mathcal{R}_p; \\ 2\pi r - 2Lr \arccos\left(\frac{\mathcal{R}_p}{r}\right), & \mathcal{R}_p \le r \le \mathcal{R}; \end{cases} \tag{2.32}$$

where $\mathcal{R}_p = \mathcal{R}\sin\left(\frac{\theta}{2}\right)$. Using (2.32), we illustrate the computation of the outage probability using the two frameworks.

MGF-based Framework: Substituting (2.32) in (2.21) and after some manipulations, we get

$$\mathbb{E}_{G,R}\left\{\exp\left(\frac{-sGR^{-\alpha}}{r_0^{-\alpha}G_0}\right)\right\} = \Psi_1(2\pi, \mathcal{R}) - \frac{2Lm^m}{|\mathcal{A}|}\int_{\mathcal{R}_p}^{\mathcal{R}} \left(m + \frac{r^{-\alpha}r_0^{\alpha}s}{g_0}\right)^{-m} r \arccos\left(\frac{\mathcal{R}_p}{r}\right) \mathrm{d}r, \tag{2.33}$$

where $\Psi_1(\cdot,\cdot)$ is defined in (2.27). Substituting (2.33) in (2.20), the outage probability can be evaluated.

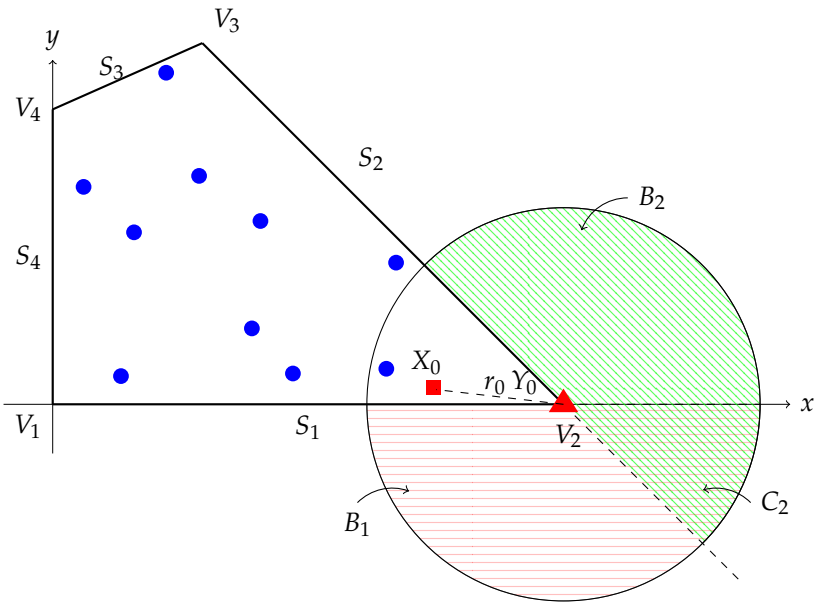

Figure 2.2: Illustration of an arbitrary location of a reference receiver in an arbitrarily shaped finite wireless network, with side lengths $S_1 = \sqrt{3}\mathcal{W}$, $S_2 = \sqrt{3}\mathcal{W}$, $S_3 = \sqrt{7-3\sqrt{3}-\sqrt{6}}\mathcal{W}$ and $S_4 = \mathcal{W}$ and vertices V_1, V_2, V_3 and V_4. The areas B_1 (shaded in horizontal lines), lines) and C_2 (intersection of horizontal and diagonal lines) are defined in Appendix A.1 (● = interfering node, ▲ = reference receiver, ■ = reference transmitter).

RLPG-based Framework: Substituting (2.32) in (2.24), and after some manipulations, we get

$$\mathbb{E}_{G,R}\left\{\Omega_{t_i}\right\} = \Psi_2\left(2\pi, \mathcal{R}, t_i\right) - \frac{2Lm^m\Gamma[m+t_i]}{|\mathcal{A}|\Gamma[m]}\int_{\mathcal{R}_p}^{\mathcal{R}} \frac{(r^{-\alpha})^{t_i} r}{\left(m+\gamma_{\text{th}} r_0^{\alpha} m_0 r^{-\alpha}\right)^{m+t_i}} \arccos\left(\frac{\mathcal{R}_p}{r}\right) \mathrm{d}r, \tag{2.34}$$

where $\Psi_2(\cdot,\cdot,\cdot)$ is defined in (2.29). Substituting (2.34) in (2.23), the outage probability can be evaluated.

2.5.2 Arbitrarily Shaped Convex Polygon Region

We consider an arbitrarily shaped convex polygon region as shown in Figure 2.2, with side lengths $S_1 = S_2 = \sqrt{3}\mathcal{W}$, $S_3 = \sqrt{7-3\sqrt{3}-\sqrt{6}}\mathcal{W}$ and $S_4 = \mathcal{W}$. Thus, the interior angles formed at vertices V_1, V_2, V_3 and V_4 are $\pi/2$, $\pi/4$, 0.6173π and 0.6327π. Suppose that Y_0 is located at the vertex V_2[2]. Then, following the derivation in Appendix A.1, $f_R(r)$ can be

[2]The Y_0 location at vertex V_2 is chosen here for the sake of simplicity. Later in Section 2.6, we also show results for an arbitrary location of Y_0 inside the arbitrarily shaped convex polygon region considered in Figure 2.2.

expressed as

$$f_R(r) = \frac{1}{|\mathcal{A}|} \begin{cases} \frac{\pi}{4} r, & 0 \le r \le \sqrt{3}\mathcal{W}; \\ 0.3673\pi r - r \arccos\left(\frac{\sqrt{3}\mathcal{W}}{r}\right) - r \arccos\left(\frac{1.6159\mathcal{W}}{r}\right), & \sqrt{3}\mathcal{W} \le r \le 2\mathcal{W}. \end{cases} \tag{2.35}$$

Using (2.35), we illustrate the computation of the outage probability using the two frameworks.
MGF-based Framework: Substituting (2.35) in (2.21), the expectation can be expressed as

$$\mathbb{E}_{G,R}\left\{\exp\left(\frac{-sGR^{-\alpha}}{r_0^{-\alpha}G_0}\right)\right\} = \Psi_1\left(0.3673\pi, 2\mathcal{W}\right) - \Psi_1\left(0.1173\pi, \sqrt{3}\mathcal{W}\right) - \frac{m^m}{|\mathcal{A}|}\int_{\sqrt{3}\mathcal{W}}^{2\mathcal{W}} \left(m + \frac{r^{-\alpha} r_0^{\alpha} s}{g_0}\right)^{-m} r \left(\arccos\left(\frac{\sqrt{3}\mathcal{W}}{r}\right) + \arccos\left(\frac{1.6159\mathcal{W}}{r}\right)\right) \mathrm{d}r, \tag{2.36}$$

where $\Psi_1(\cdot,\cdot)$ is defined in (2.27). Finally, the outage probability for the case of the reference receiver located at vertex V_2 can be evaluated by substituting (2.36) in (2.20).
RLPG-based Framework: Substituting (2.35) in (2.24), the expectation can be expressed as

$$\mathbb{E}_{G,R}\left\{\Omega_{t_i}\right\} = \Psi_2\left(0.3673\pi, 2\mathcal{W}, t_i\right) - \Psi_2\left(0.1173\pi, \sqrt{3}\mathcal{W}, t_i\right) - \frac{m^m \Gamma[m+t_i]}{|\mathcal{A}|\Gamma[m]} \times \int_{\sqrt{3}\mathcal{W}}^{2\mathcal{W}} \frac{(r^{-\alpha})^{t_i} r}{\left(m + \gamma_{\mathrm{th}} r_0^{\alpha} m_0 r^{-\alpha}\right)^{m+t_i}} \left(\arccos\left(\frac{\sqrt{3}\mathcal{W}}{r}\right) + \arccos\left(\frac{1.6159\mathcal{W}}{r}\right)\right) \mathrm{d}r, \tag{2.37}$$

where $\Psi_2(\cdot,\cdot,\cdot)$ is defined in (2.29). Finally, the outage probability for the case of the reference receiver located at vertex V_2 can be evaluated by substituting (2.37) in (2.23).

Summarizing, the procedure for deriving the outage probability for i.u.d. nodes in an arbitrarily shaped convex polygon region with i.i.d. Nakagami-m fading channels is summarized in Algorithm 1.

Algorithm 1. *Proposed Algorithm*

Step 1: Choose the location of the reference receiver inside the arbitrarily shaped convex polygon region.

Step 2: Determine $f_R(r)$ based on the approach summarized in Appendix A.1.

Step 3: Depending on the value of m_0, select the appropriate framework to calculate the outage probability.

if *m_0 is non-integer* ***then***

Use the MGF-based framework. Substitute $f_R(r)$ in (2.21) *and then* (2.21) *in* (2.20) *to*

Table 2.1: Summary of the Main Outage Probability Results.

	Equation	Node distribution	Region	Reference receiver location	Fading channels
MGF-based Framework	(2.11)	any	any	any	any
	(2.19)	i.i.d.	any	any	i.i.d.
	(2.20)	i.i.d.	any	any	i.i.d. Nakagami-m
	(2.20) & (2.26)	i.u.d.	disk	any	i.i.d. Nakagami-m
	(2.20) & (2.33)	i.u.d.	polygon	center	i.i.d. Nakagami-m
RLPG-based Framework	(2.17)	any	any	any	Reference link: (2.12) [31] & Interference links: any
	(2.22)	i.i.d.	any	any	Reference link: (2.12) [31] & Interference links: i.i.d.
	(2.23)	i.i.d.	any	any	i.i.d. Nakagami-m with interger m_0 for reference link
	(2.23) & (2.28)	i.u.d.	disk	any	i.i.d. Nakagami-m with interger m_0 for reference link
	(2.23) & (2.34)	i.u.d.	polygon	center	i.i.d. Nakagami-m with interger m_0 for reference link

compute the outage probability.

else

Use the RLPG-based framework. Substitute $f_R(r)$ *in* (2.24) *and then* (2.24) *in* (2.23) *to compute the outage probability.*

end if

2.6 Numerical and Simulation Results

In this section, we first address the computational aspects of the two frameworks. We then study the outage probability performance of arbitrarily shaped finite wireless networks and discuss the boundary effects in finite wireless networks in detail. A summary of the main outage probability results in this chapter is summarized in Table 2.1.

2.6.1 Computational Aspects of the Frameworks

In general, both frameworks require numerical evaluation of integration, for which any standard mathematical package such as Matlab or Mathematica can be used. It must be noted that the numerical evaluation of single and double integrations is standard and widely practiced in the wireless communications literature [127].

For the MGF-based framework, the outage expressions in (2.11), (2.19) and (2.20) are

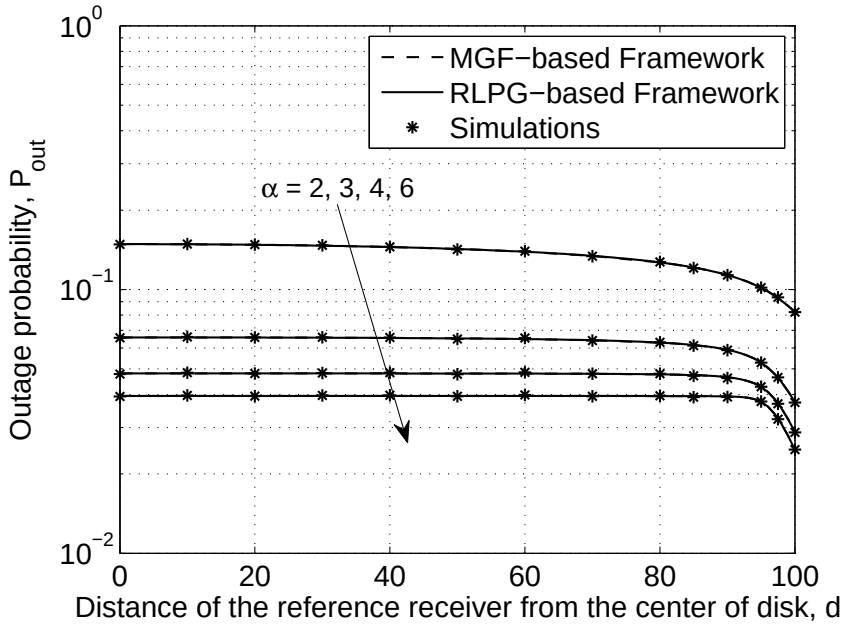

Figure 2.3: Outage probability, P_{out}, versus the distance of the reference receiver from the center of disk, d, for $M = 10$ interferers i.u.d. in a disk of radius $\mathcal{R} = 100$, with reference link distance $r_0 = 5$, path-loss exponents $\alpha = 2, 3, 4, 6$, i.i.d. Rayleigh fading channels ($m_0 = m = 1$), SINR threshold $\gamma_{\text{th}} = 0$ dB and SNR $\gamma_0 = 20$ dB.

a summation over a finite number of terms. The three parameters A, B and C (defined below (2.9)) control the estimation error. Following the well established guidelines in [108], [118], in order to achieve an estimation accuracy of $10^{-\zeta}$ (i.e., having the $(\zeta - 1)$th decimal correct), A, B and C have to at least equal $\zeta \ln 10$, $1.243\zeta - 1$, and 1.467ζ, respectively. For example, for the disk region, we set $A = 8 \ln 10$, $B = 11$, $C = 14$. This achieves stable numerical inversion with an estimation error of 10^{-8}.

For the RLPG-based framework, if both m_0 and M are large, then the computation of all possible integer results for t_i in $t_1 + t_2 + ... + t_M = j$ $(j = 0, ..., m_0 - 1)$ in (2.17), (2.22) and (2.23) can be time-consuming. This is due to the fact that we need to use M for loops to find the complete results. However, when either m_0 or M is a small number we can precompute these results, as suggested in [75], and store them as a matrix for use in computations.

2.6.2 Validation of the Proposed Two Frameworks

Figure 2.3 plots the outage probability, P_{out}, versus the distance of the reference receiver from the center of disk, d, for path-loss exponents $\alpha = 2, 3, 4, 6$ and i.i.d. Rayleigh fading channels. The solid lines are plotted using (2.23) and (2.28), i.e., the RLPG-based framework. The dash lines are plotted using (2.20) and (2.26), i.e., the MGF-based framework. For the simulation results, we uniformly distribute the users inside a disk region and average the results over 1

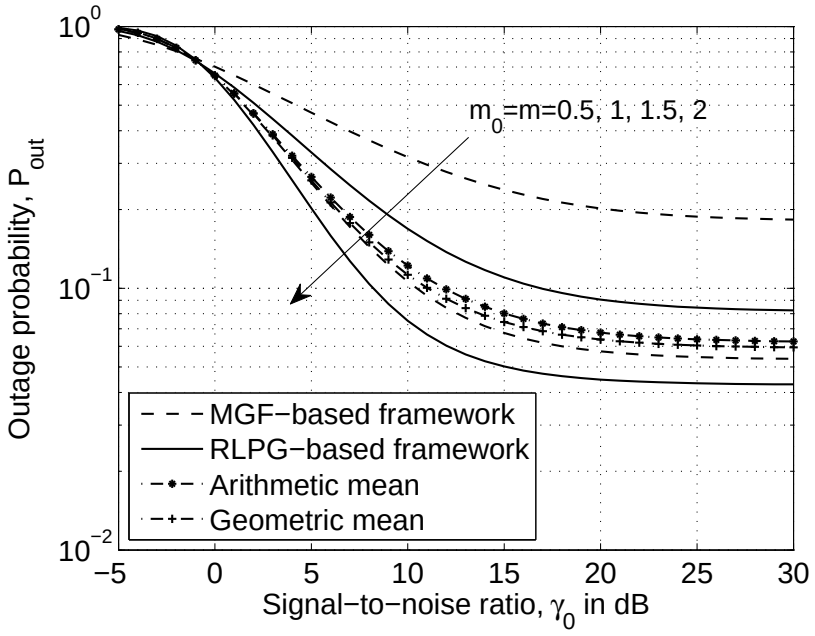

Figure 2.4: Outage probability, P_{out}, versus the signal-to-noise ratio, γ_0, for i.i.d. Nakagami-m fading channels and $m_0 = m = 0.5, 1, 1.5, 2$, with $M = 10$ interferers i.u.d. in a disk of radius $\mathcal{R} = 100$, reference link distance $r_0 = 5$ and reference receiver located at the center of the network, path-loss exponent $\alpha = 2.5$ and SINR threshold $\gamma_{\text{th}} = 0$ dB.

million simulation runs. We can see that the results from both the frameworks are the same and the curves overlap perfectly. In addition, we can see that the simulation results match perfectly with the our analytical results, which is to be expected since we are evaluating the outage probability exactly. These comparisons verify the accuracy of the proposed frameworks.

2.6.3 Importance of Having the Two Frameworks

As stated earlier in Remark 2, while both m_0 and m can take any (integer or non-integer) value in the MGF-based framework, m_0 is constrained to take integer values only (while m can take any value) in the RLPG-based framework. It is important to note that for small m_0, using the RLPG-based framework and interpolation for non-integer m_0 values either does not work or cannot provide accurate approximation results. This is illustrated in Figure 2.4 which plots the outage probability, P_{out}, versus the SNR, γ_0, for i.i.d. Nakagami-m fading channels ($m_0 = m = 0.5, 1, 1.5, 2$), path-loss exponent $\alpha = 2.5$ and the reference receiver located at the center of the disk. The results for $m_0 = m = 0.5$ and 1.5 are plotted using the MGF-based framework ((2.20) and (2.26)). The results for $m_0 = m = 1$ and 2 are plotted using the RLPG-based framework ((2.30)). For $m_0 = m = 1.5$ we also plot the arithmetic and the geometric means using the outage probabilities for $m_0 = m = 1$ and $m_0 = m = 2$, respectively. We

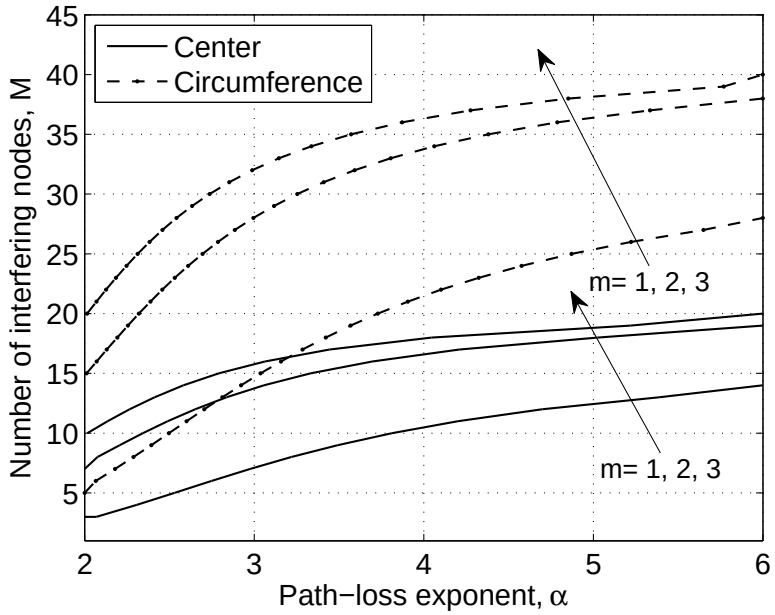

Figure 2.5: The number of interfering nodes M versus path-loss exponent α in order to meet a fixed outage probability constraint of $P_{\text{out}} = 0.05$ for the reference node located at the center and the circumference, respectively, of a disk region with radius $\mathcal{R} = 100$, i.i.d. Nakagami-m fading channels ($m = 1, 2, 3$), reference link distance $r_0 = 5$, SINR threshold $\gamma_{\text{th}} = 0$ dB and SNR $\gamma_0 = 20$ dB.

can see that the arithmetic and geometric means do not match the exact value of the outage probability, which illustrates that the interpolation approach [128, 129] does not work here. In addition, the result for $m_0 = m = 1$ does not provide a tight bound on the outage probability when $m_0 = m < 1$. These issues highlight the importance of having the two frameworks, which together can handle any value of m_0.

Note that the error floor observed in all the curves in Figure 2.4 is due to the fact that at high SNR, the interference term dominates the noise power term and causes the outage probability to become nearly constant (the $x-$axis in Figure 2.4 is the SNR, which is defined below (2.3) and not the SINR, which is defined in (2.3)).

2.6.4 Boundary Effects in a Disk Region

Figure 2.3 shows that for the disk region the minimum value of the outage probability occurs when the reference receiver is located at the circumference. This is due to the boundary effects. When the nodes are confined within a finite region, the nodes located close to the physical boundaries of the region experience different network characteristics, such as outage probability, compared to the nodes located near the center of the region. Note that the boundary effects are absent in PPP networks which assume an infinite region. In the following, we focus on the low outage probability regime and study the impact of the system parameters on the bound-

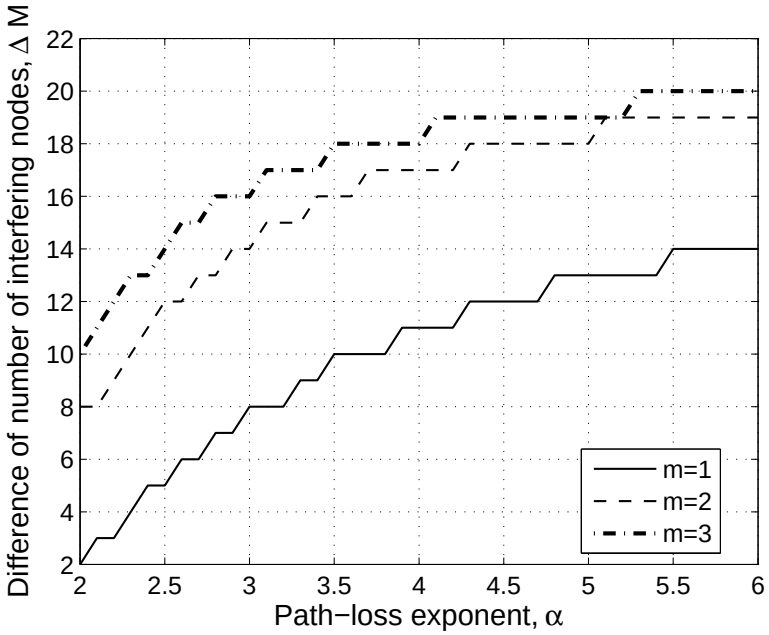

Figure 2.6: The difference in the number of interferers between the reference receiver located at the circumference and the center of a disk region, versus the path-loss exponent α, with the same parameters as in Figure 2.5.

ary effects by comparing the performance at the center and the boundary of disk and polygon regions, respectively.

Figure 2.5 plots the number of interfering nodes, M, that the network can accommodate in order to meet a fixed low outage probability constraint of $P_{\text{out}} = 0.05$ versus the path-loss exponent α for the two cases of the reference receiver located at the center and the circumference of a disk region, respectively, with radius $\mathcal{R} = 100$, i.i.d. Nakagami-m fading channels ($m = 1, 2, 3$), reference link distance $r_0 = 5$, SINR threshold $\gamma_{\text{th}} = 0$ dB and SNR $\gamma_0 = 20$ dB. We can see that as the path-loss exponent α increases the number of interfering nodes increases for all the curves. This is because as α increases, the total received power at the reference receiver Y_0 from all the interferers decreases more as compared to the received power at Y_0 from the desired transmitter X_0. In addition, as $m_0 = m$ increases, the number of interfering nodes increases for all the curves. This is because as the the fading becomes less severe, the received power at the reference receiver Y_0 from the desired transmitter X_0 increases more compared to the total received power from all the interferers. Comparing the curves for the center and the circumference, we can see that when Y_0 is located at the center of the disk region the network can only accommodate a small number of interferers in order to meet the low outage constraint. However, when Y_0 is located at the circumference of the disk region, the network can accommodate a larger number of interferers. This is because the circumference location is most impacted by the boundary effects and the reference receiver located at the cir-

cumference can only experience interference from certain surrounding regions inside the disk region. The figure also shows that the two sets of curves for the center and the circumference are not parallel, i.e., the impact of the boundary effects varies with the channel conditions. This is further explored in the next figure.

Figure 2.6 plots the difference in the number of interferers between the reference receiver located at the circumference and the center of a disk region, versus the path-loss exponent α for the scenario considered in Figure 2.5. The figure shows that for a fixed $m_0 = m$, an increase in the path-loss exponent enhances the impact of the boundary effects, e.g., for $m_0 = m = 1$ the difference is 2 interferers for $\alpha = 2$, which grows to 14 interferers for $\alpha = 6$. In addition, for a fixed α, an increase in $m_0 = m$ also enhances the impact of the boundary effects, e.g., for $\alpha = 4$, the difference is 11 interferers for $m_0 = m = 1$, which grows to 18 interferers for $m_0 = m = 3$. Note that the piece-wise nature of the curves in Figure 2.6 is due to the fact that the difference in the number of the interferers can only take integer values.

2.6.5 Boundary Effects in Polygon Regions

Figure 2.7 shows the number of interfering nodes M that the network can accommodate in order to meet a fixed low outage probability constraint of $P_{\text{out}} = 0.05$ versus the number of sides L for the two cases of the reference receiver located at the center and a vertex of a $L = 3, 4, 5, 6, 7, 8, 9$-sided convex polygon having a fixed area $|\mathcal{A}| = \pi 100^2$, with i.i.d. Nakagami-$m$ fading channels ($m_0 = m = 3$), path-loss exponent $\alpha = 2.5$, reference link distance $r_0 = 5$, SINR threshold $\gamma_{\text{th}} = 0$ dB and SNR $\gamma_0 = 20$ dB. When the reference receiver is located at the center of the polygon, the impact of the boundary effects is negligible and the number of interferers that the network can accommodate is 14, irrespective of the number of sides[3]. This is consistent with the fact that we have considered a large-scale finite network and the surrounding environment for the reference receiver located at the center of the L-sided convex polygon is quite the same, regardless of the number of sides. When the reference receiver is located at a vertex of the L-sided convex polygon, the number of interferers decreases as the number of sides L increases. This shows that the impact of the number of sides on the boundary effects depends on the location of the reference receiver. We can see that for $L = 3$ the network can accommodate the highest number of interferers while meeting the low outage probability constraint of $P_{\text{out}} = 0.05$. This can be intuitively explained as follows. For $L = 3$, since the area of the L-sided polygon is fixed, $f_R(r)$ has the longest tail. In addition, the interior angle formed at the vertex is the smallest. Consequently, the interfering nodes are more likely to located further away from the reference receiver located at a vertex, which leads to better performance in terms of the number of interferers that the network can accommodate.

[3]For the case of the reference receiver located at the center of a disk region (which can be regarded as a $L = \infty$-sided convex polygon) with the same area, the number of interferers is also 14.

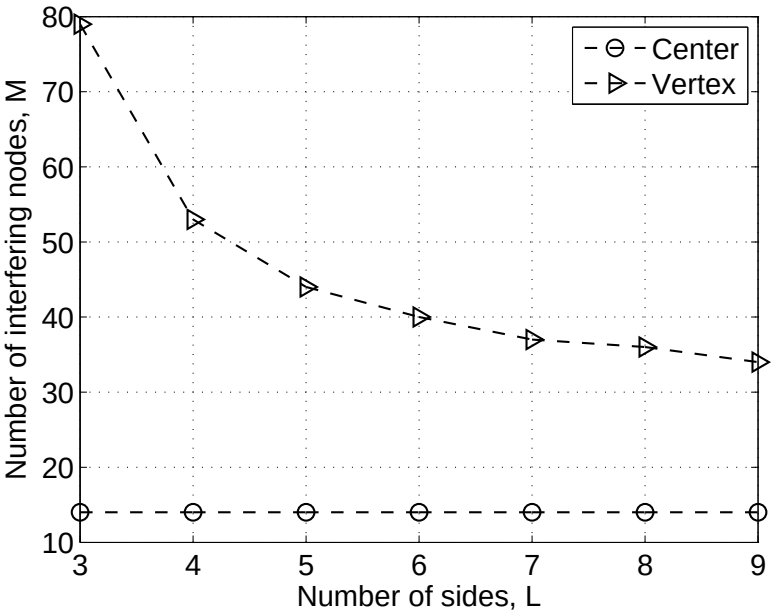

Figure 2.7: The number of interfering nodes M versus the number of sides L in order to meet a fixed low outage probability constraint of $P_{\text{out}} = 0.05$ for the reference node located at the center and the corner, respectively, of a L-sided polygon ($L = 3, 4, 5, 6, 7, 8, 9$) having a fixed area $|\mathcal{A}| = \pi 100^2$, with i.i.d. Nakagami-$m$ fading channels ($m_0 = m = 3$), path-loss exponent $\alpha = 2.5$, reference link distance $r_0 = 5$, SINR threshold $\gamma_{\text{th}} = 0$ dB and SNR $\gamma_0 = 20$ dB.

In addition, Figure 2.7 shows that as L increases, the difference in the number of interferers between the two cases of the reference receiver located at the vertex and the center decreases. This shows that the relative impact of the boundary effects becomes less significant as the number of sides increases.

2.6.6 Outage Probability in an Arbitrarily Shaped Convex Region

Figure 2.8 plots the outage probability, P_{out}, versus the SNR, γ_0, with arbitrary locations of the reference receiver in the arbitrarily shaped finite region ($|\mathcal{A}| = 13143$) defined in Figure 2.2, i.i.d. Rayleigh fading channels ($m_0 = m = 1$) and path-loss exponent $\alpha = 2.5$. We consider and compare the following cases for the reference receiver located at: (i) vertex V_2 at $(173.2, 0)$ (ii) vertex V_3 at $(50.73, 122.474)$ (iii) mid point of side S_2 at $(111.97, 61.24)$ and (iv) intersection point of the diagonals at $(33.4, 80.7)$. For comparison, we also plot the outage probability assuming a PPP node distribution with a node density $\lambda = 10/13143 = 7.6086 \times 10^{-4}$ using the result from [130], which is given below

$$P_{\text{out}} = 1 - \exp\left(-\frac{\gamma_{\text{th}}}{\gamma_0}\right) \exp\left(-\lambda \pi r_0^2 \gamma_{\text{th}}^{\frac{2}{\alpha}} \frac{2\pi}{\alpha} \csc\left(\frac{2\pi}{\alpha}\right)\right). \tag{2.38}$$

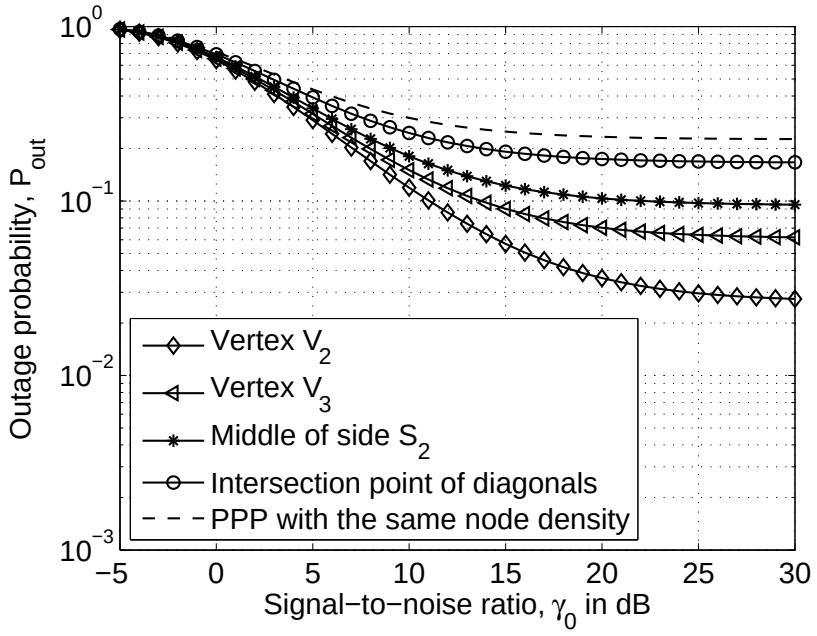

Figure 2.8: Outage probability, P_{out}, versus the signal-to-noise ratio, γ_0, with arbitrary locations of the reference receiver inside the arbitrarily shaped finite region defined in Figure 2.2 having area $|\mathcal{A}| = 13143$, $M = 10$ interferers, i.i.d. Rayleigh fading channels ($m_0 = m = 1$), path-loss exponent $\alpha = 2.5$ and SINR threshold $\gamma_{\text{th}} = 0$ dB. For the PPP node distribution, the node density is $\lambda = 10/13143 = 7.6086 \times 10^{-4}$ (which is the same as for the BPP).

At high SNR, the error floor observed in all the curves is because of the same reasons as explained before. We can see that the outage probabilities for the four cases are completely different as the location of the reference receiver and consequently the boundary effects are different in each case. The outage probability is the highest for case (iv) as this location is well inside the region and is less impacted by the boundary effects. The outage probability is the lowest for case (i) as the interior angle formed at V_2 vertex is the smaller than that at vertex V_3. Thus, interferers are more likely to be located further away from the reference receiver located at V_2 vertex. We can see that the PPP result, which does not take boundary effects into account, is completely different from the four cases considered and provides an extremely loose upper bound for the outage probability. This re-iterates the importance of the proposed frameworks, which allow the outage probability at any arbitrary location of a finite wireless network with arbitrary shape to be exactly determined.

2.7 Summary

In this chapter, we examined the performance of an arbitrarily located reference node inside an arbitrarily shaped ad-hoc network, where the locations of interfering ad-hoc users are mod-

eled as the BPP. We developed two general frameworks allowing to analytically compute the outage probability at the reference node for such a network. We also proposed an algorithm to derive the distribution function of the distance between an interfering node and the reference node, which is key in determining the outage probability. Our results highlighted the importance of characterizing the location-dependent performance, and they also allowed us to proper understand the effects of system parameters on the boundary effects.

Chapter 3

Performance Analysis of Arbitrarily Shaped Underlay Cognitive Networks

In Chapter 2, we have developed the general frameworks to calculate the outage probability at an arbitrarily location within an arbitrarily shaped ad-hoc network region. It has been shown that for an arbitrarily shaped finite region, the aggregate interference and the outage probability are strongly influenced by the shape of the region and the position of the typical user.

In this chapter, we apply the developed techniques to study the performance of a more complex underlay cognitive network with an arbitrarily shaped region. We consider different SU activity protocols to limit the number of active SUs, in order to maintain the interference threshold requirement at the primary receiver at an arbitrary location. For such network systems, we propose a framework, based on the MGF of the interference due to a random SU, to analytically compute the outage probability and statistics of interference at the primary user with SU activity protocols. Additionally, we derive the average number of active SUs to examine the performance of secondary users, which has been largely ignored by previous works. With the derived analytical expressions, we investigate the average number of active SUs for the different SU activity protocols, subject to a given outage probability constraint at the primary receiver, and regard it as an analytical approach to compare the effect of different SU activity protocols on the performance of the primary and secondary networks. Under fully uncorrelated channel situation, we observe that the guard zone protocol which requires long term sensing can support the highest number of active SUs. In terms of short term sensing, our proposed cooperation-based protocol can improve the average number of active SUs, compared to the threshold-based protocol.

This chapter is organized as follows. Section 3.1 presents the detailed system model and assumptions and describes the three different SU activity protocols, including the proposed cooperation-based protocol. The proposed mathematical framework is presented in Section 3.2. The analysis for the interference and the average number of active SUs is presented in Section 3.3 and Section 3.4, respectively. Numerical and simulation results to study the

aggregate interference, outage probability and average number of active SUs are discussed in Section 3.5. Finally, conclusions are presented in Section 3.6.

3.1 System Model

We consider an underlay cognitive network with a PU link, comprising of a PU transmitter (PU-Tx) and a PU receiver (PU-Rx) separated by a distance r_0, and M SUs. The network region $\mathcal{A}$ is an arbitrarily shaped finite region, where $\mathcal{A} \subset \mathbb{R}^2$ and $\mathbb{R}^2$ denotes the two-dimensional Euclidean space. We do not place any restriction on the location of the PU-Tx and PU-Rx and they can be located anywhere inside the network region $\mathcal{A}$. A primary exclusion zone $\mathcal{B}$, with radius ϵ, is formed around the PU-Rx and no active user is allowed to enter this region [131]. The SU locations are modeled according to a uniform Binomial Point Process, i.e., the M SUs are independently and uniformly distributed at random inside the region $\mathcal{A}'$, where $\mathcal{A}' = \mathcal{A} \setminus \mathcal{B}$.

The SUs decide whether to transmit or not depending on the adopted SU activity protocol (discussed later in this section). We assume that all the nodes operate in the frequency division duplex mode. Similar to [63], we assume that in order to know the signal strength to PU-Rx each SU receives a signal transmitted by PU-Rx via a sensing channel. We assume that this sensing channel (from PU-Rx to SU) and the SU transmitting (i.e., interfering) channel (from SU to PU-Rx) are well separated in the frequency band so that these two channels can be regarded as fully uncorrelated.

Let the random variable R_i $(i = 1, 2, \ldots, M)$ denote the random distance between the i-th SU and the PU-Rx with probability density function $f_{R_i}(r_i)$. We denote the transmit power of the PU-Tx as P_{T_0}, the transmit power of each SU as P_{T_i} and the transmit power of PU-Rx as P_{T_S}. We assume that all users have a single antenna and the wireless communication channel is modeled as a path-loss and fading channel. Let G_i represent the instantaneous power gain due to fading on the SU transmitting channel from i-th SU to the PU-Rx with fading distribution function $f_{G_i}(g_i)$ and H_i represent the instantaneous fading power gain on the sensing channel with the distribution function $f_{H_i}(h_i)$.

For the above setup, the interference at the PU-Rx generated from the i-th SU is given by

$$I_i = P_{T_i} G_i R_i^{-\alpha} \mathbf{1}_{(\text{condition})}, \tag{3.1}$$

where α is the path-loss exponent which is typically in the range $2 \leq \alpha \leq 6$ [115]. The

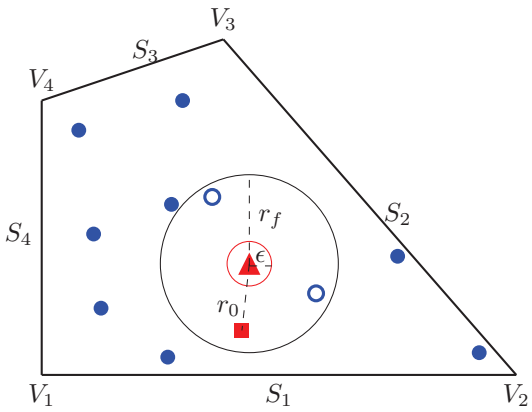

(a) Guard zone protocol with radius r_f and primary exclusion zone radius ϵ.

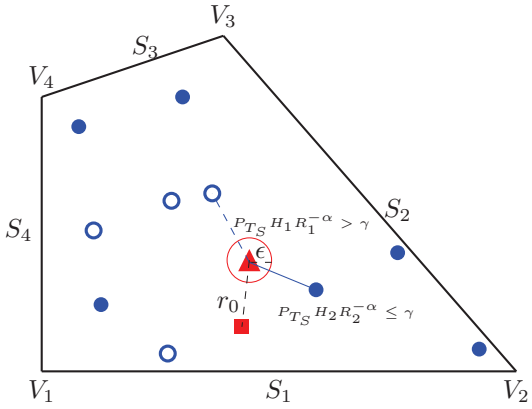

(b) Threshold-based protocol with activation threshold γ.

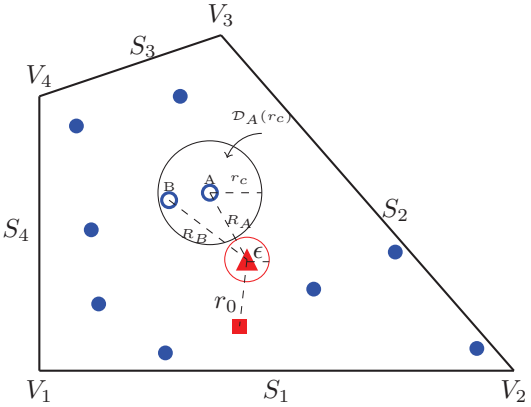

(c) Cooperation-based protocol with activation threshold γ and cooperation range r_c .

Figure 3.1: Illustration of secondary user spatial activity protocols in underlay cognitive network (▲ = interfered PU-Rx, ■ = PU-Tx, ○ = inactive secondary user, ● = active secondary user). S_j and V_j ($j = 1, 2, 3, 4$) denote the side and vertex, respectively.

indicator function is given by

$$\mathbf{1}_{(\text{condition})} = \begin{cases} 1, & \text{if condition is true;} \\ 0, & \text{else if condition is false;} \end{cases} \tag{3.2}$$

where the “condition" depends on the different SU activity protocols and the explicit expressions for each protocol are given in (3.4), (3.5) and (3.6), respectively. In addition, although the unbounded path-loss model is used in (3.1), the singularity at $R_i = 0$ and the amplification of the transmitted signal are avoided because of the primary exclusion zone around the PU-Rx, i.e., the random distance R_i is always greater than ϵ ($\epsilon \geq 1$) [36].

The aggregate interference at PU-Rx is given by

$$I_{\text{agg}} = \sum_{i=1}^{M} I_i = \sum_{i=1}^{M} P_{T_i} G_i R_i^{-\alpha} \mathbf{1}_{(\text{condition})}. \tag{3.3}$$

In the following subsections, we present the definition of each SU activity protocol.

3.1.1 Guard Zone Protocol

The guard zone protocol was employed in [38, 39]. In this protocol, the SUs are permitted to enter the guard zone region but once a SU intrudes into it, it is prohibited from transmitting. This is illustrated in Figure 3.1(a), where there is a guard zone region around the PU-Rx with radius r_f. Consequently, the two SUs that are inside this region are inactive and do not generate any interference to the PU-Rx. The aggregate interference under the guard zone protocol can be written as

$$I_{\text{agg}} = \sum_{i=1}^{M} P_{T_i} G_i R_i^{-\alpha} \mathbf{1}_{\left(R_i > r_f\right)}. \tag{3.4}$$

3.1.2 Threshold-based Protocol

The threshold-based protocol was proposed in [63]. In this protocol, each SU receives the instantaneous signal power transmitted by the PU-Rx on the sensing channel. If the received instantaneous signal power at the i-th SU is greater than the activation threshold ξ, i.e., $P_{T_S} H_i R_i^{-\alpha} > \xi$, it becomes silent and does not interfere with the PU-Rx. Otherwise, it is permitted to transmit, as illustrated in Figure 3.1(b). Hence, for the threshold-based protocol, the aggregate interference can be written as

$$I_{\text{agg}} = \sum_{i=1}^{M} P_{T_i} G_i R_i^{-\alpha} \mathbf{1}_{\left(P_{T_S} H_i R_i^{-\alpha} \leq \xi\right)}. \tag{3.5}$$

3.1.3 Cooperation-based Protocol

This is the new protocol proposed in this chapter and is illustrated in Figure 3.1(c). The basic idea of this protocol is inspired from the cooperative spectrum sensing in interweave cognitive networks, where cooperation among nodes helps to improve the detection of licensed spectrum occupancy [36, 61].[1]

In the proposed cooperation-based protocol for underlay cognitive networks, each SU receives the instantaneous signal power transmitted by the PU-Rx on the sensing channel and forms an initial decision on activation. Then this initial decision is broadcast to other SUs. For analytical convenience, we assume that, for each SU, it can only correctly receive the initial decisions from other SUs within a certain range, which is known as its cooperation range r_c. Finally, in order to decide whether it is active or not, each SU applies the logical AND operation on the received initial decisions from other cooperating SUs and its own initial decision. Consequently, for a considered SU, it is permitted to be active as long as its preliminary decision is to be active, and the initial decision of all SUs which fall into this SU's cooperation range is also to be active. For example, considering SU node A in Figure 3.1(c), there is only SU node B located inside its cooperation range. Although the preliminary decision for node A may be to be active, node A can be finally in inactive state if the preliminary decision of node B is to be inactive. Mathematically, the aggregate interference generated at the PU-Rx is

$$I_{\text{agg}} = \sum_{i=1}^{M} P_{T_i} G_i R_i^{-\alpha} \mathbf{1}_{(\Pi_d(\mathcal{D}_i(r_c)) \cap \mathcal{A}' = \emptyset)}, \tag{3.6}$$

where Π_d denotes the set of SUs whose received instantaneous signal power on the sensing channel is greater than the activation threshold ξ, $\mathcal{D}_i(r_c)$ represents the disk cooperation region centered at the i-th SU and $\emptyset$ denotes the null set. Note that when $r_c = 0$, the cooperation-based protocol is the same as the threshold-based protocol. Thus, the proposed cooperation-based protocol includes the threshold-based protocol as a special case.

Remark 4. *Both the cooperation-based and threshold-based protocols require the SU to receive the instantaneous signal power transmitted by the PU-Rx on the sensing channel. As such, they are much more applicable in practice. However, the guard zone protocol requires the SU to know the instantaneous signal power on the sensing channel over a relatively long period of time and then average it to determine its distance to the PU-Rx, before deciding whether to transmit or not.*[2] *As such, this protocol is not suitable for the scenarios where the SUs need to transmit without too much delay.*

[1] The notion of cooperation among SUs is also similar in spirit to base station cooperation in cellular networks [132].

[2] Alternatively, the guard zone protocol can also be implemented using cooperative localization techniques [133].

3.2 Mathematical Framework

In this section, we present the proposed mathematical framework to characterize the interference and outage probability at the PU-Rx in underlay cognitive networks with different SU activity protocols. The aggregate interference from the secondary network in (3.3) is a stochastic process that strongly relies on the random location of the SUs inside the arbitrarily shaped finite cognitive network region and the random fading channel gains. Since there is no available general expression for the PDF of the aggregate interference [21, 71], we adopt the moment generating function approach to analyze the interference and outage probability at the PU-Rx in this chapter. Previous work [62, 63] has also adopted the MGF approach. However, their focus is on analysing the statistics of the aggregate interference in the primary network only and the results are limited to specific, e.g., annulus-shaped regions. We consider arbitrarily shaped cognitive network regions and analyze the performance in both the primary network (i.e., the aggregate interference in Section 3.3) and the secondary network (i.e., the average number of active SUs in Section 3.4).

3.2.1 Assumptions

In this work, we consider that the nodes are independently and uniformly distributed inside the network region $\mathcal{A}'$, which results in the distribution function of R_i being the same for all i. Moreover, the fading gain on all communication channels is independently and identically distributed Nakagami-m fading. This type of fading is widely considered in the wireless communications literature [115]. The transmit power for different SUs are assumed to be the same. Consequently, the distribution of interference from i-th SU becomes identical and we can drop the index i in the P_{T_i}, I_i, R_i, G_i, H_i and let $f_{R_i}(r_i) = f_R(r)$, $f_{G_i}(g_i) = f_G(g)$ and $f_{H_i}(h_i) = f_H(h)$.

For Nakagami-m fading, the distribution of the power gain on the SU transmitting channel and the sensing channel can be modeled by a Gamma distribution as [115]

$$f_G(g) = \frac{g^{m_g-1} m_g^{m_g}}{\Gamma[m_g]} \exp(-m_g g), \tag{3.7}$$

$$f_H(h) = \frac{h^{m_h-1} m_h^{m_h}}{\Gamma[m_h]} \exp(-m_h h), \tag{3.8}$$

where m_g and m_h represent the fading parameters, which control the severity of the fading. Note that $m_g = m_h = 1$ corresponds to Rayleigh fading channels. In addition, the n-th moment of the fading power gain on the SU transmitting channel, which is needed in the

analysis in Section 3.3, is available in closed-form as [134]

$$\mathbb{E}_G\left\{G^n\right\} = \frac{(m_g + n - 1)!}{m_g^n (m_g - 1)!}. \tag{3.9}$$

3.2.2 Distance Distributions

The proposed formulation relies on the knowledge of the distance distribution $f_R(r)$, i.e., the PDF of the distance of a random SU from the PU-Rx. For a disk region, $f_R(r)$ is well known [39, 57, 60, 61, 62, 63]. For an L-sided arbitrarily shaped convex polygon, $f_R(r)$ can be a complicated piece-wise function with at most $2L$ piece-wise terms [65]. The number of piece-wise terms depends on the number of unique distances between the location of the reference node and all the sides and vertices, respectively, of the polygon region. Recently, [88] proposed an algorithm to determine $f_R(r)$ for the case of a random node located anywhere inside an arbitrarily shaped convex polygon. This algorithm is used in this work to determine $f_R(r)$ in closed-form. Once $f_R(r)$ is determined using the algorithm in [88], the expectation $\mathbb{E}_R\left\{R^{-n\alpha}\right\}$ involving the random variable R, which is needed in the analysis in Section 3.3, can be easily calculated in closed-form.

3.2.3 Moment Generating Function

In general, the moment generating function of the aggregate interference is defined as [115]

$$\mathcal{M}_{I_{\text{agg}}}(s) = \mathbb{E}_{I_{\text{agg}}}\left\{\exp\left(-sI_{\text{agg}}\right)\right\}, \tag{3.10}$$

where $\mathbb{E}_{I_{\text{agg}}}\{\cdot\}$ denotes the expectation with respect to the random variable I_{agg}. Assuming that the interference from each SU is independent and identical, the moment generating function of the aggregate interference in (3.10) can be re-written as [115]

$$\mathcal{M}_{I_{\text{agg}}}(s) = \left(\mathcal{M}_I(s)\right)^M, \tag{3.11}$$

where I denotes the interference generated by a random SU and $\mathcal{M}_I(s) = \mathbb{E}_I\left\{\exp(-sI)\right\}$ corresponds to the MGF of I.

3.2.4 n-th Cumulant

The n-th cumulant of the aggregate interference can be written in terms of the MGF of the aggregate interference as [115]

$$\begin{aligned}\kappa_{I_{\text{agg}}}(n) =&(-1)^n \left.\frac{\mathrm{d}^n \ln \mathcal{M}_{I_{\text{agg}}}(s)}{\mathrm{d}s^n}\right|_{s=0} \\ =&(-1)^n M \left.\frac{\mathrm{d}^n \ln \mathcal{M}_{I}(s)}{\mathrm{d}s^n}\right|_{s=0} \\ =&M\kappa_I(n) \\ =&M\left(\mu_I(n) - \sum_{j=1}^{n-1}\binom{n-1}{j-1}\kappa_I(j)\mu_I(n-j)\right), \end{aligned} \tag{3.12}$$

where the last step comes from the recursive moment-cumulant relationship [57], and $\kappa_I(n)$ and $\mu_I(n)$ represent the n-th cumulant and n-th moment of the interference from a random SU respectively. Note that $\mu_I(n)$ can also be directly related to $\mathcal{M}_I(s)$ by [115]

$$\mu_I(n) = (-1)^n \left.\frac{\mathrm{d}^n \mathcal{M}_I(s)}{\mathrm{d}s^n}\right|_{s=0}. \tag{3.13}$$

With the derived formula of the n-th cumulant/n-th moment of the interference, we can investigate the statistical behavior of the aggregate interference. A detail study has been presented in [135], which is omitted here. In addition, the n-th moment is closely related to the average number of active SUs, which will be shown in Section 3.4.

3.2.5 Outage Probability at the PU-Rx

The outage probability at the PU-Rx is an important metric to evaluate the impact of SU activity protocols on the performance of the primary users over fading channels. It is given by

$$P_{\text{out}} = \Pr\left(\text{SINR} < \gamma_{\text{th}}\right) = \Pr\left(\frac{P_{T_0} r_0^{-\alpha} G_0}{I_{\text{agg}} + \mathcal{N}} < \gamma_{\text{th}}\right), \tag{3.14}$$

where γ_{th} is the SINR threshold and $\mathcal{N}$ is the AWGN power.

In this work, we are interested in the spatially averaged outage probability which is spatially averaged over both the possible location of the SUs and the fading channels. When the fading on the desired link (from PU-Tx to PU-Rx) follows the general distribution defined in [31, (9)] (an important special case of which is Nakagami-m fading with integer m value), we can employ the RLPG-based framework proposed in [88] to evaluate the spatially averaged outage probability. The basic principle of this approach is to first condition on the interference and express the outage probability in terms of the CDF of the reference link's fading power gain. The conditioning on the interference is then removed first by removing the condition-

ing on the fading power gains of the interferers and then removing the conditioning on the locations of the interferers. For Nakagami-m fading channels, the spatially averaged outage probability is given by [88]

$$P_{\text{out}} = 1 - \exp\left(-m_0 \frac{\gamma_{\text{th}}}{\gamma_0}\right) \sum_{k=0}^{m_0-1} \frac{m_0^k}{k!} \sum_{j=0}^{k} \binom{k}{j} \left(\frac{\gamma_{\text{th}}}{\gamma_0}\right)^{k-j} \left(\frac{\gamma_{\text{th}} r_0^{\alpha}}{P_{T_0}}\right)^{j} \times \sum_{t_1+t_2\ldots+t_M=j} \binom{j}{t_1, t_2, \ldots, t_M} \prod_{i=1}^{M} \mathbb{E}_I \left\{ \exp\left(-m_0 \frac{\gamma_{\text{th}} r_0^{\alpha}}{P_{T_0}} I\right) (I)^{t_i} \right\}, \tag{3.15}$$

where $\gamma_0 = \frac{P_{T_0} r_0^{-\alpha}}{\mathcal{N}}$ indicates the average SNR and m_0 denotes the fading parameter on the desired link.

Note the MGF of the interference due to a random SU is $\mathcal{M}_I(s) = \mathbb{E}_I\{\exp(-sI)\}$. Its t_i-th derivative with respect to s is $\frac{\mathrm{d}^{t_i}\mathcal{M}_I(s)}{\mathrm{d}s^{t_i}} = \mathbb{E}_I\left\{(-I)^{t_i}\exp(-sI)\right\}$. By substituting $s = m_0 \frac{\gamma_{\text{th}} r_0^{\alpha}}{P_{T_0}}$ and after rearranging, the expectation term in (3.15) can be expressed in terms of the MGF of the interference due to a random SU as

$$\mathbb{E}_I \left\{ \exp\left(-m_0 \frac{\gamma_{\text{th}} r_0^{\alpha}}{P_{T_0}} I\right) (I)^{t_i} \right\} = (-1)^{t_i} \left. \frac{\mathrm{d}^{t_i}\mathcal{M}_I(s)}{\mathrm{d}s^{t_i}} \right|_{s=m_0 \frac{\gamma_{\text{th}} r_0^{\alpha}}{P_{T_0}}}. \tag{3.16}$$

Examining (3.11), (3.12) and (3.15), we can see that the proposed mathematical formulation depends on the MGF of the interference due to a random SU $\mathcal{M}_I(s)$. This is determined for the different SU activity protocols in the next section.

3.3 Interference Analysis

In this section, we derive the general expressions characterizing the MGF of the interference from a random SU for the different SU activity protocols.

3.3.1 Guard Zone Protocol

For this protocol, the SUs within the guard zone region do not transmit. The main result is summarized in Theorem 1.

Theorem 1. *For the guard zone protocol, the MGF of the interference at an arbitrarily located PU-Rx due to an independently and uniformly distributed SU inside an arbitrarily shaped finite region is*

$$\mathcal{M}_I(s) = \int_0^{\infty} \int_{r_f}^{r_{max}} \exp\left(-sP_T g r^{-\alpha}\right) f_R(r) f_G(g)\, \mathrm{d}r\, \mathrm{d}g + F_R(r_f), \tag{3.17}$$

where $F_R(\cdot)$ represents the cumulative distribution function of the distance of a random SU from the PU-Rx, which can be determined by the algorithm in [88].

Corollary 1. *For the guard zone protocol, the n-th moment of the interference at an arbitrarily located PU-Rx due to an independently and uniformly distributed SU inside an arbitrarily shaped finite region is*

$$\mu_I(n) = P_T^n \mathbb{E}_G\left\{G^n\right\} \mathbb{E}_R^{pt}\left\{-n\alpha, r_f, r_{max}\right\}, \tag{3.18}$$

where $\mathbb{E}_R^{pt}\{\cdot\}$ denotes the partial moment of R.

Proof of Theorem 1 and Corollary 1: See Appendix B.1.

Remark 5. (3.17) *and* (3.18) *can also be used to obtain the results for the full activity protocol in which no activity constraint is imposed on SUs and all the SUs are in active status. In the full activity protocol, a SU located within the maximum range of ϵ and r_{max} generates interference to the PU-Rx. In the guard zone protocol, a SU located within the smaller range of r_f and r_{max} generates interference to the PU-Rx. Thus, when the guard zone range r_f is set to equal to ϵ, the guard zone protocol reduces to the full activity protocol. Therefore, the MGF and n-th cumulant results for the full activity protocol are the same as* (3.17) *and* (3.18) *with r_f replaced by ϵ.*

Special Case of a Regular L-sided Polygon: Consider the special case that the PU-Rx is located at the center of a regular L-sided polygon which is inscribed in a circle of radius $\mathcal{R}$. In this case, the distance distribution function is given by [65]

$$f_R(r) = \frac{1}{|\mathcal{A}'|}\begin{cases} 2\pi r, & \epsilon \le r \le \mathcal{R}_p; \\ 2\pi r - 2Lr\arccos\left(\frac{\mathcal{R}_p}{r}\right), & \mathcal{R}_p \le r \le \mathcal{R}; \end{cases} \tag{3.19}$$

where $|\mathcal{A}'| = \frac{1}{2}L\mathcal{R}^2\sin\left(\frac{2\pi}{L}\right) - \pi\epsilon^2$ denotes the area of the underlay secondary network region, $\theta = \frac{\pi(L-2)}{L}$ is the interior angle between two adjacent sides of the polygon and $\mathcal{R}_p = \mathcal{R}\sin\left(\frac{\theta}{2}\right)$ is the perpendicular distance from the center of the polygon to any side. Substituting (3.19) and (3.7) into (3.17) and (3.18), yields the following results

$$\begin{aligned}\mathcal{M}_I(s) =& \frac{\pi\left(\mathcal{R}^2\,{}_2F_1\left[m_g, -\frac{2}{\alpha}; \frac{-2+\alpha}{\alpha}; -\frac{\mathcal{R}^{-\alpha}sP_T}{m_g}\right] - r_f^2\,{}_2F_1\left[m_g, -\frac{2}{\alpha}; \frac{-2+\alpha}{\alpha}; -\frac{r_f^{-\alpha}sP_T}{m_g}\right] + r_f^2 - \epsilon^2\right)}{|\mathcal{A}'|} \\ & - \int_{\mathcal{R}_p}^{\mathcal{R}} \frac{2m^m Lr}{\left(m + r^{-\alpha}sP_T\right)^m}\arccos\left(\frac{\mathcal{R}_p}{r}\right)\mathrm{d}r,\end{aligned} \tag{3.20}$$

$$\mu_I(n) = P_T^n \frac{(m_g+n-1)!}{m_g^n(m_g-1)!} \frac{2\left(\pi\left(\mathcal{R}^{2-n\alpha} - r_f^{2-n\alpha}\right) - L\varphi\left(\mathcal{R}\right) + L\varphi\left(\mathcal{R}_p\right)\right)}{|\mathcal{A}'|(2-n\alpha)}, \tag{3.21}$$

where $\varphi(r) = \frac{(1-n\alpha)\left((1+n\alpha)r^3 \arccos\left(\frac{\mathcal{R}_p}{r}\right) + \mathcal{R}_p^3 {}_2F_1\left[\frac{1}{2}, \frac{n\alpha+1}{2}; \frac{n\alpha+3}{2}; \frac{\mathcal{R}_p^2}{r^2}\right]\right) - \mathcal{R}_p(1+n\alpha)r^2 {}_2F_1\left[-\frac{1}{2}, \frac{n\alpha-1}{2}; \frac{n\alpha+1}{2}; \frac{\mathcal{R}_p^2}{r^2}\right]}{(n\alpha-1)(n\alpha+1)r^{1+n\alpha}}$ and r_f is assumed to be less than $\mathcal{R}_p$.

Note that while (3.20) does not have a closed-form result due to the integration involving the $\arccos(\cdot)$ term, it can be easily computed numerically.

Remark 6. *When $L \to \infty$, $\mathcal{R}_p \to \mathcal{R}$ and the regular L-sided polygon approaches a disk region. The disk region or annulus-shaped region with centered PU-Rx and full activity protocol is the most popular scenario and has been widely analyzed in previous works [39, 57, 62, 63]. Under Nakagami-m fading assumption, the MGF calculated from* (3.20) *by setting $r_f = \epsilon$ (i.e., full activity protocol) and $\mathcal{R}_p = \mathcal{R}$ (i.e., the integration term in* (3.20) *reduces to zero) is identical to the result in [57, eq. (6)]. In addition, the n-th cumulant calculated from* (3.21) *(replacing r_f by ϵ and $\varphi\left(\mathcal{R}_p\right) = \varphi\left(\mathcal{R}\right)$) and* (3.12) *is the same as the result from [57].*

3.3.2 Threshold-based Protocol

In this protocol, the activity of each SU depends on the instantaneous signal power received on the sensing channel. The main result is summarized in Theorem 2.

Theorem 2. *For the threshold-based protocol, assuming the sensing channel is fully uncorrelated with the SU transmitting channel, the MGF of the interference at an arbitrarily located PU-Rx due to an independently and uniformly distributed SU inside an arbitrarily shaped finite region is*

$$\begin{aligned}\mathcal{M}_I(s) = &\int_0^{\infty}\int_{\epsilon}^{r_{max}} \exp\left(-sP_T g r^{-\alpha}\right) F_H\left(\frac{\xi r^{\alpha}}{P_{T_S}}\right) f_R(r) f_G(g)\,\mathrm{d}r\,\mathrm{d}g + 1 \\ &- \int_{\epsilon}^{r_{max}} F_H\left(\frac{\xi r^{\alpha}}{P_{T_S}}\right) f_R(r)\,\mathrm{d}r,\end{aligned} \tag{3.22}$$

where $F_H(\cdot)$ denotes the CDF of the fading power gain on sensing channel.

Corollary 2. *For the threshold-based protocol, the n-th moment of the interference at an arbitrarily located PU-Rx due to an independently and uniformly distributed SU inside an arbitrarily shaped finite region is*

$$\mu_I(n) = P_T^n \mathbb{E}_G\left\{G^n\right\} \mathbb{E}_R\left\{F_H\left(\frac{\xi R^{\alpha}}{P_{T_S}}\right) R^{-n\alpha}\right\}. \tag{3.23}$$

Proof of Theorem 2 and Corollary 2: See Appendix B.2.

Special Case of regular L-sided Polygon: Substituting the PDFs $f_R(r)$ in (3.19) and $f_G(g)$ in (3.7) into (3.22) and (3.23), we can obtain the MGF and the n-th moment for this special case. For simplicity, we only show the n-th moment result, which is given by

$$\mu_I(n) = P_T^n \frac{(m_g+n-1)!}{m_g^n(m_g-1)!}\frac{2\pi}{|\mathcal{A}'|(2-n\alpha)}\left(\mathcal{R}^{2-n\alpha}\frac{\Gamma[m_h,0,m_h\xi\mathcal{R}^\alpha/P_{T_S}]}{\Gamma[m_h]}\right.$$
$$-\epsilon^{2-n\alpha}\frac{\Gamma[m_h,0,m_h\xi\epsilon^\alpha/P_{T_S}]}{\Gamma[m_h]} - \left(\frac{m_h\xi}{P_{T_S}}\right)^{n-\frac{2}{\alpha}}\frac{\Gamma[m_h-n+\frac{2}{\alpha},m_h\xi\epsilon^\alpha/P_{T_S},m_h\xi\mathcal{R}^\alpha/P_{T_S}]}{\Gamma[m_h]}$$
$$\left.-\frac{L(2-n\alpha)}{\pi}\int_{\mathcal{R}_p}^{\mathcal{R}}\frac{\Gamma\left[m_h,0,\frac{m_h\xi r^\alpha}{P_{T_S}}\right]}{\Gamma[m_h]}r^{1-n\alpha}\arccos\left(\frac{\mathcal{R}_p}{r}\right)\mathrm{d}r\right), \tag{3.24}$$

where $\Gamma[\cdot,\cdot,\cdot]$ is the generalized incomplete gamma function.

Remark 7. *For the disk region,* (3.24) *with* $L=\infty$ *(i.e., ignoring the integration part in* (3.24)*) is equivalent to the result in [63]. However, the method of calculating the n-th cumulant in [63] is only applicable for the special case that PU-Rx is located at the center of the disk region.*

3.3.3 Cooperation-based Protocol

For the cooperation-based protocol, the activity of each SU is determined by itself as well as other SUs within its cooperative range. Thus, the interference due to each SU is not independent and (3.11) is not strictly valid. The analysis in the presence of correlated interference is an important open research problem. In this chapter, we still use (3.11) to derive approximate analytical results for the cooperation-based protocol. We show that these results are accurate under certain conditions, which will be discussed in detail in Section 3.5. The main result is summarized in Proposition 1 below.

Proposition 1. *For the cooperation-based protocol, the MGF of the interference at an arbitrarily located PU-Rx due to an independently and uniformly distributed SU inside an arbitrarily shaped finite region is approximated by*

$$\mathcal{M}_I(s) \approx 1 + \int_0^\infty\int_\epsilon^{r_{max}} \exp\left(-sP_Tgr^{-\alpha}\right) F_H\left(\frac{\xi r^\alpha}{P_{T_S}}\right)\left(\frac{\left|\mathcal{A}'-\pi r_c^2\right|}{|\mathcal{A}'|}+\frac{\pi r_c^2}{|\mathcal{A}'|}F_H\left(\frac{\xi r^\alpha}{P_{T_S}}\right)\right)^{M-1}$$
$$\times f_R(r)f_G(g)\,\mathrm{d}r\,\mathrm{d}g - \int_\epsilon^{r_{max}} F_H\left(\frac{\xi r^\alpha}{P_{T_S}}\right)\left(\frac{\left|\mathcal{A}'-\pi r_c^2\right|}{|\mathcal{A}'|}+\frac{\pi r_c^2}{|\mathcal{A}'|}F_H\left(\frac{\xi r^\alpha}{P_{T_S}}\right)\right)^{M-1} f_R(r)\,\mathrm{d}r. \tag{3.25}$$

Corollary 3. *For the cooperation-based protocol, the n-th moment of the interference at an arbitrarily located PU-Rx due to an independently and uniformly distributed SU inside an*

arbitrarily shaped finite region is approximated by

$$\mu_I(n) \approx P_T^n \mathbb{E}_G\left\{G^n\right\} \mathbb{E}_R\left\{F_H\left(\frac{\xi R^\alpha}{P_{T_S}}\right)\left(\frac{\left|\mathcal{A}' - \pi r_c^2\right|}{|\mathcal{A}'|} + \frac{\pi r_c^2}{|\mathcal{A}'|} F_H\left(\frac{\xi R^\alpha}{P_{T_S}}\right)\right)^{M-1} R^{-n\alpha}\right\}. \tag{3.26}$$

Proof of Proposition 1 and Corollary 3: See Appendix B.3.

Remark 8. *To the best of our knowledge, it is not possible to express* (3.25) *and* (3.26) *in closed-form, even for the special cases of PU-Rx located at the center of a polygon or disk region. This is because* (3.25) *and* (3.26) *contain one term, related to the random variable R, which is raised to the power of* $M-1$ *(*$M \geq 2$*) inside the expectation. Nevertheless,* (3.25) *and* (3.26) *can easily be evaluated numerically. Also, if* $r_c = 0$*, the term raised to the power of* $M-1$ *becomes one and* (3.25) *and* (3.26) *reduce to* (3.22) *and* (3.23)*.*

Summarizing, for an arbitrarily located PU-Rx inside an arbitrarily shaped convex region and the different SU activity protocols, we can calculate (i) the MGF of the aggregate interference by substituting (3.17), (3.22) and (3.25) into (3.11), (ii) the n-th cumulant of the aggregate interference by substituting (3.18), (3.23) and (3.26) into (3.12), and (iii) the outage probability in the primary network by substituting (3.17), (3.22) and (3.25) into (3.16) and (3.15).

3.4 Average Number of Active Secondary Users

The aggregate interference at the PU-Rx and the resulting outage probability are metrics to evaluate the performance of the primary network, which was the common focus of most prior studies on cognitive networks, e.g., [38, 39, 62, 63]. Ideally, the performance of the secondary network should also be evaluated. Furthermore, this should be done subject to a quality-of-service constraint that the SINR of each active SU is maintained higher than a desired level. One way to do this analytically is to determine the SU throughput which can be defined as the expected spatial density of successful SU transmission and depends on (i) the number of active SUs over a certain region and (ii) whether each active SU is in outage or not, i.e., whether its SINR is above a certain threshold.

The exact SINR distribution of an active SU (and consequently the SU throughput) in an arbitrarily shaped underlay cognitive network is difficult to obtain because of two main reasons. *Firstly*, for an arbitrarily shaped region with a fixed number of nodes, the Binomial Point Process is non-stationary and an active SU's SINR is, therefore, location-dependent. Thus, the SINR of an active SU at a certain location (say origin) does not reflect the SINR of other active SUs. The difficulty in *analytically averaging* the active SU's SINR over all possible locations

in an arbitrarily shaped region poses a significant challenge for the derivation of analytical expression. *Secondly*, with the consideration of the different SU activity protocols, only the active SUs generate interference to other SUs and PU-Rx. This means that when accounting for the interference to a SU-Rx (which is the desired receiver for a certain SU), the distance between an interfering SU and PU-Rx is *correlated* to the distance between this interfering SU and the SU-Rx. This distance correlation poses a second significant challenge for analytical analysis.

In this work, in order to evaluate the performance of the secondary network in underlay cognitive networks, we study the average number of active SUs. The average number of active SUs is an analytically tractable performance metric, which can indirectly measure the SU throughput under certain conditions. For example, if the SINR threshold for SUs is not too high or each SU is sufficiently close to its desired receiver, it is possible that almost every active SU can transmit successfully. Under such conditions, the average number of active SUs plays the dominant role in determining the aggregate throughput of SUs[3].

The main analytical result in this section is presented in Theorem 3 below.

Theorem 3. *For any SU activity protocol with independently and uniformly distributed SUs inside an arbitrarily shaped finite region, the average number of active SUs is given by*

$$\overline{M}_{active} = M \times \mu_I(0), \tag{3.27}$$

where $\mu_I(0)$*, which is dependent on the SU activity protocol, is obtained using* (B.3) *and substituting* $n = 0$*.*

Proof: See Appendix B.4.

Remark 9. *Theorem 3 is valid for any SU activity protocol with i.u.d. node distribution and i.i.d. fading channels. For the protocols considered in this work, the value of* $\mu_I(0)$ *can be easily computed from* (3.18)*,* (3.23) *and* (3.26)*, respectively.*

Remark 10. *Intuitively, there is tradeoff between the primary network performance (i.e., in terms of the outage probability in the primary network) and the secondary network performance (i.e., in terms of the average number of active SUs). For example, increasing* r_f *in the guard zone protocol or decreasing the activation threshold* ξ *in threshold-based and cooperation-based protocols can reduce the outage probability. However, this would decrease the number of active secondary users, which means the licensed spectrum is not efficiently reused. In this context,* (3.15) *and* (3.27) *provide an analytical means for evaluating this tradeoff in the performance of both the primary and secondary networks. In the next section,*

[3]We have confirmed this through extensive simulations.

Table 3.1: Main System Parameter Values.

Parameter	Symbol	Value
Transmit powers	P_{T_S}, P_{T_0}, P_T	1
SINR threshold	γ_{th}	0 dB
Signal-to-noise ratio	γ_0	20 dB
Reference distance	r_0	5 m
Primary exclusion zone radius	ϵ	1
Path-loss exponent	α	2.5
Nakagami-m fading parameters	$m_0 = m_g = m_h$	3

we will use the primary-secondary performance tradeoff as a systematic way to compare the performance of the different SU activity protocols.

3.5 Numerical Results

In this section, we present numerical results to investigate and compare the performance of the SU activity protocols. In order to validate the numerical results, we also present simulation results which are generated using MATLAB and are averaged over 1 million simulation runs. For the simulation results, we use the following procedure to uniformly distribute the SUs inside an arbitrarily shaped region [136]: (a) Generate a bounding box which is generally the minimal rectangle that can entirely enclose the polygon shape, (b) Randomly and uniformly generate a point in this bounding box, (c) Check whether this point is inside the required polygon, (d) Repeat steps (b) and (c) until the required number of nodes are obtained. Unless specified otherwise, the values of the main system parameters shown in Table 3.1 are used. All the distance, side length and radius values are in meters (m).

3.5.1 Validation of Cooperation-based Protocol Analysis

First, we investigate the accuracy of the cooperation-based protocol analysis given in Section 3.3.3. Figure 3.2 plots the outage probability at the PU-Rx, P_{out}, versus the normalized radius of the cooperation range, $\frac{r_c}{\mathcal{R}/100}$, when the PU-Rx is located at the center and circumference, respectively, of a disk region with different radius and number of SU pair values $(\mathcal{R}, M)$ (i.e., $(150\text{ m}, 225)$, $(100\text{ m}, 100)$ and $(50\text{ m}, 25)$). The analytical result is plotted using Proposition 1, i.e., by substituting (3.25) into (3.16) and (3.15). The figure shows that the analytical results match closely with the simulation results when the cooperation range is relatively small compared to the size of the cognitive network region. For the disk case with the considered $(\mathcal{R}, M)$ pair values, the analytical result is accurate even when the radius of the cooperation region is as large as 7% of the radius of the disk region. This is in line with the

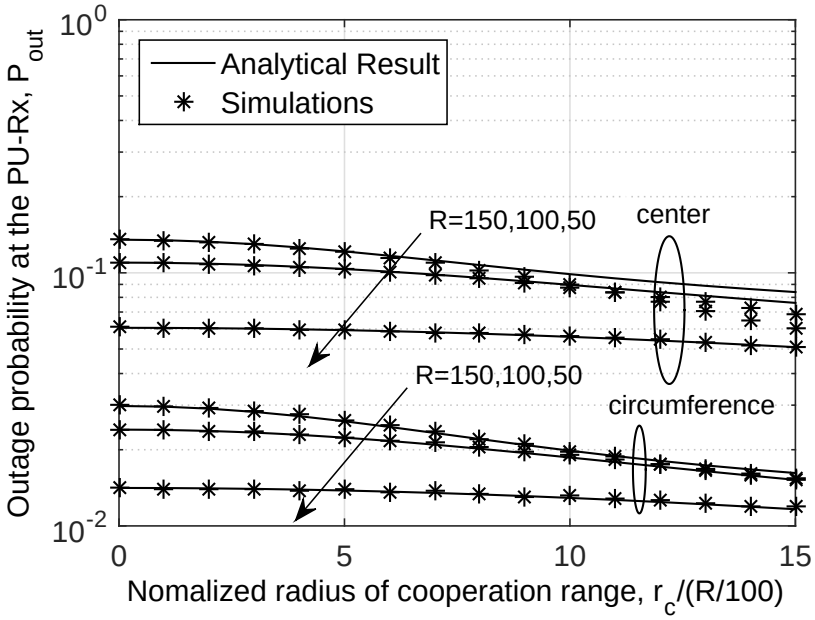

Figure 3.2: Outage probability at the PU-Rx, P_{out}, versus the normalized radius of the cooperation range, $\frac{r_c}{\mathcal{R}/100}$, for the cases that the PU-Rx is located at the center and circumference, respectively, of a disk region with different radius and number of SU pair values $(\mathcal{R}, M)$ (i.e., $(150\text{ m}, 225)$, $(100\text{ m}, 100)$ and $(50\text{ m}, 25)$).

assumption used for the analysis in Appendix B.3. We can also see from the figure that the outage probability decreases as r_c increases. This can be intuitively explained as follows. When the radius of the cooperation range r_c increases, the number of cooperating SUs increases and the opportunity of being active for each SU decreases. This reduces the aggregate interference and improves the primary network's outage performance. Also increasing the number of SUs increases the slope of the curves.

3.5.2 Moments of Aggregate Interference at the Primary Receiver

In this subsection, we investigate and compare the moments of the aggregate interference at the PU-Rx for the different SU activity protocols. We also illustrate the versatility of the proposed framework in being able to handle arbitrarily shaped cognitive network regions.

We consider an arbitrarily shaped cognitive network, as depicted in Figure 3.1, with side lengths $S_1 = S_2 = \sqrt{3}\mathcal{W}$, $S_3 = \sqrt{7-3\sqrt{2}-\sqrt{6}}\mathcal{W}$ and $S_4 = \mathcal{W}$ and interior angles $\theta_1 = \pi/2$, $\theta_2 = \pi/4$, $\theta_3 = \pi - \arcsin\left(\frac{\sqrt{6}-\sqrt{2}}{2S_3}\mathcal{W}\right)$ and $\theta_4 = \frac{\pi}{4} + \arcsin\left(\frac{\sqrt{6}-\sqrt{2}}{2S_3}\mathcal{W}\right)$. Without loss of generality, the origin is assumed to be at vertex V_1. The PU-Rx is located at coordinates $(\frac{\sqrt{3}\cos\frac{3\pi}{8}}{2\sin\frac{11\pi}{24}}\mathcal{W}, \frac{\sqrt{3}\sin\frac{3\pi}{8}}{2\sin\frac{11\pi}{24}}\mathcal{W})$, which corresponds to the intersection point of the two diagonals of the $L = 4$ sided arbitrarily shaped cognitive network. The radius of the guard zone and the cooperation range are set to $r_f = 30$ m and $r_c = 8$ m, respectively. The activation

Table 3.2: Validation of the 1st, 2nd and 3rd moment of the three SU activity protocols.

SU activity protocol	1st moment		Percentage error (%)
	analytical	simulation	
Guard zone	2.82E-3	2.82E-3	0.003
Threshold-based	2.10E-3	2.10E-3	0.002
Cooperation-based	1.83E-3	1.83E-3	0.063
SU activity protocol	2nd moment		Percentage error (%)
	analytical	simulation	
Guard zone	8.20E-6	8.20E-6	0.006
Threshold-based	4.61E-6	4.61E-6	0.006
Cooperation-based	3.47E-6	3.48E-6	0.29
SU activity protocol	3rd moment		Percentage error (%)
	analytical	simulation	
Guard zone	2.45E-8	2.45E-8	0.007
Threshold-based	1.06E-8	1.05E-8	0.068
Cooperation-based	6.88E-9	6.95E-9	1

threshold for both the threshold-based and the cooperation-based protocols is set to $\xi = 10^{-4}$ (linear scale).

Applying the algorithm in [88], the distance distribution function $f_R(r)$ can be expressed as

$$f_R(r) = \frac{1}{|\mathcal{A}'|} \begin{cases} 2\pi r, & \epsilon \le r < d_{S_3}; \\ 2\pi r - 2r\arccos\left(\frac{d_{S_3}}{r}\right), & d_{S_3} \le r < d_{S_4}; \\ 2\pi r - 2r\arccos\left(\frac{d_{S_3}}{r}\right) - 2r\arccos\left(\frac{d_{S_4}}{r}\right), & d_{S_4} \le r < d_{V_4}; \\ \frac{9}{4}\pi r - \theta_3 r - r\arccos\left(\frac{d_{S_3}}{r}\right) - r\arccos\left(\frac{d_{S_4}}{r}\right), & d_{V_4} \le r < d_{S_2}; \\ \frac{9}{4}\pi r - \theta_3 r - 2r\arccos\left(\frac{d_{S_2}}{r}\right) - r\arccos\left(\frac{d_{S_3}}{r}\right) - r\arccos\left(\frac{d_{S_4}}{r}\right), & d_{S_2} \le r < d_{V_3}; \\ \frac{5}{4}\pi r - r\arccos\left(\frac{d_{S_2}}{r}\right) - r\arccos\left(\frac{d_{S_4}}{r}\right), & d_{V_3} \le r < d_{S_1}; \\ \frac{5}{4}\pi r - 2r\arccos\left(\frac{d_{S_1}}{r}\right) - r\arccos\left(\frac{d_{S_2}}{r}\right) - r\arccos\left(\frac{d_{S_4}}{r}\right), & d_{S_1} \le r < d_{V_1}; \\ \frac{3}{4}\pi r - r\arccos\left(\frac{d_{S_1}}{r}\right) - r\arccos\left(\frac{d_{S_2}}{r}\right), & d_{V_1} \le r < d_{V_2}; \end{cases} \tag{3.28}$$

where d_{V_i} denotes the distance from PU-Rx to vertex V_i ($i = 1, 2, 3, 4$), d_{S_i} denotes the perpendicular distance from PU-Rx to side S_i and the area $|\mathcal{A}'| = \left(\frac{3}{2\sqrt{2}} + \frac{1}{2}\left(\sqrt{3} - \sqrt{\frac{3}{2}}\right)\right)\mathcal{W}^2 - \pi\epsilon^2$. Using the geometry, it can be easily shown that $d_{V_1} = \frac{\sqrt{3}}{2\sin\frac{11\pi}{24}}\mathcal{W}$, $d_{V_2} = \frac{\sqrt{3}\sin\frac{3\pi}{8}}{\sin\frac{11\pi}{24}}\mathcal{W}$, $d_{V_3} = \frac{\sqrt{6}\mathcal{W}}{2\sin\frac{3\pi}{8}} - d_{V_1}$, $d_{V_4} = 2\mathcal{W} - d_{V_2}$, $d_{S_1} = \frac{\sqrt{3}\sin\frac{3\pi}{8}}{2\sin\frac{11\pi}{24}}\mathcal{W}$, $d_{S_2} = \frac{\sin\frac{13\pi}{24}}{\sqrt{3}\mathcal{W}}d_{V_2}d_{V_3}$, $d_{S_3} = \frac{\sin\frac{11\pi}{24}}{S_3}d_{V_3}d_{V_4}$, and $d_{S_4} = \frac{\sqrt{3}\cos\frac{3\pi}{8}}{2\sin\frac{11\pi}{24}}\mathcal{W}$.

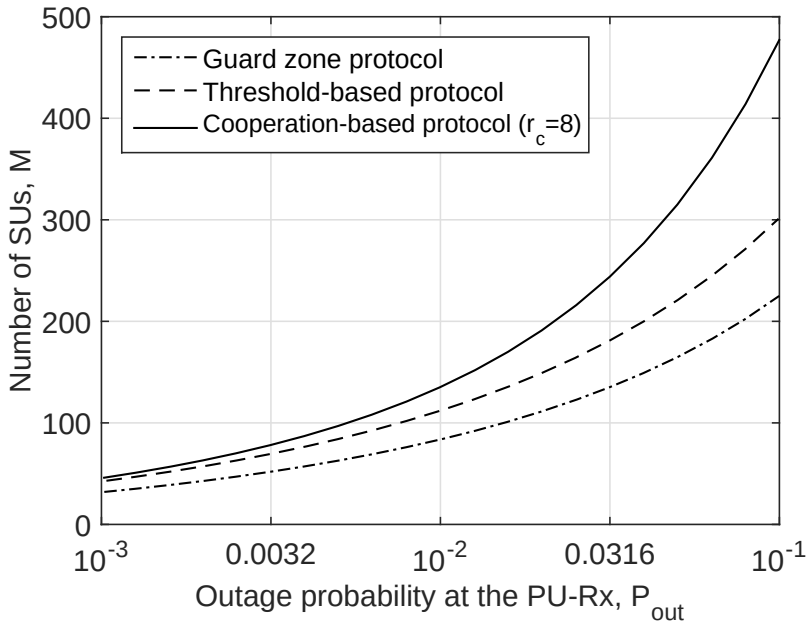

Figure 3.3: Number of SUs, M, versus the outage probability at the PU-Rx, P_{out}, for the scenario defined in Section 3.5.2 with $\mathcal{W} = 150$ m.

Substituting (3.28) in Corollaries 1, 2, 3, we can obtain the analytical n-th moment results. Table 3.2 shows the 1st, 2nd and 3rd moment of the aggregate interference for the three SU activity protocols with $\mathcal{W} = 150$ m. The simulation results are an excellent match with the analytical results, which confirms the accuracy of the results in Corollaries 1, 2, 3. We can see from Table 3.2 that for the considered case, the proposed cooperation-based protocol has the smallest values of the moments, i.e., it results in the smallest aggregate interference. The next best is the threshold-based protocol, followed by the guard zone protocol.

3.5.3 Outage Probability at the Primary Receiver

In this subsection, we investigate and compare the outage probability at the PU-Rx for the different SU activity protocols.

Figure 3.3 plots the number of SUs M versus the outage probability at the PU-Rx, P_{out}, for the different SU activity protocols and the arbitrarily shaped cognitive network region considered in Section 3.5.2 with $\mathcal{W} = 150$ m. The analytical results are plotted by substituting (3.28) in Theorems 1, 2, 1, and then substituting in (3.16) and (3.15). As illustrated in this figure, for the considered case, the cooperation-based performs the best while the guard zone protocol performs the worst. For example, for $M = 100$ SUs inside the arbitrarily shaped region, the cooperation-based protocol can achieve the best QoS of $P_{\text{out}} = 5.33 * 10^{-3}$ at the PU-Rx. However, the threshold-based protocol and guard zone protocol can only achieve

$P_{\text{out}} = 7.59 * 10^{-3}$ and $P_{\text{out}} = 1.54 * 10^{-2}$, respectively.

It must be noted that such an analysis has two main issues. Firstly, for a given shape of the network region and a given location of the PU-Rx, the outage at the PU-Rx strongly relies on the protocol system parameters (i.e., the guard zone range r_f for the guard zone protocol, activation threshold ξ for both of the threshold-based and cooperation-based protocols) and different values of the protocol system parameters can lead to a different performance ordering of the SU activity protocols. Secondly, it focuses on the performance in the primary network only. These aspects are addressed in the next Section 3.5.4.

3.5.4 Comparison of Secondary User Activity Protocols

In this section, we investigate and compare the SU activity protocols in terms of their effect on the primary network (i.e., the outage probability) and the secondary network (i.e., the average number of active SUs).

Figure 3.4 plots the average number of active SUs, $\overline{M}_{\text{active}}$, versus the outage probability at the PU-Rx, P_{out}, when the PU-Rx is located at the intersection point of the two diagonals inside the arbitrarily shaped finite region specified in Section 3.5.2 with $\mathcal{W} = 150$ m. The results are shown for different values of path-loss exponent $\alpha = 2, 3, 6$ (Figure 3.4(a)) and Nakagami-m fading $m = 1, 3, 5$ (Figure 3.4(b)), respectively. The following approach is adopted to work out these curves for the SU activity protocols:

1. For each PU-Rx's outage probability value, using (3.15), (3.16) and Theorems 1, 2, 1, we can find the value of r_f for guard zone protocol and ξ for threshold-based protocol and cooperation-based protocol, respectively;

2. We substitute the value r_f and ξ into (3.27) and Corollaries 1, 2, 3 to obtain the average number of active SUs for each protocol.

Figure 3.4 shows that for each protocol, the active number of SUs is higher if the fading is less severe (i.e., m has higher value) or if the path-loss exponent has a higher value. For the same outage probability, it is desirable to have a larger average number of active SUs. From Figure 3.4, we can see that the guard zone protocol supports the largest number of active SUs, followed by the cooperation-based protocol and the threshold-based protocol. For example, in order to achieve a QoS of $P_{\text{out}} = 0.01$ at the PU-Rx with $m = 3$ and $\alpha = 2.5$, only 192 SUs are active on average under the threshold-based protocol. However, the cooperation-based protocol and guard zone protocol can have 197 and 207 active SUs, respectively. This ordering stays the same for the different values of m and α.

This ordering can be intuitively explained as follows. The guard zone protocol supports the largest number of active SUs because it enables the SUs to determine their "average" impact on

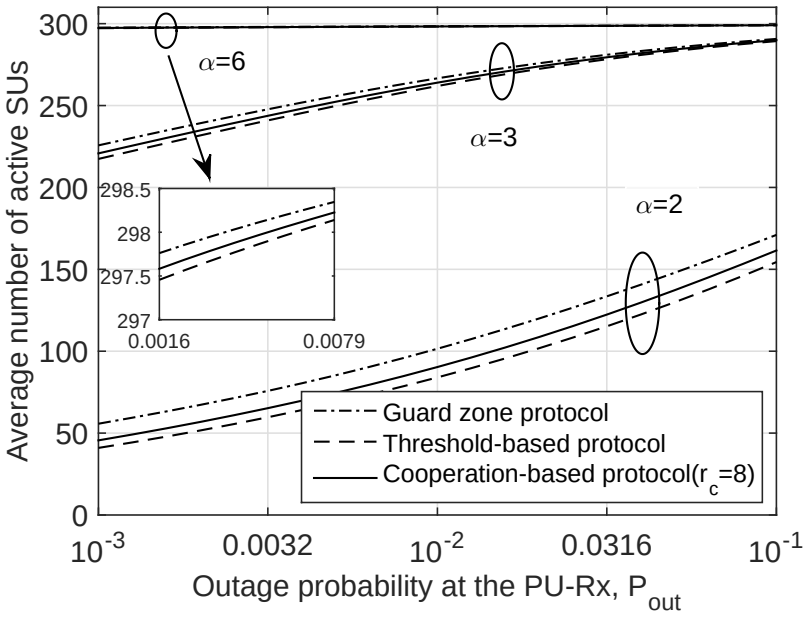

(a) Different path-loss exponent $\alpha = 2, 3, 6$.

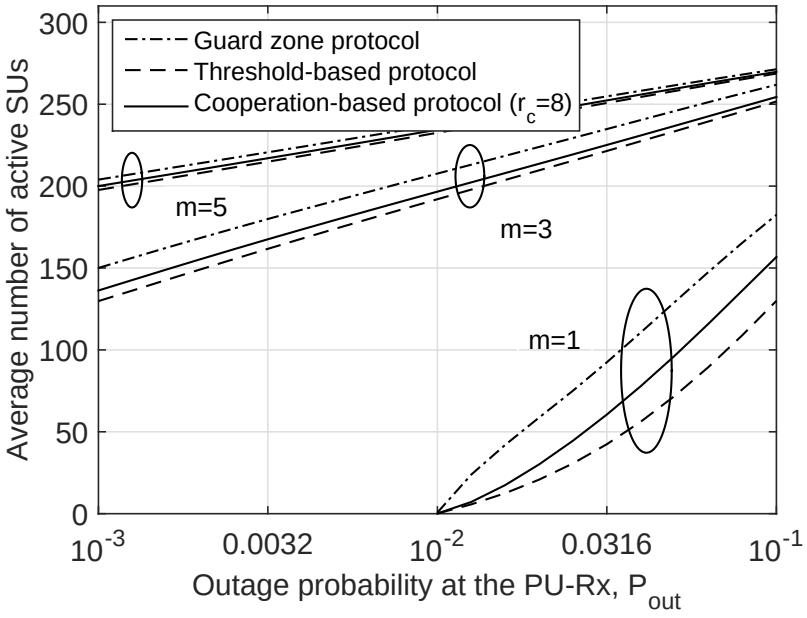

(b) Different Nakagami-m fading $m = 1, 3, 5$.

Figure 3.4: Average number of active SUs, $\overline{M}_{\text{active}}$, versus the outage probability at the PU-Rx, P_{out}, when the PU-Rx is located at the intersection point of two diagonals inside the arbitrarily shaped finite region specified in Section 3.5.2 with $\mathcal{W} = 150$ m.

the PU-Rx from long-term sensing signal monitoring. The outage probability is usually caused by the SUs that are close to the PU-Rx. By forming a proper guard zone region around the PU-Rx, the interference from the nearby SUs is avoided and on average more SUs are allowed to transmit. The threshold-based protocol supports the smallest number of active SUs due to the effect of uncorrelated fading between sensing and transmitting channels. For example, the fading on the sensing channel may be severe but the fading on the SU transmitting channel may be weak. Thus, the SU may receive a weak signal on the sensing channel and decide to transmit, which may generate severe interference for the PU-Rx. The cooperation-based protocol helps to minimize the effect of uncorrelated fading channels by utilizing the local information exchange among SUs. Therefore, the cooperation-based protocol allows a higher activation threshold while still meeting the same outage value. This results in the larger number of active SUs, compared to the threshold-based protocol. Although the guard zone protocol supports the largest number of active SUs, the implementation of this protocol is only possible in scenarios that allow a long-term sensing signal monitoring before SUs can transmit. On the other hand, the threshold-based and cooperation-based protocols only rely on the short-term signal monitoring. It must be noted that a more comprehensive comparison requires a rigorous study of the tradeoff between performance and implementation complexity in the scenario of interest, which is outside the scope of this work.

3.6 Summary

In this chapter, we considered an arbitrarily shaped underlay cognitive network, where SU activity protocols were employed to limit the interference generated by SUs. We presented a framework to study the statistics of interference generated by SUs, the outage probability at the primary user and the average number of active SUs, under different SU activity protocols. Our analytical results indicated that, in the short-term sensing signal monitoring scenario, our proposed cooperation-based protocol improves the network performance compared to the existing threshold-based protocol.

Chapter 4

Device-to-Device Communication Underlaying a Finite Cellular Network Region

Chapters 2 and 3 have focused on the arbitrarily shaped ad-hoc and underlay cognitive networks. For this chapter, we consider a cellular network underlaid with device-to-device communication, where users have the capability to directly talk to each others by bypassing the BS. In the underlay in-band D2D communication, the coexistence of D2D and cellular users causes severe inter-cell and intra-cell interference. The former can be effectively managed through inter-cell interference coordination. In this chapter, we examine the performance of intra-cell interference in a D2D communication enabled cellular network, where a D2D mode selection scheme is proposed to deal with intra-cell interference. Under this scheme, the potential D2D users are controlled by the BS to operate in D2D mode based on the average interference generated to the BS. For such a network, we present a tractable framework to study the outage probability experienced at both the BS and a typical D2D receiver, the average number of successful D2D transmissions and the spectrum reuse ratio, which is defined as the average fraction of D2D users that can successfully transmit. Note the latter two metrics are employed to investigate the performance of overall underlay D2D communication in a finite disk region. The analysis shows that the outage probability at the D2D receiver varies for different locations, which highlights the location-dependent performance. In addition, we observe that, without impairing the performance at the BS, the spectrum reuse ratio can have negligible decrease while the D2D users' average number of successful transmissions increases with increasing D2D node density, given that the path-loss exponent on the cellular link is slightly lower than that on the D2D link.

This chapter is organized as follows. Section 4.1 describes the network model and assumptions, including the mode selection scheme. Section 4.2 presents the analytical results for the outage probability at BS and a typical D2D receiver. Section 4.3 proposes and derives two

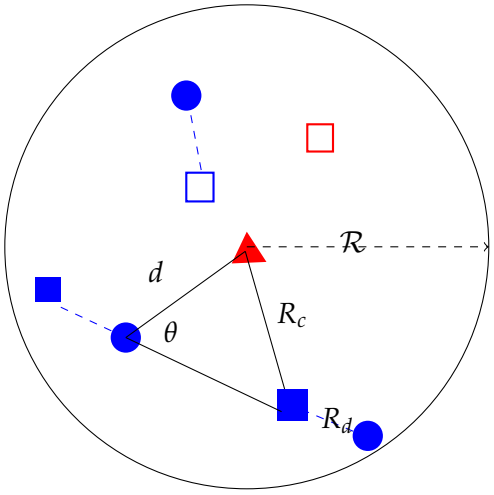

Figure 4.1: Illustration of the network model (▲ = BS, □ = CUE, ■ = DUE (p-DUE in D2D mode), □ = p-DUE in other transmission mode, • = DRx. Note that p-DUE and its corresponding DRx are connected by a dashed line).

metrics to assess the overall quality of underlay D2D communication in a finite region. Section 4.4 presents the numerical and simulation results, and uses the numerical results to obtain design guidelines. Finally, Section 4.5 summarize this chapter.

4.1 System Model

Consider a single cellular network that employs the orthogonal frequency-division multiple scheme with a center-located base station. The region of cell $\mathcal{A}$ is assumed to be a finite disk with radius $\mathcal{R}$ and area $|\mathcal{A}| = \pi\mathcal{R}^2$. We assume that the inter-cell interference is effectively managed with ICIC mechanism, based on resource scheduling. Hence, the inter-cell interference is not considered in this work. This assumption has been widely used in the literature, e.g., see [49, 91, 93, 94, 95, 96, 97, 98, 99]. We also restrict our analysis to one uplink channel because the other channels occupied by cellular users (CUEs) share similar interference statistics [41, 46, 47, 49, 50]. For analytical convenience, we assume that there is one uplink CUE, whose location follows a uniform distribution inside the entire cellular region (i.e., from 0 to $\mathcal{R}$). Let Z denote both the location of the CUE and the cellular user itself.

To improve the spectral efficiency of the frequency band occupied by the CUE, its uplink channel is also utilized for D2D communication. Note that D2D communication may also reuse downlink resources, but uplink is preferred in terms of interference in practical systems as it is less congested [89]. We further assume there are multiple potential D2D users (p-DUEs) that are randomly distributed in the entire cellular region $\mathcal{A}$. Note that the distributions of CUE and p-DUE are assumed to be independent. For each p-DUE, there is an intended D2D receiver

(DRx) which is uniformly distributed within this p-DUE's proximity (e.g., $\pi\mathcal{R}_D^2$)[1], hence, the distance distribution for the potential D2D link, R_d, is $f_{R_d}(r_d) = \frac{2r_d}{\mathcal{R}_D^2}$. Let X_k denote both the location of the k-th p-DUE and the user itself, and Y_k denote both the location of the k-th DRx and the receiver itself. For analytical convenience, we further assume that the location of p-DUE follows the Poisson Point Process, denoted as Φ, with constant density λ. Thus, based on the displacement property of PPP [71, eq. (2.9)], the location of DRxs also follows a PPP, denoted as Φ^{DRx}, with density λ^{DRx}.

We consider the path-loss plus block fading channel model. In this way, the received power at a receiver is $P_t G R^{-\alpha}$, where P_t is the transmit power of the transmitter, G denotes the fading power gain on the link that is assumed to be independently and identically distributed, R is the distance between the transmitter and receiver, and α is the path-loss exponent. Additionally, as we consider the uplink transmission, power control is necessary; we employ the full channel inversion for uplink power control [41, 46]. Hence, the transmit power for the CUE and the p-DUE using D2D link are $\rho_{\text{BS}} R_z^{\alpha_C}$ and $\rho_D R_d^{\alpha_D}$, respectively, where R_z is the distance between CUE and BS, ρ_{BS} and ρ_D are the minimum required power at BS and DRx (also known as the receiver sensitivity), and α_C and α_D are path-loss exponents on cellular link and D2D link, respectively.

We define the mode selection scheme as the selection between the underlay D2D mode (i.e., direct communication via the D2D link in underlay paradigm) or the other transmission mode. The other transmission mode can be the overlay D2D mode where the dedicated spectrum that is not occupied by cellular user is used, or the silent mode where no transmission happens [137, 138, 139]. In this chapter, as motivated by [111, 112], we consider that the mode selection for each p-DUE is determined by its average interference generated to the BS. For example, if the average interference $\rho_D R_{d_k}^{\alpha_D} R_{c_k}^{-\alpha_C}$ for the k-th p-DUE is larger than the threshold ξ, where R_{d_k} is the distance between this p-DUE and BS, then, this user is forced by the BS to operate in the other transmission mode. The focus of this chapter is on potential D2D users in underlay in-band D2D mode (referred to as DUEs which follow a certain point process Φ^{DUE}); the analysis of the other transmission mode is outside the scope of this work. Also we assume that the BS is fully in control of the D2D communication and D2D device discovery, which ensures that the considered mode selection scheme is feasible [139].

In the above set-up, intra-cell interference exists in the network because the considered spectrum band is shared between a CUE and DUEs. The aggregate interference received at the

[1] In reality, the intended DRx should also be confined in the network region $\mathcal{A}$ (i.e., a disk region with radius $\mathcal{R}$). However, for p-DUE nears cell-edge, this would mean that the DRx is no longer uniformly distributed in a disk region. For analytical tractability, we still assume that DRx is uniformly distributed in a disk region, regardless of the p-DUE's location, i.e., we assume that the DRx is confined in a disk region of radius $\mathcal{R} + \mathcal{R}_D$. The accuracy of this approximation will be validated in the results section.

BS and at a certain DRx Y_j can then be expressed as

$$I_{\text{agg}}^{\text{BS}} = \sum_{X_k \in \Phi} G_k^{\text{BS}} \rho_D R_{d_k}^{\alpha_D} R_{c_k}^{-\alpha_C} \mathbf{1}\left(\rho_D R_{d_k}^{\alpha_D} R_{c_k}^{-\alpha_C} < \xi\right), \tag{4.1a}$$

$$I_{\text{agg}}^{\text{DRx}}(X_j, Y_j) = \frac{G_z \rho_{\text{BS}} R_z^{\alpha_C}}{|Z - Y_j|^{\alpha_D}} + \sum_{X_k \in \Phi, k \neq j} \frac{G_k^{\text{DRx}} \rho_D R_{d_k}^{\alpha_D}}{|X_k - Y_j|^{\alpha_D}} \mathbf{1}\left(\rho_D R_{d_k}^{\alpha_D} R_{c_k}^{-\alpha_C} < \xi\right), \tag{4.1b}$$

respectively, where $\mathbf{1}(\cdot)$ is the indicator function, $|Z - Y_j|$ denote the Euclidean distance between CUE and j-th DRx, and $|X_k - Y_j|$ is the Euclidean distance between k-th DUE and j-th DRx. G_z, G_k^{BS} and G_k^{DRx} are the fading power gain on the interfering links, which are assumed to be i.i.d. Rayleigh fading. In the following, we refer I_{agg}^{κ} to the aggregate interference at a typical Rx κ for notation simplicity.

Considering an interference limited system, we can write the signal-to-interference ratio at a typical Rx κ as

$$\text{SIR}^{\kappa} = \frac{G_0 \rho}{I_{\text{agg}}^{\kappa}}, \tag{4.2}$$

where G_0 is the fading power gain on the reference link between the typical transmitter-receiver pair, which is assumed to experience Nakagami-m fading, ρ is the receiver sensitivity of the typical Rx (i.e., $\rho = \rho_{\text{BS}}$ when BS is the typical Rx and $\rho = \rho_D$ if DRx is the typical Rx)[2].

4.2 Outage Probability Analysis

To evaluate the network performance, we first consider and compute the outage probability experienced at a typical receiver.

4.2.1 Mathematical Framework

Our considered outage probability for a typical Rx at a given location is averaged over the fading power gain and the possible locations of all interfering users. Mathematically, the outage probability at a typical Rx can be written as

$$P_{\text{out}}^{\kappa}(\gamma_{\text{th}}) = \mathbb{E}_{I_{\text{agg}}^{\kappa}, G_0}\left\{\Pr\left(\frac{G_0 \rho}{I_{\text{agg}}^{\kappa}} < \gamma_{\text{th}}\right)\right\}, \tag{4.3}$$

where $\mathbb{E}_{I_{\text{agg}}^{\kappa}, G_0}\{\cdot\}$ is the expectation operator with respect to I_{agg}^{κ} and G_0.

[2] According to (4.1b), when the typical Rx is a DRx, the SIR relies on the location of DRx Y_j. Hence, the SIR at Y_j should be expressed as $\text{SIR}^{\text{DRx}}(X_j, Y_j)$. But in this work, we will sometimes ignore X_j and Y_j, and refer it simply as SIR^{DRx}. This notation is also adopted for the outage probability at Y_j, where the full notation would be $P_{\text{out}}^{\kappa}(\gamma_{\text{th}}, Y_j)$.

We leverage the reference link power gain-based framework [88] to work out the outage probability. For the case that the reference link suffers from Nakagami-m fading with integer m, the outage expression in (4.3) can be re-written as (see proof in Appendix C.1)

$$P_{\text{out}}^{\kappa}(\gamma_{\text{th}}) = 1 - \sum_{t=0}^{m-1} \frac{(-s)^t}{t!} \frac{\mathrm{d}^t}{\mathrm{d}s^t} \mathcal{M}_{I_{\text{agg}}^{\kappa}}(s) \Big|_{s=m\frac{\gamma_{\text{th}}}{\rho}}, \tag{4.4}$$

where $\mathcal{M}_{I_{\text{agg}}^{\kappa}}(s) = \mathbb{E}_{I_{\text{agg}}^{\kappa}}\left[\exp(-sI_{\text{agg}}^{\kappa})\right]$ is the moment generating function of I_{agg}^{κ}. Note that this fading model covers Rayleigh fading (i.e., by setting $m = 1$) and can also approximate Rician fading [88, 115]. Hence, it is adopted in this chapter.

As shown in (4.4), the computation of outage probability requires the MGF results for the aggregate interference at the typical Rx, which will be presented in the following.

4.2.2 MGF of the Aggregate Interference at the BS

The aggregate interference at the BS is generally in the form of $\sum_{X_k \in \Phi} I_k^{\text{BS}}$, where I_k^{BS} is the interference from the k-th p-DUE. Note that $I_k^{\text{BS}} = 0$ if k-th p-DUE is in the other transmission mode. Due to the i.u.d. property of p-DUEs and the i.i.d. property of the fading channels, the interference from a p-DUE is also i.i.d.. In the following, we drop the index k in R_{c_k}, R_{d_k}, G_k and I_k^{BS}. As such, the aggregate interference can be written as $\left(I^{\text{BS}}\right)^M$, where M is the number of p-DUEs following the Poisson distribution with density $\lambda(|\mathcal{A}|)$. Based on the MGF's definition (stated below (4.4)), the MGF of $I_{\text{agg}}^{\text{BS}}$ is given by

$$\mathcal{M}_{I_{\text{agg}}^{\text{BS}}}(s) = \mathbb{E}_M\left[\mathbb{E}_{I^{\text{BS}}}\left[\exp\left(-s\left(I^{\text{BS}}\right)^M\right)\Big| M\right]\right] = \exp\left(\lambda(|\mathcal{A}|)\left(\mathcal{M}_{I^{\text{BS}}}(s) - 1\right)\right), \tag{4.5}$$

where $\mathcal{M}_{I^{\text{BS}}}(s)$ denotes the MGF of the interference at the BS from a p-DUE, which is presented as follows.

Proposition 2. *For the underlay in-band D2D communication with the considered mode selection scheme in a disk-shaped cellular network region, following the system model in Section 4.1, the MGF of the interference from an i.u.d. p-DUE received at the BS can be expressed*

as

$$\mathcal{M}_{I^{\mathrm{BS}}}(s) = 1 + \frac{{}_2F_1\left[1, \frac{2}{\alpha_C}; 1+\frac{2}{\alpha_C}; \frac{-1}{s\xi}\right]}{\mathcal{R}_D^2 \mathcal{R}^2 \tilde{\mathcal{R}}_D^{-2-\frac{2\alpha_D}{\alpha_C}} (\xi/\rho_D)^{\frac{2}{\alpha_C}}} \frac{\alpha_C}{\alpha_D + \alpha_C} - \begin{cases} \left[\frac{\alpha_C\, {}_2F_1\left[1, \frac{2}{\alpha_C}; 1+\frac{2}{\alpha_C}; \frac{-\mathcal{R}^{\alpha_C}}{s\rho_D x^{\alpha_D}}\right] + \alpha_D\, {}_2F_1\left[1, \frac{-2}{\alpha_D}; 1-\frac{2}{\alpha_D}; \frac{-\mathcal{R}^{\alpha_C}}{s\rho_D x^{\alpha_D}}\right]}{x^{-2}\mathcal{R}_D^2(\alpha_C+\alpha_D)}\right]\Bigg|_0^{\tilde{\mathcal{R}}_D}, & \alpha_D \neq 2; \\ \frac{2\tilde{\mathcal{R}}_D{}^2 \mathrm{MeijerG}\left[\left\{\left\{0, \frac{\alpha_C-2}{\alpha_C}\right\}, \{2\}\right\}, \left\{\{0,1\}, \left\{\frac{-2}{\alpha_C}\right\}\right\}, \frac{\mathcal{R}^{\alpha_C}}{s\rho_D \tilde{\mathcal{R}}_D{}^2}\right]}{\mathcal{R}_D^2 \alpha_C}, & \alpha_D = 2; \end{cases} \tag{4.6}$$

where $\tilde{\mathcal{R}}_D \triangleq \min\left(\mathcal{R}_D, \mathcal{R}^{\frac{\alpha_C}{\alpha_D}} \left(\frac{\xi}{\rho_D}\right)^{\frac{1}{\alpha_D}}\right)$, ξ *is the mode selection threshold and* $G\left[\{\cdot\}, \cdot\right]$ *is the Meijer G-function.*

Proof: See Appendix C.2.

Note that the result in (4.6) is expressed in terms of the ordinary hypergeometric function and the Meijer G-function, which are readily available in standard mathematical packages such as Mathematica.

4.2.3 MGF of the Aggregate Interference at a Typical DRx

The point process of DUEs Φ^{DUE} is in fact an independent thinning process of the underlaying PPP Φ, which is also a PPP with a certain density [71]. Similarly, in terms of the location of underlay DRxs (i.e., whose corresponding p-DUE is in underlay D2D mode), it is also a PPP Φ_u^{DRx}, which is an independent thinning process of DRxs Φ^{DRx}.

For analytical convenience, we condition on an underlay DRx Y_0, which is located at a distance d away from the BS, and its corresponding DUE is denoted as X_0. Because of the isotropic network region and PPP's rotation-invariant property, the outage probability derived at Y_0 is the same for those underlay DRxs whose distance to BS is d. Then, according to the Slivnyak's theorem, we can have the MGF of the aggregate interference received at Y_0 as

$$\begin{aligned} \mathcal{M}_{I_{\mathrm{agg}}^{\mathrm{DRx}}}(s,d) &= \mathbb{E}_{I_C^{\mathrm{DRx}}}\left\{\exp\left(-sI_C^{\mathrm{DRx}}\right)\right\} \mathbb{E}_{\Phi\setminus X_0}\left\{\exp\left(-s\sum_{X_k\in\Phi\setminus X_0} I_k^{\mathrm{DRx}}(Y_0)\right)\right\} \\ &= \mathcal{M}_{I_C^{\mathrm{DRx}}}(s,d)\mathbb{E}_{\Phi}\left\{\exp\left(-s\sum_{X_k\in\Phi} I_k^{\mathrm{DRx}}(Y_0)\right)\right\} \\ &= \mathcal{M}_{I_C^{\mathrm{DRx}}}(s,d)\exp\left(\lambda(|\mathcal{A}|)\left(\mathcal{M}_{I^{\mathrm{DRx}}}(s,d)-1\right)\right), \end{aligned} \tag{4.7}$$

where I_C^{DRx} is the interference from CUE, $\mathcal{M}_{I_C^{\mathrm{DRx}}}(s,d)$ is the corresponding MGF, $I_k^{\mathrm{DRx}}(Y_0)$ is the interference from k-th p-DUE, and $\mathcal{M}_{I^{\mathrm{DRx}}}(s,d)$ is the MGF of the interference from a

p-DUE. The results for these two MGFs are presented as follows.

Proposition 3. *For the underlay in-band D2D communication with the considered mode selection scheme in a disk-shaped cellular network region, following the system model in Section 4.1, with the path-loss exponent $\alpha_C = \alpha_D = 2$ or 4, the MGF of the interference from an i.u.d. p-DUE received at a DRx, which is a distance d away from the BS can be given as*

$$\mathcal{M}_{I^{\mathrm{DRx}}}(s,d) = 1 - \begin{cases} \frac{s\rho_D \left[\Psi\left(x^2, s\rho_D, \mathcal{R}^2 - d^2, 4d^2 s\rho_D\right) - \Psi\left(x^2, s\rho_D + \frac{\rho_D}{\xi}, -d^2, 4d^2 s\rho_D\right)\right]\Big|_0^{\mathcal{R}_D}}{\mathcal{R}_D^2 \mathcal{R}^2}, & \alpha_C = \alpha_D = 2; \\ \frac{\mathrm{Im}\left\{\left[\Psi\left(x^2, -\mathbf{i}\sqrt{s\rho_D}, \mathcal{R}^2 - d^2, -4\mathbf{i}\sqrt{s\rho_D}d^2\right) - \Psi\left(x^2, \sqrt{\frac{\rho_D}{\xi}} - \mathbf{i}\sqrt{s\rho_D}, -d^2, -4\mathbf{i}\sqrt{s\rho_D}d^2\right)\right]\Big|_0^{\mathcal{R}_D}\right\}}{(\sqrt{s\rho_D})^{-1}\mathcal{R}_D^2\mathcal{R}^2}, & \alpha_C = \alpha_D = 4; \end{cases} \tag{4.8}$$

where $\Psi(x,\cdot,\cdot,\cdot)$ is given in (C.9)*. Note that for other α_C values, the semi-closed-form of $\mathcal{M}_{I^{\mathrm{DRx}}}(s,d)$ is available in* (C.8a) *($\alpha_D = 2$) and* (C.10a) *($\alpha_D = 4$).*

Proof: See Appendix C.3.

Corollary 4. *For the underlay in-band D2D communication with the considered mode selection scheme in a disk-shaped cellular network region, following the system model in Section 4.1, with the path-loss exponent $\alpha_C = \alpha_D = 2$ or 4, the MGF of the interference from an i.u.d. cellular user received at a DRx, which is distance d away from the BS, can be given as*

$$\mathcal{M}_{I_C^{\mathrm{DRx}}}(s,d) = 1 - \begin{cases} \frac{s\rho_{\mathrm{BS}} \left[\beta_2\left(x^2, (s\rho_{\mathrm{BS}}+1)^2, d^2(s\rho_{\mathrm{BS}}-1), 4d^4 s\rho_{\mathrm{BS}}\right)\right]\Big|_0^{\mathcal{R}}}{\mathcal{R}^2(s\rho_{\mathrm{BS}}+1)^3}, & \alpha_C = \alpha_D = 2; \\ \mathrm{Im}\left\{\frac{\sqrt{s\rho_{\mathrm{BS}}}\left[\beta_2\left(x^2, 1-\mathbf{i}\sqrt{s\rho_{\mathrm{BS}}}, -d^2\frac{1+\mathbf{i}\sqrt{s\rho_{\mathrm{BS}}}}{1-\mathbf{i}\sqrt{s\rho_{\mathrm{BS}}}}, \frac{-4\mathbf{i}\sqrt{s\rho_{\mathrm{BS}}}d^4}{(1-\mathbf{i}\sqrt{s\rho_{\mathrm{BS}}})^2}\right)\right]\Big|_0^{\mathcal{R}}}{\mathcal{R}^2(1-\mathbf{i}\sqrt{s\rho_{\mathrm{BS}}})^2}\right\}, & \alpha_C = \alpha_D = 4; \end{cases} \tag{4.9}$$

where $\beta_2(x,a,b,c) = \sqrt{(ax+b)^2+c} - b\ln\left(ax+b+\sqrt{(ax+b)^2+c}\right)$. For other α_C values, the $\mathcal{M}_{I_C^{\mathrm{DRx}}}(s,d)$ expression is given in (C.11b) *($\alpha_D = 2$) and* (C.12a) *($\alpha_D = 4$).*

Proof: See Appendix C.4.

Note that although (4.8) and (4.9) contain terms with the imaginary number, the MGF results are still real because of the $\mathrm{Im}\{\cdot\}$ function.

4.3 D2D Communication Performance Analysis

Generally, the outage probability reflects the performance at a typical user. In order to characterize the overall network performance, especially when the users are confined in a finite region, metrics other than the outage probability need to be considered. In this section, we consider two metrics: average number of successful D2D transmissions and spectrum reuse ratio. Their definitions and formulations are presented below.

4.3.1 Average Number of Successful D2D Transmissions

4.3.1.1 Mathematical Framework

In this chapter, the average number of successful D2D transmissions is defined as the average number of underlay D2D users that can transmit successfully over the network region $\mathcal{A}$. Therein, the successful transmission is defined as the event that the SIR at a DRx is greater than the threshold γ_{th}. For the considered scenario, we obtain the expression of the average number of success transmissions in the following.

Proposition 4. *For the underlay in-band D2D communication with the considered mode selection scheme in a disk-shaped cellular network region, following the system model in Section 4.1, the average number of successful D2D transmissions is*

$$\bar{M} = \int_0^{\mathcal{R}+\mathcal{R}_D} \left(1 - P_{out}^{\text{DRx}}(\gamma_{th}, d)\right) p_{\text{D2D}}(d) \lambda^{\text{DRx}}(d) 2\pi d \, \mathrm{d}d, \tag{4.10}$$

where $p_{\text{D2D}}(d)$ is the probability that p-DUE is in D2D mode given its corresponding DRx's distance to BS is d, $\lambda^{\text{DRx}}(d)$ is the node density of DRxs, and $P_{out}^{\text{DRx}}(\gamma_{th}, d)$ is outage probability at the corresponding DRx.
Proof: See Appendix C.5.

According to Proposition 4, the average number of successful D2D transmissions is determined by the outage probability experienced at the underlay DRxs, the density function of DRx, and the probability that the DRx is an underlay DRx. The outage probability has been derived in Section 4.2. In this section, we present the results for the remaining two factors, which will then allow the computation of average number of successful D2D transmissions using (4.10).

4.3.1.2 Density Function of DRxs

Before showing the exact density function, we define one lemma as follows.

Lemma 1. *For two disk regions with radii r_1 and r_2, respectively, which are separated by distance d, the area of their overlap region is given by [140]*

$$\psi(d, r_1, r_2) = r_1^2 \arccos\left(\frac{d^2 + r_1^2 - r_2^2}{2dr_1}\right) + r_2^2 \arccos\left(\frac{d^2 + r_2^2 - r_1^2}{2dr_2}\right) - \frac{\sqrt{2r_2^2(r_1^2 + d^2) - r_2^2 - (r_1^2 - d^2)^2}}{2}. \tag{4.11}$$

Using Lemma 1, we can express the node density of DRxs as shown in the following proposition.

Proposition 5. *For a disk-shaped network region with radius $\mathcal{R}$, assume that there are multiple p-DUEs that are randomly independently and uniformly distributed inside the region, and their location is modeled as a PPP with density λ. For each p-DUE, there is an intended DRx which is uniformly distributed inside the disk region formed around the p-DUE with radius $\mathcal{R}_D$. Then, the location of DRxs also follows a PPP, with the density*

$$\lambda^{\mathrm{DRx}}(d) = \begin{cases} \lambda, & 0 \le d < \mathcal{R} - \mathcal{R}_D; \\ \lambda \frac{\psi(d, \mathcal{R}, \mathcal{R}_D)}{\pi \mathcal{R}_D^2}, & \mathcal{R} - \mathcal{R}_D \le d \le \mathcal{R} + \mathcal{R}_D; \end{cases} \tag{4.12}$$

where $\psi(\cdot, \cdot, \cdot)$ is defined in Lemma 1.

Proof: See Appendix C.6.

The node density result in (4.12) can in fact be applied to a broader class of networks adopting the Poisson bi-polar network model [71, Definition 5.8]. To the best of our knowledge, this result for the node density of receivers for the bi-polar network model in a disk region has not been presented before in the literature.

4.3.1.3 Probability of being in D2D Mode

Proposition 6. *For the underlay in-band D2D communication with the considered mode selection scheme in a disk-shaped cellular network region, following the system model in Section 4.1, when the path-loss exponents for cellular link and D2D link are the same, the probability that a p-DUE is in underlay D2D mode given that its DRx's distance to BS is d, is given*

by

$$p_{\mathrm{D2D}}(d)=\begin{cases}\boldsymbol{I}(\xi>\rho_D)-\frac{\xi^{\frac{2}{\alpha}}d^2(-1)^{\boldsymbol{I}(\xi>\rho_D)+1}}{\left(\xi^{\frac{1}{\alpha}}-\rho_D^{\frac{1}{\alpha}}\right)^2\mathcal{R}_D^2}, & 0\le d<\mathcal{R}_{D1};\\ \boldsymbol{I}(\xi>\rho_D)-\frac{\psi\left(\mathrm{abs}\left(\frac{\xi^{\frac{2}{\alpha}}d}{\xi^{\frac{2}{\alpha}}-\rho_D^{\frac{2}{\alpha}}}\right),\mathcal{R}_D,\mathrm{abs}\left(\frac{\xi^{\frac{1}{\alpha}}\rho_D^{\frac{1}{\alpha}}d}{\xi^{\frac{2}{\alpha}}-\rho_D^{\frac{2}{\alpha}}}\right)\right)}{(-1)^{\boldsymbol{I}(\xi>\rho_D)+1}\pi\mathcal{R}_D^2}, & \mathcal{R}_{D1}\le d<\mathcal{R}_{D2};\\ 1, & d\ge\mathcal{R}_{D2};\end{cases}\tag{4.13}$$

where $\mathcal{R}_{D1}=\mathrm{abs}\left(1-\left(\frac{\rho_D}{\xi}\right)^{\frac{1}{\alpha}}\right)\mathcal{R}_D$, $\mathcal{R}_{D2}=\left(1+\left(\frac{\rho_D}{\xi}\right)^{\frac{1}{\alpha}}\right)\mathcal{R}_D$, ξ *is the mode selection threshold and* $\psi(\cdot,\cdot,\cdot)$ *is defined in* (4.11) *in Lemma 1. For* $\xi=\rho_D$, *we have* $p_{\mathrm{D2D}}(d)=1-\frac{\mathcal{R}_D^2\arccos\left(\frac{d}{2\mathcal{R}_D}\right)-\frac{d}{2}\sqrt{\mathcal{R}_D^2-\frac{d^2}{4}}}{\pi\mathcal{R}_D^2}$ *when* $d<2\mathcal{R}_D$, *while* $p_{\mathrm{D2D}}(d)=1$ *if* $d\ge2\mathcal{R}_D$.

Under the different path-loss exponent scenario, this probability can be approximated by

$$p_{\mathrm{D2D}}(d)\approx1+\sum_{n=1}^{N}(-1)^n\binom{N}{n}\frac{2d^{2\frac{\alpha_C}{\alpha_D}}(nN\xi)^{\frac{2}{\alpha_D}}\Gamma\left[-\frac{2}{\alpha_D},\frac{d^{\alpha_C}nN\xi}{(N!)^{1/N}\rho_D\mathcal{R}_D^{\alpha_D}}\right]}{\mathcal{R}_D^2\alpha_D\left((N!)^{1/N}\rho_D\right)^{\frac{2}{\alpha_D}}},\tag{4.14}$$

where N *is the parameter of a Gamma distribution which is used to formulate the approximation*[3].

Proof: See Appendix C.7.

4.3.2 Spectrum Reuse Ratio

Since we have employed the mode selection scheme, not all p-DUEs are in D2D mode. To evaluate the efficiency of our considered mode selection scheme, we propose a metric, namely the spectrum reuse ratio, which is defined as the average fraction of DUEs that can successfully transmit among all DUEs. For analytical tractability[4], spectrum reuse ratio is given by

$$\begin{aligned}\tau&=\frac{\text{average number of successful D2D transmissions}}{\text{average number of DUEs}}\\&=\frac{\bar{M}}{\bar{M}_{\mathrm{D2D}}},\end{aligned}\tag{4.15}$$

[3]By comparing with simulation results, we have verified that the average number of successful D2D transmissions obtained using this approximation is accurate when $N=6$.

[4]Note that a more accurate metric is the average of the ratio $\frac{\text{number of successful D2D transmissions}}{\text{number of DUEs}}$. However, such a metric is very difficult to obtain. Instead, we consider the metric in (4.15). It can be numerically verified that the values for these two metrics are very close to each other.

where $\bar{M}$ is given in (4.10), and $\bar{M}_{\mathrm{D2D}}$ is the average number of DUEs, which can be obtained as

$$\begin{aligned}\bar{M}_{\mathrm{D2D}} =& \mathbb{E}_{\Phi,R_d,R_c}\left\{\sum_{x\in\Phi}\mathbf{1}\left(\rho_D R_d^{\alpha_D} < \xi R_c^{\alpha_C}\right)\right\}\\ =& \int_0^{\mathcal{R}_D}\left(\int_0^{\mathcal{R}}\mathbf{1}\left(\rho_D r_d^{\alpha_D} < \xi r_c^{\alpha_C}\right)2\pi r_c\lambda\,\mathrm{d}r_c\right)f_{R_d}(r_d)\,\mathrm{d}r_d\\ =& \lambda\pi\int_0^{\tilde{\mathcal{R}}_D}\int_{r_d^{\frac{\alpha_D}{\alpha_C}}\left(\frac{\rho_D}{\xi}\right)^{\frac{1}{\alpha_C}}}^{\mathcal{R}} 2r_c f_{R_d}(r_d)\,\mathrm{d}r_c\,\mathrm{d}r_d\\ =& \lambda\pi\mathcal{R}^2\left(\frac{\tilde{\mathcal{R}}_D{}^2}{\mathcal{R}_D^2} - \frac{\alpha_C}{\alpha_C+\alpha_D}\frac{(\rho_D/\xi)^{\frac{2}{\alpha_C}}\tilde{\mathcal{R}}_D{}^{2\frac{\alpha_D}{\alpha_C}+2}}{\mathcal{R}^2\mathcal{R}_D^2}\right).\end{aligned} \tag{4.16}$$

4.3.3 Summary

Summarizing, for the underlay in-band D2D communication with the considered mode selection scheme in a disk-shaped cellular network region, following the system model in Section 4.1, we can calculate:

(i) outage probability at the BS by combining (4.5) and (4.6) in Proposition 2 and substituting into (4.4);

(ii) conditional outage probability at a DRx by combining (4.7), (4.8) in Proposition 3 and (4.9) in Corollary 4 and substituting into (4.4);

(iii) average number of successful D2D transmissions by substituting the conditional outage probability at a DRx, (4.12) in Proposition 5 and (4.13) (or (4.14)) in Proposition 6, into (4.10) in Proposition 4;

(iv) spectrum reuse ratio by finding the ratio of average number of successful D2D transmissions and $\bar{M}_{\mathrm{D2D}}$ in (4.16).

Note that the evaluation of the analytical results requires the differentiation and integration of the MGFs, which can be easily implemented using mathematical packages such as Mathematica.

4.4 Results

In this section, we present the numerical results to study the impact of the D2D system parameters (i.e., the p-DUE's node density λ and the receiver sensitivity of DRx ρ_D) on the outage

Table 4.1: Main System Parameter Values.

Parameter	Symbol	Value
p-DUE's node density	λ	$5 * 10^{-5}$ users/m^2
p-DUE's transmission range	$\mathcal{R}_D$	35 m
Receiver sensitivity for BS	ρ_{BS}	-80 dBm
Receiver sensitivity for DRx	ρ_D	-70 dBm
SIR threshold	γ_{th}	0 dB

probability, the average number of successful D2D transmissions and spectrum reuse ratio. To validate our derived results, the simulation results are generated using MATLAB, which are averaged over 10^6 simulation runs. Note that in the simulations, all DRxs are confined in the region $\mathcal{A}$. Unless specified otherwise, the values of the main system parameters shown in Table 4.1 are used. We assume a cell region radius of $\mathcal{R} = 500$ m. The vast majority of the D2D literature has considered either $\alpha_C = \alpha_D$ (i.e., [41, 44, 46, 47, 49, 97, 98, 99]) or α_C is slightly smaller than α_D (i.e., [50, 94, 141, 142, 143]). Hence we adopt the following path-loss exponent values when generating the main results: $\alpha_C = 3.5, 3.75, 4$ and $\alpha_D = 4$.[5]

4.4.1 Model Validation

In this subsection, we illustrate the accuracy of our derived results. Figure 4.2 plots the outage probability at BS and the average number of successful D2D transmissions versus the mode selection threshold ξ for different path-loss exponent sets, for $\mathcal{R}_D = 10$ m and $\mathcal{R}_D = 50$ m, respectively. The fading on the desired cellular link and the desired D2D link are assumed to be Rayleigh fading and Nakagami fading with $m = 3$, respectively. The analytical curves in Figure 4.2(a) are plotted using Proposition 2, i.e., substituting (4.5) and (4.6) into (4.4), while the curves in Figure 4.2(b) are plotted using the combination of Propositions 3, 4, 5, 6, and Corollary 4. From both figures, we can see that the analytical results match closely with the simulation results even when the mode selection threshold is small (i.e., probability of being DUE is small) or the radius of the p-DUE's transmission range is relatively large (i.e., 10% of the cell radius). This confirms the accuracy of our derived approximation results. In addition, as shown in Figure 4.2, both the outage probability at the BS and the average number of successful D2D transmissions increase as the mode selection threshold increases. This is because as mode selection threshold increases, more p-DUEs are allowed to be in underlay D2D mode which improves the average number of successful D2D transmissions. However, the increase in mode selection threshold degrades the outage performance at the BS since more interferers are involved.

[5]Consideration of multi-slope model [144] is outside the scope of this work.

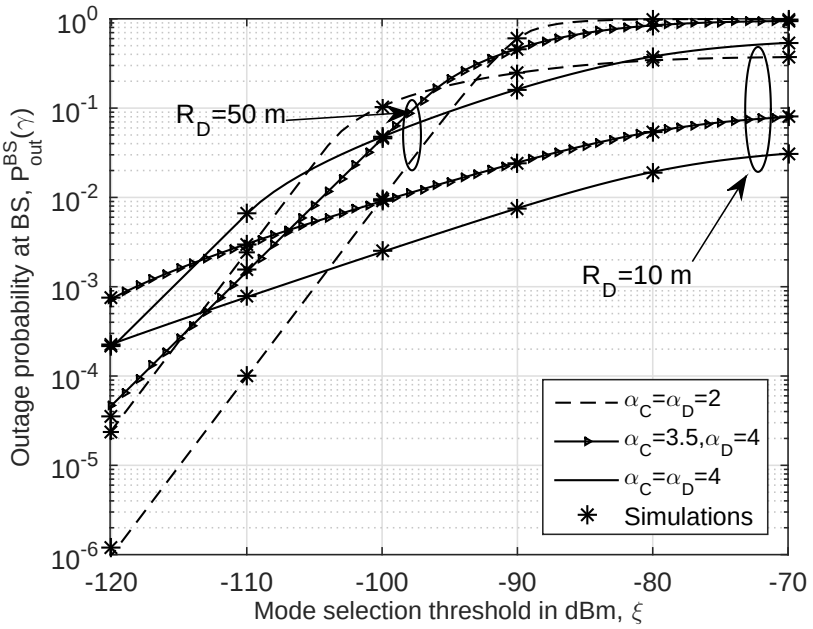

(a) Outage probability at the BS, $P_{\text{out}}^{\text{BS}}(\gamma_{\text{th}})$.

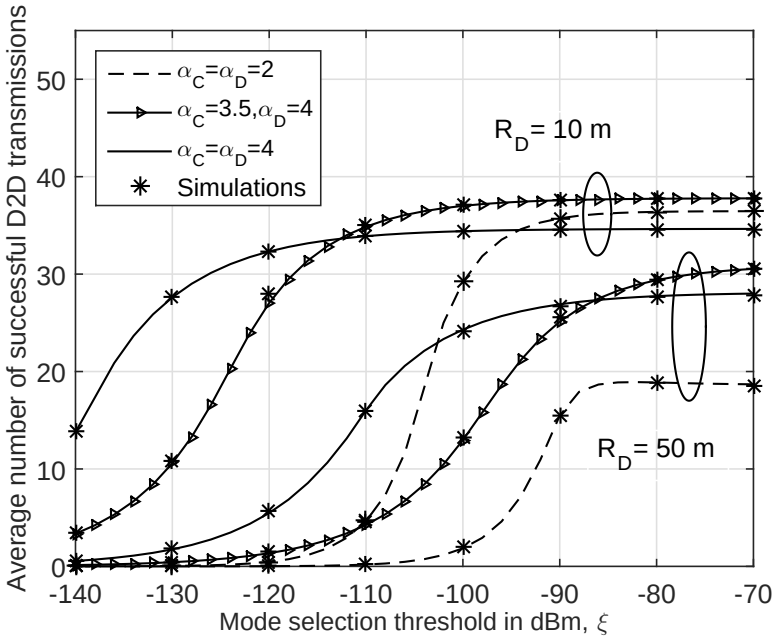

(b) Average number of successful D2D transmissions, $\bar{M}$.

Figure 4.2: Outage probability at the BS and average number of successful D2D transmissions versus the mode selection threshold ξ for $\mathcal{R}_D = 10$ m and $\mathcal{R}_D = 50$ m, respectively.

4.4.2 Outage Probability at DRx: Location-dependent Performance

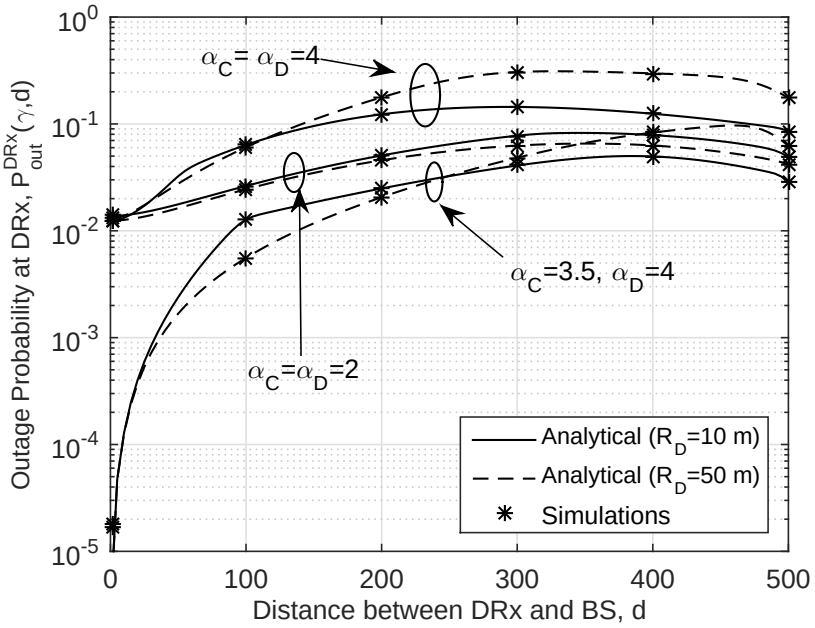

Figure 4.3: Outage probability at the DRx, $P_{\text{out}}^{\text{DRx}}(\gamma_{\text{th}}, d)$, versus the distance between the BS and the DRx, d, for $\mathcal{R}_D = 10$ m and $\mathcal{R}_D = 50$ m, respectively.

Figure 4.3 plots the outage probability at a typical DRx versus its distance to the BS with different path-loss exponent sets, for $\mathcal{R}_D = 10$ m and $\mathcal{R}_D = 50$ m, respectively. The simulation results are also presented and match well with the analytical results, which again validates our analytical results. As illustrated in Figure 4.3, the outage probability at the DRx varies greatly with the DRx location, which highlights the importance of characterizing the location-dependent performance. The general trends are that the outage probability firstly increases as the distance between DRx and BS increases and then decreases when the DRx is close to the cell-edge. These trends can be explained as follows. When the DRx is close to the BS, there are fewer number of p-DUEs that are in underlay D2D mode due to the mode selection scheme. Thus, interference is less and the outage probability is low. As the DRx gradually moves away from the BS, more interfering nodes are present and the outage probability increases. However, once the DRx is close to the cell-edge, the number of interfering DUEs decreases due to the boundary effect, and the outage probability decreases.

4.4.3 Effects of D2D User's Density

In this subsection, we investigate the effect of p-DUE's node density λ on the average number of successful D2D transmissions and spectrum reuse ratio (i.e., the average fraction of DUEs

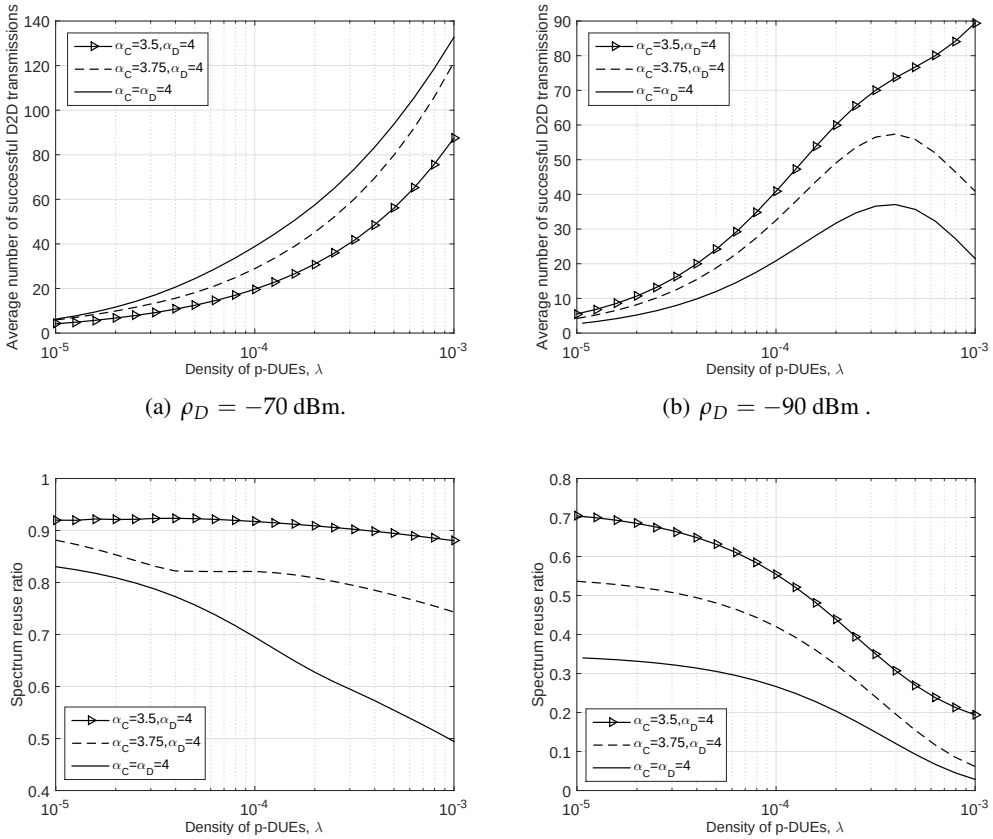

(a) $\rho_D = -70$ dBm. (b) $\rho_D = -90$ dBm .

(c) $\rho_D = -70$ dBm. (d) $\rho_D = -90$ dBm .

Figure 4.4: Average number of successful D2D transmissions $\bar{M}$ and spectrum reuse ratio τ versus the node density of p-DUEs λ, with different receiver sensitivity of DRx ρ_D, and QoS constraint $P_{\text{out}}^{\text{BS}}(\gamma_{\text{th}}) = 10^{-2}$.

that can successfully transmit among all DUEs). Since both the outage probability at the BS and the average number of successful D2D transmissions are increasing functions of the mode selection threshold ξ, as shown in Figure 4.2, we have adopted the following method to investigate the effects of D2D user's density:

- Given a QoS (i.e., the specified outage probability) at the BS, for each p-DUE's node density λ, using (4.4), (4.5) and (4.6), we can find the mode selection threshold ξ satisfying the QoS at the BS;

- Using the mode selection threshold ξ that satisfies the QoS at BS, the average number of successful D2D transmissions $\bar{M}$ can be calculated for each λ. This obtained $\bar{M}$ value can be regarded as the maximum average number of successful underlay D2D transmission achieved by the system. We can then work out the corresponding spectrum reuse ratio.

Figure 4.4 plots the average number of successful D2D transmissions and spectrum reuse ratio versus the node density of p-DUEs for QoS constraint at the BS $P_{\text{out}}^{\text{BS}}(\gamma_{\text{th}}) = 10^{-2}$ and different DRx's receiver sensitivity. We assume the fading on all the links to be Rayleigh fading. From Figures 4.4(a) and 4.4(c), we can see that the average number of successful D2D transmissions increases with increasing node density of p-DUE, however the spectrum reuse ratio decreases. This trend can be explained as follows. When the node density is higher, the probability of being in D2D mode is reduced to maintain the QoS at the BS. However, the overall node density is large which means that the number of DUEs is still large. Thus, the average number of successful D2D transmissions, which is mainly affected by the number of DUEs under this scenario, increases when the node density of p-DUEs increases. In contrast, when the number of interfering DUEs is large, the outage probability at the DRx is more severe. Thus, lesser number of DUEs are likely to transmit successfully, which leads to the decreasing trend of spectrum reuse ratio.

From Figure 4.4(b), we can see that when the receiver sensitivity of DRx is smaller than that of BS, increasing p-DUE's node density beyond a certain limit can degrade the average number of successful D2D transmissions, especially when α_C and α_D have very similar values. This is due to the fact that the average number of successful D2D transmissions is determined by the number of DUEs and the outage probability at DRx. When ρ_D is small, since there is a greater number of interfering DUEs nearby and the interference from CUE can be also severe when α_C and α_D have very similar values, the outage probability at DRx is high. Thus, $\bar{M}$ first increases and then decreases.

From Figure 4.4(c), we can see that if α_C is slightly smaller than α_D and ρ_D is greater than ρ_C, the decreasing trend for spectrum reuse ratio is almost negligible. In other words, the spectrum reuse ratio can be regarded as almost a constant and it does not degrade with increasing node density of p-DUE. Under such a case, increasing the p-DUE's node density is beneficial for underlay D2D communication.

4.4.4 Effects of D2D User's Receiver Sensitivity

In this subsection we examine the effect of DRx's receiver sensitivity ρ_D on the average number of successful D2D transmissions and spectrum reuse ratio, adopting the same approach as explained in Section 4.4.3. Figure 4.5 plots the average number of successful D2D transmissions and related spectrum reuse ratio versus the DRx's receiver sensitivity with QoS constraint at the BS $P_{\text{out}}^{\text{BS}}(\gamma_{\text{th}}) = 10^{-2}$, for different path-loss exponent sets and receiver sensitivity of BS ρ_{BS}.

From Figures 4.5(a) and 4.5(b), we can see that, in general, as the receiver sensitivity decreases the average number of successful D2D transmissions increases at first and then de-

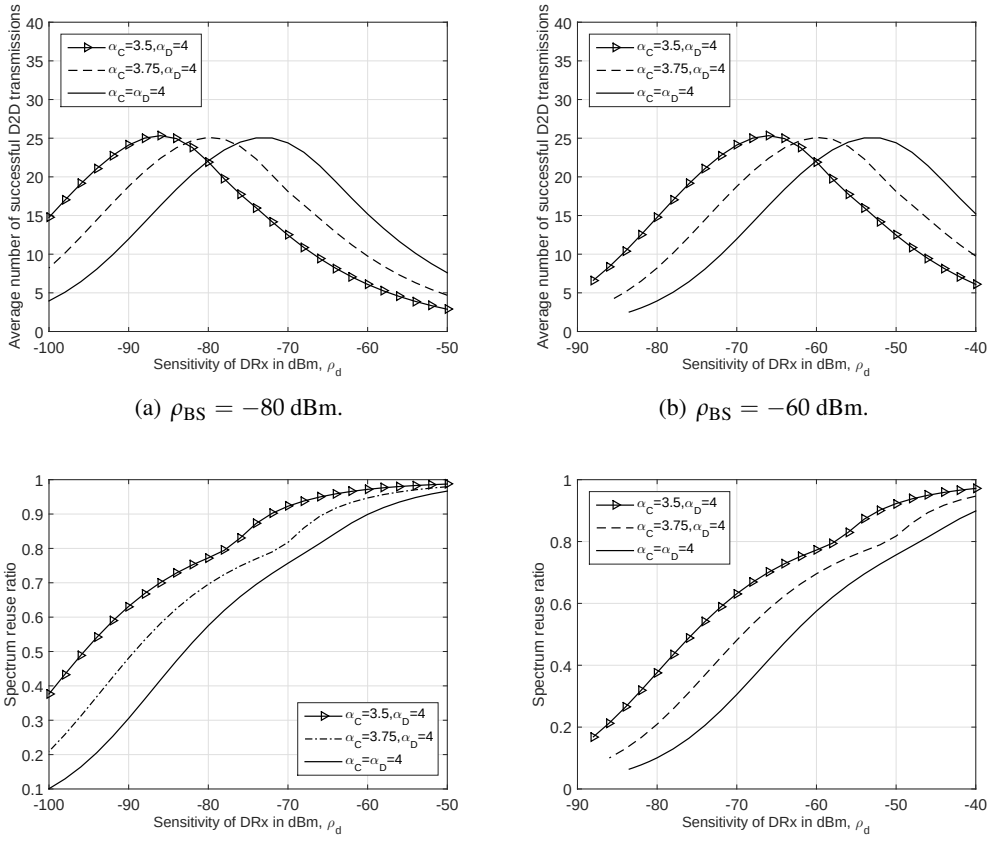

(a) $\rho_{\text{BS}} = -80$ dBm. (b) $\rho_{\text{BS}} = -60$ dBm.

(c) $\rho_{\text{BS}} = -80$ dBm. (d) $\rho_{\text{BS}} = -60$ dBm.

Figure 4.5: Average number of successful D2D transmissions $\bar{M}$ and spectrum reuse ratio τ versus the DRx's receiver sensitivity ρ_D, with different receiver sensitivity of BS ρ_{BS}, and QoS constraint $P_{\text{out}}^{\text{BS}}(\gamma_{\text{th}}) = 10^{-2}$.

creases. These trends can be explained as follows. The average number of successful D2D transmissions is impacted by both the number of DUEs and the outage probability at DRxs. When ρ_D is small, more p-DUEs are operating in D2D mode because their transmit power is small, so less interference is generated to the BS. Similarly, for the outage probability at DRx, although the total number of DUEs is large, the interference from surrounding DUEs is not severe due to the small receiver sensitivity. If we ignore the interference from CUE, the number of DUEs governs the network performance and the average number of successful D2D transmissions increases as the receiver sensitivity decreases. However, we cannot ignore the interference from CUE, especially when the value of α_C is large (i.e., close to the value of α_D). Under such a scenario, the transmit power for CUE is large. Moreover, due to the smaller receiver sensitivity at DRxs, DRxs are more likely to be in outage. Consequently, the interplay of the number of DUEs and the outage probability at the DRx causes the average number of successful D2D transmissions to first increase and then decrease as the receiver sensitivity decreases.

Figures 4.5(a) and 4.5(b) also show that for different path-loss exponent sets (α_C and α_D), the maximum value of the average number of successful D2D transmissions occurs at different receiver sensitivity values. For example, if $\alpha_C = \alpha_D$, $\bar{M}$ reaches its maximum value when the value of ρ_D is greater than ρ_C. However, if α_C is smaller than α_D, then a smaller receiver sensitivity of DRx results in the maximum $\bar{M}$. That is to say, as the value of α_C decreases, the required receiver sensitivity of DRx to achieve the maximum average number of successful D2D transmissions becomes smaller. Note that when ρ_C is far greater than ρ_D, although all p-DUEs are in D2D mode, the outage probability at the BS will still be lower than 10^{-2}. Hence, $\bar{M}$ cannot be computed and the curves are incomplete in Figures 4.5(b) and 4.5(d) for certain cases.

Figures 4.5(c) and 4.5(d) show that the spectrum reuse ratio generally decreases as the DRx's receiver sensitivity decreases. Additionally, when the path-loss exponent on the cellular link is slightly lower than the path-loss exponent on the D2D link, then the decreasing amount in the spectrum reuse ratio is less for the different cases considered.

4.5 Summary

In this chapter, we studied the performance of the intra-cell interference inside a disk-shaped cellular network underlaid with device-to-device communication, by incorporating the mode selection scheme to control the interference from D2D users. We first derived the outage probability experienced at both the BS and D2D receiver. To highlight the overall performance of underlay D2D communication in a finite region, we then proposed and calculated the average number of successful D2D transmissions and spectrum reuse ratio. Our analytical

results showed that, once the path-loss exponent on the cellular link is slightly lower than that on the D2D link, increasing the potential D2D users' density can benefit the underlay D2D communication without degrading the performance at the BS.

Chapter 5

Outage Probability of Ad-Hoc Networks with Wireless Information and Power Transfer

In Chapters 2, 3 and 4, we have investigated the performance for the networks with smart devices (i.e., ad-hoc networks, cognitive networks and D2D networks), which are the promising candidates for 5G. In this chapter, we analyze a network system that is beyond 5G, namely the simultaneous wireless information and power transfer system. We consider the simultaneous wireless information and power transfer in ad-hoc networks, where each transmitter is wirelessly powered by power beacons and uses the aggregate received power from PBs to transmit to its desired receiver. By considering that the RF harvested energy can have a large dynamic range, the practical aspect of power receiver activation threshold is incorporated into the system. For such a network, we derive the total outage probability at a typical Rx to examine the overall network performance, which is the combination of the power outage probability and channel outage probability. Note that the former term is defined as the probability that the aggregate power from PBs received at transmitter is lower than the power receiver activation threshold such that this Tx cannot transmit, while the latter term incorporates maximum transmit power at Tx and interference at Rx. For the special case of the path-loss exponent being 4, we derive accurate expressions for the power, channel and total outage probability. Our analytical results suggest that, in order to improve the total outage probability, it is necessary to increase either the power beacon's density or the power beacon's transmit power. In addition, when the Tx's node density is low, decreasing the power activation threshold is beneficial for the overall network performance.

This chapter is organized as follows. Section 5.1 presents the system model and the assumptions. Section 5.2 formulates the general expression of total outage probability, which includes both power outage probability and channel outage probability. Numerical results and the summary of this chapter are given in Sections 5.3 and 5.4, respectively.

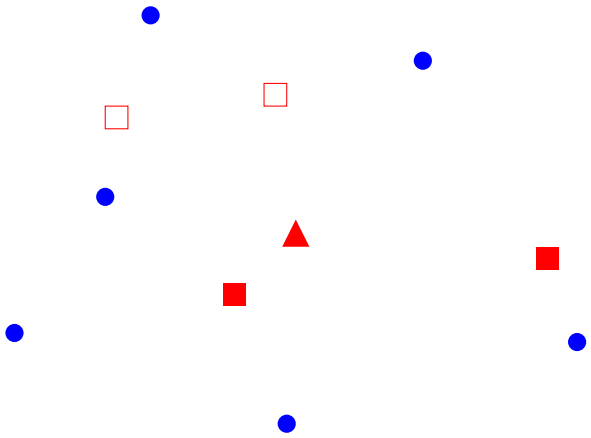

Figure 5.1: Illustration of the network model (● = power beacon, ■ = active transmitter, □ = inactive transmitter, ▲ = reference receiver).

5.1 System Model

We consider a two-dimensional wireless ad-hoc network with Tx and Rx pairs, as shown in Figure 5.1. The location of Txs is assumed to follow a homogeneous PPP, denoted as Φ_{Tx}, with node density λ_{Tx}. Each Tx has a desired Rx located at a distance r_0 from the corresponding Tx in a random direction. Note that we do not consider the relative motion between Tx and Rx. The PBs are randomly deployed and are modeled as a homogeneous PPP, denoted as Φ_{PB}, with node density λ_{PB}. We assume Φ_{Tx} and Φ_{PB} are independent. The PB's transmit power is P_{PB}. Let X_i denote both the random location as well as the i-th Tx itself, Y_i denote both the location and the corresponding i-th Rx and Z_i denote both the location and the i-th PB itself.

The Txs are wirelessly powered by the PBs. We make the following assumptions regarding the power transfer and information transmission:

- The PT from PBs and IT from Txs are sufficiently separated in frequency. Further, the PT and IT are isotropic such that each Tx/Rx can receive the PB/Tx signals, respectively, from all directions.

- Time is divided into slots and Txs employ the harvest-then-transmit architecture for IT and PT [145], as illustrated in Figure 5.2. Thus, in each time slot (T), PT occurs in the first τT seconds and IT in the remaining $(1-\tau)T$ seconds.

- In order to activate the energy harvesting circuit at any Rx, the aggregate received power from all the PBs must be greater than a power receiver activation threshold γ_{PT}[1].

- Each Tx has a maximum transmit power $P_{\max}$ due to the power amplifier rating.

[1] γ_{PT} is typically in the range -30 dBm to -10 dBm [102].

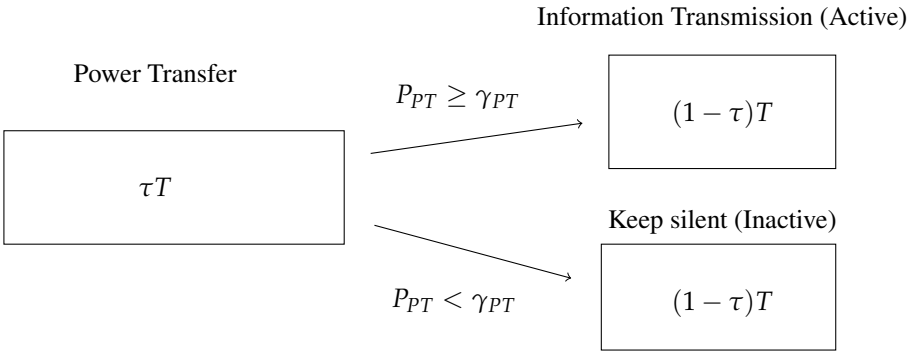

Figure 5.2: Illustration of the harvest-then-transmit architecture.

- $P_{\max}$ is sufficiently large such that the probability that the aggregate received power from all the PBs exceeds $P_{\max}$ is negligible. Hence, all the amount of received power during PT is used for IT, i.e., no energy storage involved.

We assume that all the channel links are modeled as i.i.d. Rayleigh block-fading channels[2]. Thus, in general the received power at any Tx (from a PB) or Rx (from a Tx) can be expressed as $P_t h r^{-\alpha}$, where r is the propagation distance, α is the path-loss exponent, h denotes the power gain due to fading which follows the exponential distribution with unit mean [71] and P_t denotes the transmit power. Note that for PB, $P_t = P_{\text{PB}}$ and for Tx, P_t will be be defined later in (5). In this work, we are interested in the outage probability at a typical Rx. This is formulated in the next section.

5.2 Outage Probability Formulation and Analysis

In the considered setup, an outage can occur at a typical Rx due to either of the following two conditions: (i) due to the random network topology and the fading channels, the received power at a Tx is a random variable. If the aggregate received power from all the PBs is below γ_{PT}, the Tx is inactive. Thus no IT can occur and the Rx is in *power outage*, and (ii) if a Tx is active (i.e., not in power outage), the Rx may still be in *channel outage* if the Rx SINR is below a certain threshold. This can occur because both the Tx transmit power, which depends on the random received power from PBs, and the interference received by Rx are random variables. Thus, the total outage can be formulated as

$$\mathcal{P}_{\text{out}} = \mathcal{P}^{\text{P}}_{\text{out}} + (1 - \mathcal{P}^{\text{P}}_{\text{out}})\mathcal{P}^{\text{C}}_{\text{out}}, \tag{5.1}$$

where $\mathcal{P}^{\text{P}}_{\text{out}}$ denotes the power outage probability and $\mathcal{P}^{\text{C}}_{\text{out}}$ denotes the channel outage probability. Note that both $\mathcal{P}^{\text{P}}_{\text{out}}$ and $\mathcal{P}^{\text{C}}_{\text{out}}$ need to be averaged with respect to the spatial node

[2]We do not consider shadowing but it can be included using the composite fading model in [120].

distributions and the fading distribution. In order to determine the outage probabilities, we add a reference receiver Y_0 at the origin and its associated transmitter X_0 at a distance d in a random direction. By Slivnyak's theorem, adding a point in a PPP does not change the distribution of the rest of the process [71]. In the following subsections, we derive expressions for these outage probabilities.

5.2.1 Power Outage Probability

The instantaneous aggregate received power from PBs at a typical Tx, X_0, is given by

$$P_{\mathrm{PT}_i} = \sum_{Z \in \Phi_{\mathrm{PB}}} P_{\mathrm{PB}} H_Z R_Z^{-\alpha}, \tag{5.2}$$

where H_Z is the fading power gain on the PT link and $R_Z = |Z_i - X_0|$ denotes the distance between a PB and X_0. Due to the stationary property of PPP [71], the distribution of the received power is identical for all Txs. Thus, we drop the index i in (5.2).

The power outage probability is the probability that the aggregate received power P_{PT} at a typical Tx is lower than the power circuit activation threshold, γ_{PT}. It is given by

$$\mathcal{P}_{\mathrm{out}}^{\mathrm{P}} = \Pr\left(P_{\mathrm{PT}} < \gamma_{\mathrm{PT}}\right) = F_{P_{\mathrm{PT}}}(\gamma_{\mathrm{PT}}), \tag{5.3}$$

where $F_{P_{\mathrm{PT}}}(\cdot)$ denotes the CDF of the received power.

Given the form of (5.2), which is similar to well known existing models of traditional ad-hoc networks [71], a closed-form expression for $F_{P_{\mathrm{PT}}}(\cdot)$ exists for path-loss exponent $\alpha = 4$ only. In the following, we consider the special case of $\alpha = 4$ to determine the power, channel and total outage probability. However, this does not diminish the contribution of this chapter since the proposed formulation in (5.18) is valid for any path-loss exponent.[3]

Proposition 7. *For the considered SWIPT system model as described in Section 5.1, the CDF of the aggregate received power P_{PT} for $\alpha = 4$ is given by*

$$F_{P_{PT}}(p_{PT}) = 1 - \mathrm{erf}\left(\pi^2 \lambda_{PB} \frac{\sqrt{P_{PB}}}{4\sqrt{p_{PT}}}\right). \tag{5.4}$$

[3] Our framework can also be easily modified to the scenario where each Tx harvests energy from its nearest PB only, in which case $F_{P_{\mathrm{PT}}}(\cdot)$ can be obtained using stochastic geometry for any α. However, this is outside scope of this work.

Proof. When $\alpha = 4$, the MGF of the aggregate received power P_{PT} is

$$\begin{aligned}\mathcal{M}_{P_{\mathrm{PT}}} =& \mathbb{E}_{P_{\mathrm{PT}}}\left\{\exp\left(-sP_{\mathrm{PT}}\right)\right\}\\ =& \mathbb{E}_{\Phi_{\mathrm{PB}},H_Z}\left\{\exp\left(-s\sum_{Z\in\Phi_{\mathrm{PB}}} P_{\mathrm{PB}}H_Z R_Z^{-4}\right)\right\}\\ =& \exp\left(-\int_0^{\infty}\mathbb{E}_{H_Z}\left\{1-\exp\left(-sP_{\mathrm{PB}}H_Z r_Z^{-4}\right)\right\}2\pi\lambda_{\mathrm{PB}}r_Z\,\mathrm{d}r_Z\right)\\ =& \exp\left(-\lambda_{\mathrm{PB}}\pi P_{\mathrm{PB}}^{\frac{1}{2}}\mathbb{E}_{H_Z}\left\{H_Z^{\frac{1}{2}}\right\}\Gamma\left[\frac{1}{2}\right]s^{\frac{1}{2}}\right),\end{aligned} \tag{5.5}$$

where the third step comes from the Campbell's theorem [71]. Notice that for the Lévy distribution with dispersion coefficient ζ, we have its MGF displayed as $\exp\left(-\sqrt{2\zeta}s^{\frac{1}{2}}\right)$ [71]. By comparing it with the MGF of P_{PT} given in (5.5), we can see that P_{PT} follows the Lévy distribution with dispersion coefficient $\zeta = \frac{1}{2}\left(\lambda_{\mathrm{PB}}\pi P_{\mathrm{PB}}^{\frac{1}{2}}\mathbb{E}_{H_Z}\left\{H_Z^{\frac{1}{2}}\right\}\Gamma[\frac{1}{2}]\right)^2$. When the PT link experiences Rayleigh fading (i.e., H_Z follows the exponential distribution), $\mathbb{E}_{H_Z}\left\{H_Z^{\frac{1}{2}}\right\} = \Gamma\left[\frac{3}{2}\right]$. Also $\Gamma\left[\frac{3}{2}\right]\Gamma\left[\frac{1}{2}\right] = \frac{\pi}{2}$. Hence, we arrive the result in (5.4). □

Substituting (5.4) into (5.3), we have the power outage probability $\mathcal{P}_{\mathrm{out}}^{\mathrm{P}}$ as

$$\mathcal{P}_{\mathrm{out}}^{\mathrm{P}} = 1 - \mathrm{erf}\left(\pi^2\lambda_{\mathrm{PB}}\frac{\sqrt{P_{\mathrm{PB}}}}{4\sqrt{\gamma_{\mathrm{PT}}}}\right). \tag{5.6}$$

5.2.2 Channel Outage Probability

According to our system model, the instantaneous transmit power for each *active* Tx can be written as

$$P_{\mathrm{Tx}} = \begin{cases}\mu P_{\mathrm{PT}}, & \mu^{-1}P_{\max} > P_{\mathrm{PT}} \geq \gamma_{\mathrm{PT}};\\ P_{\max}, & P_{\mathrm{PT}} \geq \mu^{-1}P_{\max};\end{cases} \tag{5.7}$$

where $\mu = \eta\frac{\tau}{1-\tau}$ and η is a factor representing the power conversion efficiency. Note that the first condition in (5.7) is due to the fact that the received power at an active Tx must be greater than γ_{PT}. The second condition in (5.7) is due to the maximum transmit power of active Txs. The distribution function of P_{Tx} is summairzed in Corollary 5.

Corollary 5. *For the considered SWIPT system model as described in Section 5.1, the PDF of*

the transmit power P_{Tx} for an active Tx for $\alpha = 4$ is given by

$$f_{P_{Tx}}(p_{Tx}) = \begin{cases} \frac{\pi^{1.5}\lambda_{PB}\sqrt{P_{PB}\mu}}{4p_{Tx}^{1.5}(1-\mathcal{P}_{out}^{P})} \exp\left(-\frac{\pi^4\lambda_{PB}^2 P_{PB}\mu}{16p_{Tx}}\right), & P_{max} > p_{Tx} \geq \mu\gamma_{PT}; \\ \frac{1-F_{P_{PT}}(\mu^{-1}P_{max})}{1-\mathcal{P}_{out}^{P}}\delta(p_{Tx}-P_{max}), & p_{Tx} \geq P_{max}; \end{cases} \tag{5.8}$$

where $\delta(\cdot)$ is the Dirac function [71].

Proof. In order to find the distribution of Tx's transmit power, we need to first obtain the distribution of the harvested energy. Taking the derivative of (5.4) with respect to P_{PT}, the distribution function of P_{PT} is given by

$$f_{P_{\mathrm{PT}}}(p_{\mathrm{PT}}) = \frac{\pi^{1.5}\lambda_{\mathrm{PB}}\sqrt{P_{\mathrm{PB}}}}{4p_{\mathrm{PT}}^{1.5}} \exp\left(-\frac{\pi^4\lambda_{\mathrm{PB}}^2 P_{\mathrm{PB}}}{16p_{\mathrm{PT}}}\right). \tag{5.9}$$

Without considering the conditions shown in (5.7), where the value of P_{Tx} has to lie in between $\mu\gamma_{\mathrm{PT}}$ and $P_{\max}$, P_{Tx} is directly related to P_{PT} by $P_{\mathrm{Tx}} = \mu P_{\mathrm{PT}}$. Using the variable transformation, the (unconditional) distribution of P_{Tx} is given by

$$f_{P_{\mathrm{Tx}}}(p_{\mathrm{Tx}}) = \frac{\pi^{1.5}\lambda_{\mathrm{PB}}\sqrt{P_{\mathrm{PB}}\mu}}{4p_{\mathrm{Tx}}^{1.5}} \exp\left(-\frac{\pi^4\lambda_{\mathrm{PB}}^2 P_{\mathrm{PB}}\mu}{16p_{\mathrm{Tx}}}\right). \tag{5.10}$$

We then add the first condition $P_{\max} > p_{\mathrm{Tx}} \geq \mu\gamma_{\mathrm{PT}}$ to the above unconditional distribution. According to the conditional probability distribution relationship, the distribution of the transmit power for active Tx is

$$f_{P_{\mathrm{Tx}}}(p_{\mathrm{Tx}}) = \frac{\pi^{1.5}\lambda_{\mathrm{PB}}\sqrt{P_{\mathrm{PB}}\mu}}{4p_{\mathrm{Tx}}^{1.5}(1-\mathcal{P}_{\mathrm{out}}^{\mathrm{P}})} \exp\left(-\frac{\pi^4\lambda_{\mathrm{PB}}^2 P_{\mathrm{PB}}\mu}{16p_{\mathrm{Tx}}}\right), \qquad P_{\max} > p_{\mathrm{Tx}} \geq \mu\gamma_{\mathrm{PT}}. \tag{5.11}$$

Finally, we incorporate the second condition due to the power amplifier rating for each Tx. For example, when the converted transmit power P_{Tx} that is higher than $P_{\max}$, it will be capped by $P_{\max}$. Under $P_{\mathrm{Tx}} \geq P_{\max}$ scenario, the distribution of P_{Tx} is

$$\begin{aligned} f_{P_{\mathrm{Tx}}}(p_{\mathrm{Tx}}) =& \int_{P_{\max}}^{\infty} \frac{\pi^{1.5}\lambda_{\mathrm{PB}}\sqrt{P_{\mathrm{PB}}\mu}}{4p_{\mathrm{Tx}}^{1.5}(1-\mathcal{P}_{\mathrm{out}}^{\mathrm{P}})} \exp\left(-\frac{\pi^4\lambda_{\mathrm{PB}}^2 P_{\mathrm{PB}}\mu}{16p_{\mathrm{Tx}}}\right) \mathrm{d}p_{\mathrm{Tx}}\delta(p_{\mathrm{Tx}}-P_{\max}) \\ =& \frac{1-F_{P_{\mathrm{PT}}}(\mu^{-1}P_{\max})}{1-\mathcal{P}_{\mathrm{out}}^{\mathrm{P}}}\delta(p_{\mathrm{Tx}}-P_{\max}) \\ =& \frac{1-F_{P_{\mathrm{Tx}}}(P_{\max})}{1-\mathcal{P}_{\mathrm{out}}^{\mathrm{P}}}\delta(p_{\mathrm{Tx}}-P_{\max}), \qquad p_{\mathrm{Tx}} \geq P_{\max}. \end{aligned} \tag{5.12}$$

Combining (5.11) and (5.12), we arrive the result in (5.8). □

Using (5.8), we can also obtain the expectation term $\mathbb{E}\{\sqrt{P_{\mathrm{Tx}}}\}$ for $\alpha = 4$ as

$$\mathbb{E}\{\sqrt{P_{\mathrm{Tx}}}\} = \frac{\pi^{1.5}\lambda_{\mathrm{PB}}\sqrt{P_{\mathrm{PB}}\mu}}{4(1-\mathcal{P}_{\mathrm{out}}^{\mathrm{P}})}\Gamma\left[0, \frac{\pi^4\lambda_{\mathrm{PB}}^2 P_{\mathrm{PB}}\mu}{16P_{\max}}, \frac{\pi^4\lambda_{\mathrm{PB}}^2 P_{\mathrm{PB}}}{16\gamma_{\mathrm{PT}}}\right] + \frac{1-F_{P_{\mathrm{PT}}}(\mu^{-1}P_{\max})}{1-\mathcal{P}_{\mathrm{out}}^{\mathrm{P}}}\sqrt{P_{\max}}. \tag{5.13}$$

In the proposed system model, the location of the active Txs as well as their transmit powers rely strongly on the PB locations. Indeed active Txs are likely to be located closer to PBs, which means that their transmit powers and locations are correlated. In this work, for analytical tractability, we assume that each active Tx's transmit power and location is independent. Thus, we approximate the active Txs as a homogeneous PPP with node density $\lambda'_{\mathrm{Tx}} = (1-\mathcal{P}_{\mathrm{out}}^{\mathrm{P}})\lambda_{\mathrm{Tx}}$, denoted as Φ'_{Tx}.

The instantaneous SINR at reference Rx, Y_0, is then given as

$$\mathrm{SINR} = \frac{P_{\mathrm{Tx}_0}G_0 r_0^{-\alpha}}{\sum_{X\in\Phi'_{\mathrm{Tx}}} P_{\mathrm{Tx}_X}G_X R_X^{-\alpha} + \mathcal{N}'}, \tag{5.14}$$

where R_X is the random distance between Y_0 and interfering Tx X, $\mathcal{N}$ is the AWGN power and G_0 and G_X denote the fading power gains on the reference link and interference link, respectively. Note that P_{Tx_0} and P_{Tx_X} are the transmit power for the reference Tx and other active Txs, respectively, which have the same distribution as given in (5.8). The subscript 0 here is used to distinguish the reference node from other nodes. Using the stochastic geometry, we obtain the channel outage probability as summarized in Proposition 8.

Proposition 8. *For the considered SWIPT system model as described in Section 5.1, the channel outage probability experienced at the typical Rx is given by*

$$\mathcal{P}_{out}^{C} = \mathbb{E}_{P_{Tx_0}}\left\{\underbrace{1-\exp\left(-\frac{\mathcal{N}r_0^{\alpha}}{P_{Tx_0}}\gamma_{th}\right)\exp\left(-\frac{(1-\mathcal{P}_{out}^{P})\lambda_{Tx}\pi^2 r_0^2\sqrt{\gamma_{th}}}{2\sqrt{P_{Tx_0}}}\mathbb{E}\{\sqrt{P_{Tx}}\}\right)}_{\mathcal{P}_{out}^{C}|_{P_{Tx_0}}(P_{Tx_0})}\right\}, \tag{5.15}$$

where γ_{th} is the SINR threshold, the term $\mathcal{P}_{out}^{C}|_{P_{Tx_0}}(P_{Tx_0})$ can be regarded as the conditional channel outage probability which is conditioned on the transmit power of the reference Tx, and $\mathbb{E}\{\sqrt{P_{Tx}}\}$ is given in (5.13).

Proof. The channel outage is defined as the event that the SINR at the Rx is below the SINR

threshold γ_{th}. By substituting the SINR given in (5.14), we have channel outage probability as

$$\mathcal{P}_{\text{out}}^{\text{C}} = \Pr\left(\frac{P_{\text{Tx}_0} G_0 r_0^{-\alpha}}{\sum_{X\in\Phi'_{\text{Tx}}} P_{\text{Tx}_X} G_X R_X^{-\alpha} + \mathcal{N}} < \gamma_{\text{th}}\right). \tag{5.16}$$

After rearranging the above the equation, we can re-write the channel outage probability as

$$\begin{aligned}
\mathcal{P}_{\text{out}}^{\text{C}} =& \mathbb{E}_{P_{\text{Tx}_0}}\left\{\Pr\left(G_0 < \frac{\sum_{X\in\Phi'_{\text{Tx}}} P_{\text{Tx}_X} G_X R_X^{-\alpha} + \mathcal{N}}{P_{\text{Tx}_0} r_0^{-\alpha}\gamma_{\text{th}}^{-1}}\right)\right\} \\
=& \mathbb{E}_{P_{\text{Tx}_0}}\left\{\mathbb{E}_{\Phi'_{\text{Tx}},G,P_{\text{Tx}}}\left\{F_{G_0}\left(\frac{\sum_{X\in\Phi'_{\text{Tx}}} P_{\text{Tx}_X} G_X R_X^{-\alpha} + \mathcal{N}}{P_{\text{Tx}_0} r_0^{-\alpha}\gamma_{\text{th}}^{-1}}\right)\right\}\right\} \\
=& \mathbb{E}_{P_{\text{Tx}_0}}\left\{1-\exp\left(-\frac{\mathcal{N} r_0^{\alpha}}{P_{\text{Tx}_0}}\gamma_{\text{th}}\right)\mathbb{E}_{\Phi'_{\text{Tx}},G,P_{\text{Tx}}}\left\{\exp\left(\frac{\sum_{X\in\Phi'_{\text{Tx}}} P_{\text{Tx}_X} G_X R_X^{-\alpha}}{P_{\text{Tx}_0} r_0^{-\alpha}\gamma_{\text{th}}^{-1}}\right)\right\}\right\} \\
=& \mathbb{E}_{P_{\text{Tx}_0}}\left\{1-\exp\left(-\frac{\mathcal{N} r_0^{\alpha}}{P_{\text{Tx}_0}}\gamma_{\text{th}}\right)\right. \\
&\qquad \left.\times \exp\left(-\int_0^{\infty}\mathbb{E}_{G,P_{\text{Tx}}}\left\{1-\exp\left(-\frac{P_{\text{Tx}} G r_X^{-\alpha}}{P_{\text{Tx}_0} r_0^{-\alpha}\gamma_{\text{th}}^{-1}}\right)\right\} 2\pi\lambda'_{\text{Tx}} r_X \,\mathrm{d}r_X\right)\right\} \\
=& \mathbb{E}_{P_{\text{Tx}_0}}\left\{\underbrace{1-\exp\left(-\frac{\mathcal{N} r_0^{\alpha}}{P_{\text{Tx}_0}}\gamma_{\text{th}}\right)\exp\left(-\frac{\lambda'_{\text{Tx}}\pi^2 r_0^2\sqrt{\gamma_{\text{th}}}}{2\sqrt{P_{\text{Tx}_0}}}\mathbb{E}\{\sqrt{P_{\text{Tx}}}\}\right)}_{\mathcal{P}_{\text{out}}^{\text{C}}|_{P_{\text{Tx}_0}}(P_{\text{Tx}_0})}\right\},
\end{aligned} \tag{5.17}$$

where the third step comes from the fact that the reference link experiences Rayleigh fading (i.e., G_0 follows the exponential distribution) and the fourth step is based on the Campbell's theorem [71]. □

5.2.3 Total Outage Probability

According the total outage probability shown in (5.1), combining the power outage probability in (5.6) and the channel outage probability in (5.15), the total outage probability at a typical Rx, Y_0, is

$$\begin{aligned}
\mathcal{P}_{\text{out}} =& \mathcal{P}_{\text{out}}^{\text{P}} + \left(1 - F_{P_{\text{PT}}}(\mu^{-1}P_{\max})\right)\left(\mathcal{P}_{\text{out}}^{\text{C}}|_{P_{\text{Tx}_0}}(P_{\max})\right) \\
&+ (1-\mathcal{P}_{\text{out}}^{\text{P}})\int_{\mu\gamma_{\text{PT}}}^{P_{\max}} \mathcal{P}_{\text{out}}^{\text{C}}|_{P_{\text{Tx}_0}}(p_{\text{Tx}_0}) f_{P_{\text{Tx}_0}}(p_{\text{Tx}_0})\,\mathrm{d}p_{\text{Tx}_0},
\end{aligned} \tag{5.18}$$

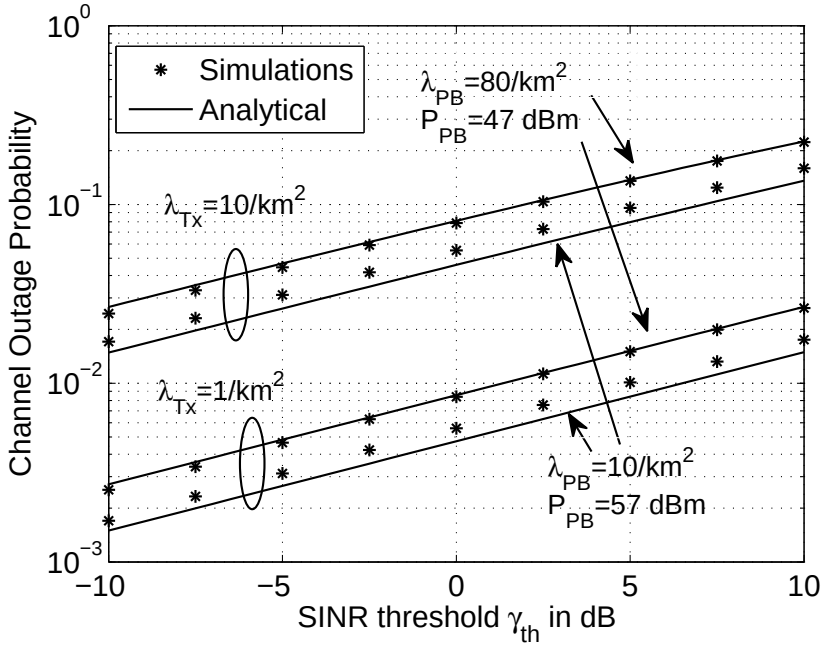

Figure 5.3: The channel outage probability versus the SINR threshold γ_{th}.

where $f_{P_{\text{Tx}_0}}(p_{\text{Tx}_0})$ is the distribution of the transmit power for active Tx given in (5.8). Note that (5.18) cannot be expressed in closed-form due to the complexity of the term $\mathcal{P}^{\text{C}}_{\text{out}}|_{P_{\text{Tx}_0}}(P_{\text{Tx}_0})$ which is inside the integration. However, (5.18) can be easily evaluated numerically.

5.3 Results

In this section, we first establish the accuracy of the derived analytical results by comparing with simulations. We then study the effects of the PB's node density, PB's transmit power and the power receiver activation threshold. Unless specified otherwise, the main system parameters are set as follows: path-loss exponent $\alpha = 4$, distance of reference link between Tx and Rx $r_0 = 20$ m, power receiver activation threshold $\gamma_{\text{PT}} = -30$ dBm [102], SINR threshold $\gamma_{\text{th}} = 0$ dB [71], AWGN power $\mathcal{N} = -130$ dBm, time ratio $\tau = 0.5$, power conversion efficiency $\eta = 0.5$ and maxim transmit power of Tx $P_{\max} = 30$ dBm.

5.3.1 Accuracy of Derived Analytical Results

Figure 5.3 plots the channel outage probability versus SINR threshold γ_{th} with $\lambda_{\text{PB}} = 10, 80/\text{km}^2$, $P_{\text{PB}} = 47, 57$ dBm and $\lambda_{\text{Tx}} = 1, 10/\text{km}^2$. Note that the unit for λ_{PB} is PBs/km^2 and the unit for λ_{Tx} is Txs/km^2. The simulation results are averaged over 1 million realizations. The analytical result is calculated using Proposition 8. The figure shows that there is a small gap between

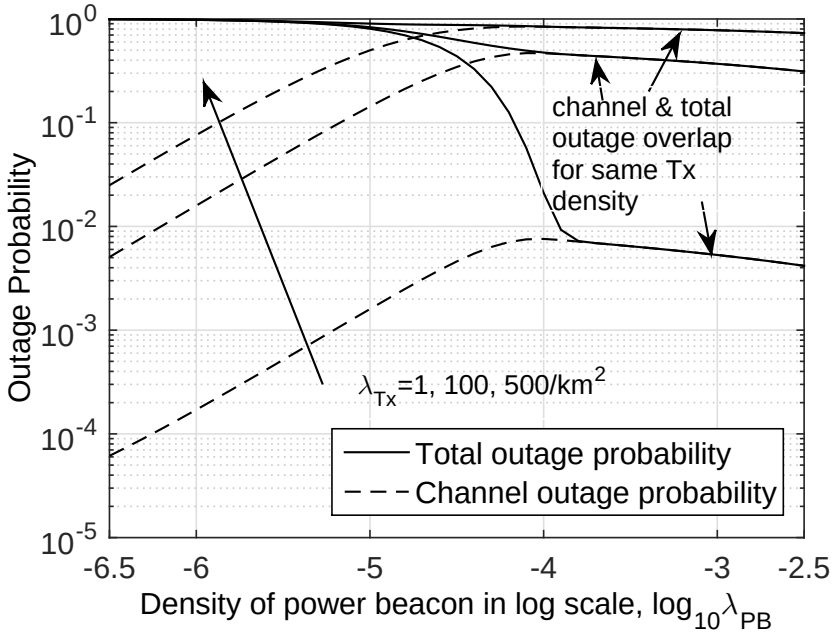

Figure 5.4: The channel outage probability and total outage probability versus the PB's node density.

the analytical and simulation results. This is due to the independence assumption of the active Tx's location and transmit powers, which has been used in the derivation. However, the trend of the analytical results is the same as the simulation results. This confirms the accuracy of the derived analytical expressions. In addition, we can see that increasing γ_{th} degrades channel the channel outage probability because the SINR is less likely to achieve the higher SINR threshold γ_{th} value.

Next, we will use the analytical results to show the impact of the important system parameters (i.e., λ_{PB}, P_{PB} and γ_{PT}) on the channel outage probability and total outage probability.

5.3.2 Effect of Power Beacon's Node Density

Figure 5.4 plots the channel outage probability and total outage probability versus the PB's node density λ_{PB}, with $P_{\text{PB}} = 47$ dBm and $\lambda_{\text{Tx}} = 1, 100, 500/\text{km}^2$. First we examine the effect on the channel outage probability. Figure 5.4 shows that as the PB's node density increases, the channel outage probability first increases and then decreases. This can be explained as the result of interplay between two factors: the probability of being active for Txs, $(1 - \mathcal{P}^{\text{P}}_{\text{out}})$, and the distribution of the transmit power, $f_{P_{\text{Tx}}}(p_{\text{Tx}})$. When the PB's node density increases, the probability of being active increases (i.e., more Txs are likely to be active). At the same time, the peak of $f_{P_{\text{Tx}}}(p_{\text{Tx}})$ is shifted to the right, which means that Tx's transmit power is more likely to be greater. Initially, the probability of being active dominantly determines the

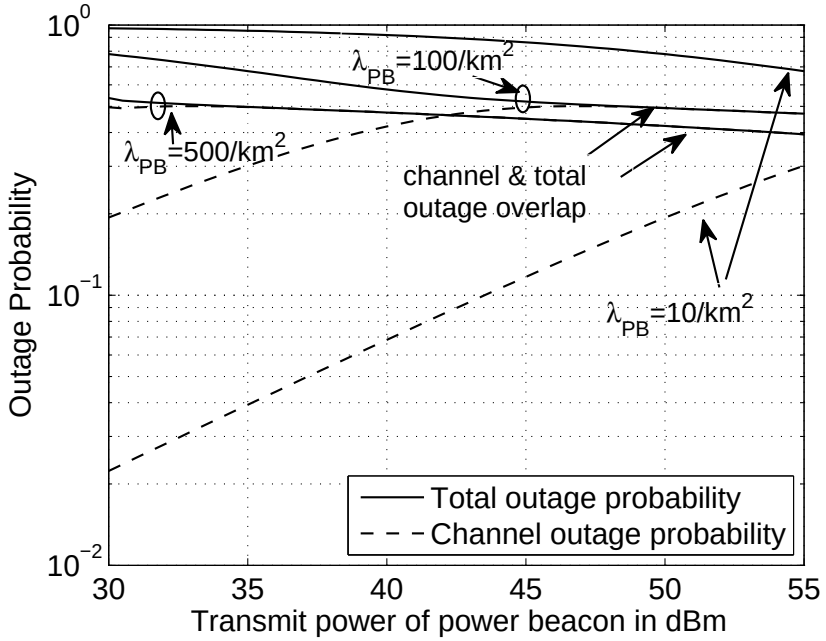

Figure 5.5: The channel outage probability and total outage probability versus the PB's transmit power.

channel outage probability as shown in Figure 5.4. For example, as the probability of being active increases, the number of interfering Txs increases, which generates more interference and degrades the channel outage probability. However, when the PB's node density increases beyond a certain value, $f_{P_{\text{Tx}}}(p_{\text{Tx}})$ begins to plays the dominant role. Thus, even through the number of interferer Txs is large, the reference Tx is likely to support its Rx with a higher transmit power which slightly improves the channel outage probability.

Next, we examine the effect on the total outage probability. Initially, the power outage probability plays the dominant role in determining the total outage probability. This is because when the PB's node density is small, the power outage probability is several orders of magnitude greater than the channel outage probability. With the number of PBs increases, more Txs can be active. Thus, the power outage probability decreases as λ_{PB} increases and so does the total outage probability. Eventually, when the PB's node density is high, the power outage probability becomes negligible small. The channel outage probability plays the dominant role, and the total outage probability and the channel outage probability overlap. In general, as the PB's node density, the total outage probability is always decreasing.

5.3.3 Effect of Power Beacon's Transmit Power

Figure 5.5 plots the channel outage probability and total outage probability versus the PB's transmit power P_{PB}, with $\lambda_{\text{PB}} = 10, 100, 500/\text{km}^2$ and $\lambda_{\text{Tx}} = 100/\text{km}^2$. The figure shows

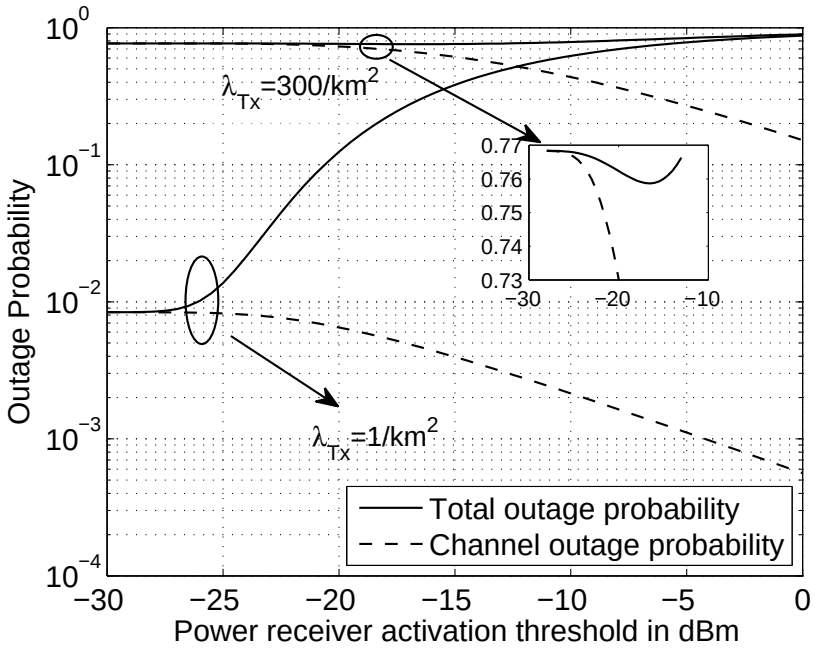

Figure 5.6: The channel outage probability and total outage probability versus the power receiver activation threshold.

that the effect of the PB's transmit power depends on the PB's node density, λ_{PB}. When $\lambda_{\text{PB}} = 10/\text{km}^2$ (i.e., small), the channel outage probability increases as the PB's transmit power increase in the considered range of P_{PB}. However, in this case, the majority of Txs are in power outage due to the small number of PBs. Hence, the total outage probability is largely determined by the power outage probability (i.e., decreases as P_{PB} increases). When $\lambda_{\text{PB}} = 100/\text{km}^2$, increasing the PB's transmit power improves the power outage probability and hence the total outage probability, until the channel outage probability becomes dominant when the channel outage probability and the total outage probability curves merge. Finally, when $\lambda_{\text{PB}} = 500/\text{km}^2$ (i.e., large), nearly all Txs are always active. Hence, the channel outage probability and the total outage probability overlap and slightly decrease as PB's transmit power increases. These trends, which we have observed to be valid as long as Tx's node density is not too large, can be explained using similar arguments as before.

5.3.4 Effect of Power Receiver Activation Threshold

Figure 5.6 plots the channel outage probability and total outage probability versus the power receiver activation threshold γ_{PT}, with $\lambda_{\text{Tx}} = 1,300/\text{km}^2$, $\lambda_{\text{PT}} = 200/\text{km}^2$ and $P_{\text{PT}} = 47$ dBm. From the figure, we can see that the channel outage probability decreases as the power receiver activation threshold increases. This is because a larger value of γ_{PT} prohibits more

Txs from being active and the interference at the reference Rx is consequently reduced.

As for the total outage probability, when the Tx's node density is low, the total outage probability increases as the power receiver activation threshold increases. This is because the power outage probability (which is far greater than the channel outage probability for low λ_{Tx}) increases as γ_{PT} increases and plays the dominant role in determining the total outage probability. When the Tx's node density is large, the total outage probability first decreases and then increases with increasing the power receiver activation threshold. This is due to the interaction of the power outage probability and the channel outage probability, since the power outage probability increases as γ_{PT} increase, while the channel outage probability is always decreasing.

5.4 Summary

In this chapter, we investigated the total outage probability performance inside ad-hoc networks with SWIPT, where the transmitters are wirelessly charged by power beacons and then transmit information to their receivers. Note that the total outage probability is determined by the channel outage probability and power outage probability. Therein, the power outage occurs when the received power is not enough to active the energy harvesting circuit. By formulating the analytical expression for these outage probabilities, we studied the impact of the system parameters. We observed that, although increasing the node density or transmit power of power beacons is not always favorable for the channel outage probability, it can improve the total outage performance.

Chapter 6

Conclusions and Future Research Directions

In this chapter, we summarize the general conclusions drawn from this thesis. We also outline some future research directions arising from this work.

6.1 Conclusions

Firstly, in Chapter 2, we proposed two general frameworks for analytically computing the outage probability when a finite number of nodes are distributed at random inside an arbitrarily shaped finite ad-hoc network. For the case that the random nodes are independently and uniformly distributed and the fading channels are identically, independently distributed following Nakagami-m distribution, we demonstrated the use of the frameworks to analytically compute the outage probability at any arbitrary location inside the finite wireless network. The probability density function of a random node from the reference receiver plays a key part in our frameworks and enables the accurate modeling of the boundary effects. We presented an algorithm to accurately compute the outage probability in a finite wireless network with an arbitrary shape. We also analyzed the impact of the fading channel and the shape of the region on the boundary effects. Our results showed that the impact of boundary effects is enhanced by an increase in the m value for Nakagami-m fading channels or an increase in the path-loss exponent.

We then extended the framework developed in Chapter 2 to Chapter 3. In Chapter 3, we investigated the performance of arbitrarily shaped underlay cognitive networks with different SU activity protocols. Especially, a framework based on the MGF of the interference due to a random SU was proposed and it allowed closed-form computation of the outage probability in the primary network as well as the average number of active SUs in the secondary network. We also applied cooperation in the context of the underlay cognitive network to come up with a cooperation-based SU activity protocol, which includes the existing threshold-based protocol

as a special case. We studied the average number of active SUs for the different SU activity protocols, subject to a given outage probability constraint at the PU and we used it as an analytical approach to compare the performance of different SU activity protocols in the underlay cognitive networks. Our results showed that, in the short-term sensing signal monitoring scenarios, the cooperation-based protocol improves the networks' performance compared to the threshold-based protocol.

In Chapter 4, we considered a more complex network system, in-band D2D communication underlaid with cellular network, and proposed a framework to analyze the performance of such system inside a disk region. We adopted a mode selection scheme for potential D2D users to manage the intra-cell interference experienced by the BS. We derived approximate yet accurate analytical results for the outage probability at the BS and a typical DRx, the average number of successful D2D transmissions and spectrum reuse ratio. Our derived results showed that the outage probability relies strongly on the location of DRx. They also allowed the impact of the D2D system parameters on both the average number of successful D2D transmissions and spectrum reuse ratio to be determined. For example, it was observed that, given the QoS constraint at the BS, as the D2D users' node density increases, the spectrum reuse ratio decreases. When the receiver sensitivity of the DRx is greater than the receiver sensitivity of the BS, the average number of successful D2D transmissions increases. Moreover, when the path-loss exponent on the cellular link is slightly lower than that on the D2D link, the decreasing trend for spectrum reuse ratio can become negligible. This indicated that an increasing level of D2D communication can be beneficial in future networks and provides design guidelines in the practical communication systems with D2D communication.

Finally, in Chapter 5, we formulated the outage probability of a wireless ad-hoc network with decoupled SWIPT, assuming a realistic model for wirelessly powered transmitters nodes. Different from Chapters 2, 3,4, where the network performance is mainly governed by the channel outage probability, in this chapter the total outage probability is determined by both the power outage probability and channel outage probability. The occurrence of power outage is due to the fact that the harvested energy at the receiver has to be greater than a threshold in order to activate the energy harvesting circuit, and it has been largely ignored by previous works. In particular, for $\alpha = 4$, we derived the analytical results for the power outage probability and channel outage probability. Our results showed that increasing the power beacon density and the power beacon transmit power can improve the total outage probability performance. In addition, when the node density for transmitters is low, the total outage probability improves by decreasing the power receiver activation threshold.

6.2 Future Work

A number of future research directions arise from the work presented in this thesis.

SWIPT systems inside a finite region: In Chapter 5 of this thesis, we assumed an infinite network region for analytical convenience. In practical systems, however, wireless power transfer can only work over a relatively short communication range [146]. In other words, the network region for wireless power transfer is more likely to be a finite region. In addition, when the transmission distance is limited, the link for power transfer can be better modeled as a line-of-sight (LOS) fading channel [146]. To best of our knowledge, there is no available research work analyzing the performance of SWIPT systems using stochastic geometry from the perspective of a finite network region with LOS fading.

Machine-to-machine communications: Machine-to-machine (M2M) communications is concerned with connecting a massive number of machine type devices and is a key 5G technology [147]. M2M communications requires support for a massive number of such connected devices, with small and infrequent data transmissions, reliable operation virtually all the time, extra energy efficiency and longevity requirements. Initial work can be found in [148] where the rate and energy performances of M2M communication were studied using PPP model and stochastic geometry. Analyzing the performance of M2M communication is an important open problem.

Massive multiple-input and multiple-output and millimeter wave communication: 5G systems are also likely to include massive multiple-input and multiple-output (MIMO) and millimeter wave (mmWave) technologies [4]. Massive MIMO is envisaged for base stations, where each BS is equipped with a very large number of service antennas (e.g., hundreds or thousands) and utilizes these to communicate with single-antenna terminals [149]. The mmWave system indicates that the extremely high frequency spectrum band is utilized for communication (i.e., 30 GHz to 300 GHz) [150] and it poses potential broader application in heterogeneous networks [4]. The consideration of these two technologies in conjunction with smart devices can be subject of future work.

Consideration of another point processes: In this thesis, we employed the BPP and PPP to model the wireless network system, since the independence assumption for the location results in the analytical tractability. For certain networks, the node distribution is not exactly spatially random. Instead it can be either clustered or more regular distributed [151]. For example, when users gather around Wi-Fi hot spots, the clustered point process is a better model [21]. Under the carrier sense multiple access type MAC scheme, since there is a minimum distance imposed between the transmitters, the hard-core process is more suitable [70]. Hence, it is interesting to develop frameworks to investigate the performance of future wireless networks with such clustered or regular point processes.

Appendix A

A.1 Derivation of the Distance Distribution $f_R(r)$

In this appendix, we summarize the derivation of the distance distribution results using the procedure in [65].

For the uniform BPP, the CDF $F_R(r)$ of the distance between a randomly located node and an arbitrary reference point located inside a regular convex polygon was derived in [65]. Using this result, the PDF of the Euclidean distance between the arbitrary reference point and its ith neighbor node is obtained, generalizing the result in [58]. The approach in [65] is also applicable for arbitrarily shaped convex polygons, which has been adapted in this chapter to obtain the PDF $f_R(r)$ for an arbitrary location of the reference receiver inside an arbitrarily shaped finite wireless network. The main steps of the procedure are summarized below.

Step 1: Consider a convex[1] polygon with L sides. Let S_ℓ and V_ℓ $(\ell = 1, 2, \ldots, L)$ denote the sides and the vertices, which are numbered in an anti-clockwise direction.

Step 2: Using the property of uniform BPP the CDF $F_R(r)$, which is the probability that the distance between an i.u.d. node and the reference receiver is less than or equal to r, is given by

$$F_R(r) = \frac{|\mathcal{D}(Y_0; r) \cap \mathcal{A}|}{|\mathcal{A}|} = \frac{\mathcal{O}(Y_0; r)}{|\mathcal{A}|}, \tag{A.1}$$

where $\mathcal{D}(Y_0; r)$ is a disk region centered at Y_0 with radius r and $\mathcal{O}(Y_0; r)$ is the overlap area between $\mathcal{D}(Y_0; r)$ and the network region, respectively.

Step 3: In order to find the area of overlap region $\mathcal{O}(Y_0; r)$, the approach in [65] is to first find the circular segment areas formed outside the sides (denoted as B_ℓ for side ℓ) and the corner overlap areas between two circular segments at a vertex (denoted as C_ℓ for vertex ℓ),

[1] All the interior angles are less than π radians.

and then subtract from the area of the disk. Thus, (A.1) can be expressed as

$$F_R(r) = \frac{1}{|\mathcal{A}|}\left(\pi r^2 - \sum_{\ell} B_\ell + \sum_{\ell} C_\ell\right). \tag{A.2}$$

Taking the derivative of (A.2), we have

$$f_R(r) = \frac{1}{|\mathcal{A}|}\left(2\pi r - \sum_{\ell} \frac{\mathrm{d}B_\ell}{\mathrm{d}r} + \sum_{\ell} \frac{\mathrm{d}C_\ell}{\mathrm{d}r}\right), \tag{A.3}$$

where $\mathrm{d}/\mathrm{d}r$ denotes the derivative with respective to r. Note that $\frac{\mathrm{d}B_\ell}{\mathrm{d}r}$ and $\frac{\mathrm{d}C_\ell}{\mathrm{d}r}$ depend on the radius r and location of Y_0. Following [65], they can be expressed as

$$\frac{\mathrm{d}B_\ell}{\mathrm{d}r} = 2r \arccos\left(\frac{p_{S_\ell}}{r}\right), \tag{A.4}$$

$$\frac{\mathrm{d}C_\ell}{\mathrm{d}r} = r\left(-\pi + \delta_\ell + \arccos\left(\frac{p_{S_\ell}}{r}\right) + \arccos\left(\frac{p_{S_{\ell-1}}}{r}\right)\right), \tag{A.5}$$

where p_{S_ℓ} denotes the perpendicular distance from Y_0 to the side S_ℓ, δ_ℓ represents the interior angle at vertex V_ℓ and the notation S_ℓ. Note that for $\ell = 1$, $S_{\ell-1} = S_L$.

Step 4: In order to find the perpendicular distances p_{S_ℓ}, establish a Cartesian coordinate system. For arbitrarily shaped finite regions, without loss of generality, the origin can be placed at vertex V_1. For regular convex polygons, the origin can be placed at the center of the polygon to exploit the rotational symmetry [65].

Following the steps above, and substituting the values, the distance distribution $f_R(r)$ can be derived. This is illustrated in detail in the next subsection for the case of the reference receiver located at vertex V_2 in Figure 2.2. The remaining distance distribution results used in Section 2.6 can be similarly derived, but are not included here for brevity.

A.1.1 Reference Receiver Located at Vertex V_2 in Figure 2.2

Consider the arbitrarily shaped region shown in Figure 2.2, with reference receiver located at vertex V_2.

For $0 \leq r \leq \sqrt{3}\mathcal{W}$, the disk region $\mathcal{D}(Y_0; r)$ is limited by sides S_1 and S_2 and vertex V_2, i.e., there are two circular segment areas outside S_1 and S_2, which are denoted by B_1 and B_2. Also there is a corner overlap area between them, which is denoted by C_2. Hence for this range, $f_R(r) = \frac{1}{|\mathcal{A}|}\left(2\pi r - \frac{\mathrm{d}B_1}{\mathrm{d}r} - \frac{\mathrm{d}B_2}{\mathrm{d}r} + \frac{\mathrm{d}C_2}{\mathrm{d}r}\right)$.

For $\sqrt{3}\mathcal{W} \leq r \leq 2\mathcal{W}$, the disk region $\mathcal{D}(Y_0; r)$ is limited by all four sides and three vertices V_1, V_2 and V_3, i.e., there are four circular segments formed outside all sides and three

corner overlaps between them. Hence for this range, $f_R(r) = \frac{1}{|\mathcal{A}|}\left(2\pi r - \sum_{\ell=1}^{4}\frac{\mathrm{d}B_\ell}{\mathrm{d}r} + \sum_{\ell=1}^{3}\frac{\mathrm{d}C_i}{\mathrm{d}r}\right)$.

For $r > 2\mathcal{W}$, the disk region covers the whole region in Figure 2.2 which results in $F_R(r) = 1$ and $f_R(r) = 0$. Consequently, in this case, $f_R(r)$ is a piece-wise function with two ranges only. Using (A.4) and (A.5), and simplifying, we get (2.35) which is used in the generation of the results in Figure 2.8.

Appendix B

In this appendix, we derive the moment generating function of the interference from a random SU and the corresponding n-th moment for the SU activity protocols.

From (3.4), (3.5) and (3.6), we can see that whether a random SU generates interference or not is strongly dependent on the SU's random distance to the PU-Rx, R. The conditional probability mass function (PMF) of the interference from a SU is given by

$$\Pr(I = \mathbb{I}|R,G) = \begin{cases} P_{\text{active}|R}, & \mathbb{I} = P_T G R^{-\alpha}; \\ 1 - P_{\text{active}|R}, & \mathbb{I} = 0; \end{cases} \tag{B.1}$$

where $\mathbb{I}$ is the value taken by the random variable I, and $P_{\text{active}|R}$ represents the conditional probability that a SU is active, which is conditioned on its random distance R to the PU-Rx.

Using (B.1), we can express the MGF of the interference from a random SU (defined below (3.11)) as

$$\begin{aligned} \mathcal{M}_I(s) =& \mathbb{E}_I\left\{\exp(-sI)\right\} \\ =& \mathbb{E}_G\{\mathbb{E}_R\{\Pr(I = \mathbb{I}|R,G)\exp\left(-s\mathbb{I}\right)\}\} \\ =& \mathbb{E}_G\left\{\mathbb{E}_R\left\{P_{\text{active}|R}\exp\left(-sP_T G R^{-\alpha}\right\}\right\}\right. + \mathbb{E}_G\left\{\mathbb{E}_R\left\{\left(1 - P_{\text{active}|R}\right)\exp(-s\times 0\right\}\right\} \\ =& \mathbb{E}_{G,R}\left\{P_{\text{active}|R}\exp\left(-sP_T G R^{-\alpha}\right)\right\} + 1 - \mathbb{E}_R\left\{P_{\text{active}|R}\right\}. \end{aligned} \tag{B.2}$$

Substituting (B.2) into (3.13), the n-th moment of the interference from a random SU is

$$\begin{aligned} \mu_I(n) =& (-1)^n \mathbb{E}_{G,R}\left\{P_{\text{active}|R}\left(-1\right)^n P_T^n G^n R^{-n\alpha}\exp\left(-sP_T G R^{-\alpha}\right)\right\}|_{s=0} \\ =& P_T^n \mathbb{E}_G\left\{G^n\right\}\mathbb{E}_R\left\{P_{\text{active}|R}R^{-n\alpha}\right\}. \end{aligned} \tag{B.3}$$

We now define and use the value of the conditional probability $P_{\text{active}|R}$ for different SU activity protocol to derive the main analytical results in the chapter.

B.1 Proof of Theorem 1 and Corollary 1

Proof. For the guard zone protocol, (3.4) shows that the interference from a random SU is given by $P_T G R^{-\alpha} \mathbf{1}_{\left(R>r_f\right)}$. Thus, the conditional probability that a SU is active can be expressed as

$$P_{\text{active}|R} = \begin{cases} 1, & R > r_f; \\ 0, & R \leq r_f. \end{cases} \tag{B.4}$$

Substituting (B.4) into (B.2) and (B.3), the MGF and n-th moment of the interference from a random SU for the guard zone protocol are respectively given by

$$\begin{aligned} \mathcal{M}_I(s) = &\int_0^{\infty} \left(\int_{\epsilon}^{r_f} 0 \times \exp\left(-sP_T g r^{-\alpha}\right) f_R(r)\, \mathrm{d}r + \int_{r_f}^{r_{\max}} 1 \times \exp\left(-sP_T g r^{-\alpha}\right) f_R(r)\, \mathrm{d}r \right) \\ &\times f_G(g)\, \mathrm{d}g + 1 - \left(\int_{\epsilon}^{r_f} 0 \times f_R(r)\, \mathrm{d}r + \int_{r_f}^{r_{\max}} 1 \times f_R(r)\, \mathrm{d}r \right) \\ = &\int_0^{\infty} \int_{r_f}^{r_{\max}} \exp\left(-sP_T g r^{-\alpha}\right) f_R(r) f_G(g)\, \mathrm{d}r\, \mathrm{d}g + F_R(r_f), \end{aligned} \tag{B.5}$$

and

$$\begin{aligned} \mu_I(n) = &P_T^n \mathbb{E}_G\left\{G^n\right\} \left(\int_{\epsilon}^{r_f} 0 \times R^{-n\alpha} f_R(r)\, \mathrm{d}r + \int_{r_f}^{r_{\max}} 1 \times R^{-n\alpha} f_R(r)\, \mathrm{d}r \right) \\ = &P_T^n \mathbb{E}_G\left\{G^n\right\} \int_{r_f}^{r_{\max}} R^{-n\alpha} f_R(r)\, \mathrm{d}r. \end{aligned} \tag{B.6}$$

Hence, we arrive at the results in Theorem 1 and Corollary 1. □

B.2 Proof of Theorem 2 and Corollary 2

Proof. For the threshold-based protocol, (3.5) shows that the interference from a random SU is given by $P_T G R^{-\alpha} \mathbf{1}_{\left(P_{T_S} H R^{-\alpha} \leq \xi\right)}$, i.e., the SU generates interference as long as $H \leq \frac{\xi R^{\alpha}}{P_{T_S}}$ when the distance to PU-Rx is given. Thus, the conditional probability that a SU is active can be written as

$$P_{\text{active}|R} = \int_0^{\frac{\xi R^{\alpha}}{P_{T_S}}} f_H(h)\, \mathrm{d}h = F_H\left(\frac{\xi R^{\alpha}}{P_{T_S}}\right). \tag{B.7}$$

Substituting (B.7) into (B.2) and (B.3), we can express the MGF and $\mu_I(n)$ of the interfer-

ence from a random SU as

$$\mathcal{M}_I(s) = \int_0^{\infty} \int_{\epsilon}^{r_{\max}} \exp\left(-sP_T g r^{-\alpha}\right) F_H\left(\frac{\xi r^{\alpha}}{P_{T_S}}\right) f_R(r) f_G(g)\, \mathrm{d}r\, \mathrm{d}g + 1 - \int_0^{\infty} F_H\left(\frac{\xi r^{\alpha}}{P_{T_S}}\right) f_R(r)\, \mathrm{d}r, \tag{B.8}$$

and

$$\mu_I(n) = P_T^n \mathbb{E}_G\left\{G^n\right\} \mathbb{E}_R\left\{F_H\left(\frac{\xi R^{\alpha}}{P_{T_S}}\right) R^{-n\alpha}\right\}. \tag{B.9}$$

Hence, we arrive at the results in Theorem 2 and Corollary 2. □

B.3 Proof of Proposition 1 and Corollary 3

Proof. For the cooperation-based protocol, consider a typical SU node A, cooperating with node B, as shown in Figure 3.1(c). Given the position of node A, let p_{nt} represents the conditional probability that node B leads to node A deciding not to transmit. This event occurs when node B falls into the cooperative region $\mathcal{D}_A(r_c)$ around the typical user A and the received signal at node B is greater than the activation threshold ξ. Using this fact, we can express p_{nt} as

$$p_{nt} = \int_{\mathcal{D}_A(r_c)\cap\mathcal{A}'} \int_{\frac{\xi r_B^{\alpha}}{P_{T_S}}}^{\infty} f_{H_B}(h_B)\, \mathrm{d}h_B\, \mathrm{d}x_B \mathrm{d}y_B = \int_{\mathcal{D}_A(r_c)\cap\mathcal{A}'} \left(1 - F_{H_B}\left(\frac{\xi r_B^{\alpha}}{P_{T_S}}\right)\right) \mathrm{d}x_B\, \mathrm{d}y_B, \tag{B.10}$$

where $r_B = \sqrt{x_B^2 + y_B^2}$ is the distance from node B to the PU-Rx[1], (x_B, y_B) is the coordinate of node B, $f_{H_B}(h_B)$ represents the fading power distribution on the user B's sensing channel and $\int_{\mathcal{D}_A(r_c)\cap\mathcal{A}'}$ denotes the integration over the overlap region between $\mathcal{A}'$ and $\mathcal{D}_A(r_c)$.

We can see from (B.10) that p_{nt} is a function of the location of node A. Consequently, the integration in (B.10) is very complicated to evaluate in closed-form. In order to simplify the analysis, we assume that:

- the cooperation range r_c is small compared to the size of the cognitive network region;
- the SUs within the cooperation range experience the same path-loss;
- the effect from the boundary is neglected so that the overlap region is the same as the cooperative region irrespective of location of node A.

[1]The location of PU-Rx is assumed to be at the origin.

Thus, we can approximate (B.10) as

$$p_{nt} \approx \left(1 - F_{H_B}\left(\frac{\xi R_A^{\alpha}}{P_{T_S}}\right)\right) \int_{\mathcal{D}_A(r_c)} \mathrm{d}x_B \, \mathrm{d}y_B = \frac{\pi r_c^2}{|\mathcal{A}'|} - \frac{\pi r_c^2}{|\mathcal{A}'|} F_{H_B}\left(\frac{\xi R_A^{\alpha}}{P_{T_S}}\right), \tag{B.11}$$

where R_A is the distance from node A to the PU-Rx.

The complement of the probability p_{nt}, denoted by $1 - p_{nt}$, is known as the probability that node B causes node A to transmit. In addition to node A, there are a total number of $M - 1$ SUs which are independently distributed inside the network region. Consequently, the conditional probability that $M - 1$ nodes can make node A to be active is $(1 - p_{nt})^{M-1}$, where p_{nt} is given by (B.11).

In order for node A to transmit, both the received signal powers at the SUs inside $\mathcal{D}_A(r_c)$ and the received signal power by node A on the sensing channel must be less than the activation threshold ξ. Since nodes are identically distributed, we can drop the subscript A in R_A and B in $F_{H_B}(\cdot)$. Thus, the conditional probability of a random SU being active can be expressed as

$$\begin{aligned} P_{\text{active}|R} &\approx (1 - p_{nt})^{M-1} \int_0^{\frac{\xi R^{\alpha}}{P_{T_S}}} f_H(h) \, \mathrm{d}h \\ &= \left(\frac{\left|\mathcal{A}' - \pi r_c^2\right|}{|\mathcal{A}'|} + \frac{\pi r_c^2}{|\mathcal{A}'|} F_H\left(\frac{\xi r^{\alpha}}{P_{T_S}}\right)\right)^{M-1} F_H\left(\frac{\xi r^{\alpha}}{P_{T_S}}\right). \end{aligned} \tag{B.12}$$

Then the MGF and n-th for the interference from a random SU can be obtained by substituting (B.12) into (B.2) and (B.3) respectively, which can be expressed as

$$\begin{aligned} \mathcal{M}_I(s) \approx 1 + \int_0^{\infty} \int_{\epsilon}^{r_{\max}} \exp\left(-sP_T g r^{-\alpha}\right) F_H\left(\frac{\xi r^{\alpha}}{P_{T_S}}\right) \left(\frac{\left|\mathcal{A}' - \pi r_c^2\right|}{|\mathcal{A}'|} + \frac{\pi r_c^2}{|\mathcal{A}'|} F_H\left(\frac{\xi r^{\alpha}}{P_{T_S}}\right)\right)^{M-1} \\ \times f_R(r) f_G(g) \, \mathrm{d}r \, \mathrm{d}g - \int_{\epsilon}^{r_{\max}} F_H\left(\frac{\xi r^{\alpha}}{P_{T_S}}\right) \left(\frac{\left|\mathcal{A}' - \pi r_c^2\right|}{|\mathcal{A}'|} + \frac{\pi r_c^2}{|\mathcal{A}'|} F_H\left(\frac{\xi r^{\alpha}}{P_{T_S}}\right)\right)^{M-1} f_R(r) \, \mathrm{d}r, \end{aligned} \tag{B.13}$$

and

$$\mu_I(n) \approx P_T^n \mathbb{E}_G\left\{G^n\right\} \mathbb{E}_R\left\{F_H\left(\frac{\xi R^{\alpha}}{P_{T_S}}\right) \left(\frac{\left|\mathcal{A}' - \pi r_c^2\right|}{|\mathcal{A}'|} + \frac{\pi r_c^2}{|\mathcal{A}'|} F_H\left(\frac{\xi R^{\alpha}}{P_{T_S}}\right)\right)^{M-1} R^{-n\alpha}\right\}. \tag{B.14}$$

Hence, we arrive at the results in Proposition 1 and Corollary 1. □

B.4 Proof of Theorem 3

Proof. From definition, $\overline{M}_{\text{active}}$ is the mean value of the number of active SUs, after averaging over all possible networking realizations. Let P_{active} denote the (unconditional) probability of a SU being active. Mathematically, the average number of active SUs can be written as

$$\overline{M}_{\text{active}} = M \times P_{\text{active}} = M \times \mathbb{E}_R\{P_{\text{active}|R}\}. \tag{B.15}$$

In order to further simplify (B.15), we can exploit the fact that $P_T^0 = 1$, $\mathbb{E}_G\{G^0\} = 1$ and $R^0 = 1$. Thus, we can re-write (B.15) as

$$\begin{aligned}\overline{M}_{\text{active}} =& M \times 1 \times 1 \times \mathbb{E}_R\{P_{\text{active}|R} \times 1\} \\ =& M \times \underbrace{P_T^0 \mathbb{E}_G\{G^0\} \mathbb{E}_R\{P_{\text{active}|R} \times R^0\}}_{\mu_I(0)}.\end{aligned} \tag{B.16}$$

Comparing the latter term in (B.16) with (B.3), we can see that it can be obtained from (B.3) by substituting $n = 0$, denoted as $\mu_I(0)$. Thus, we arrive at the result in (3.27). □

Appendix C

C.1 Derivation of Equation (4.4): Outage Probability

Rearranging (4.3), we have the outage probability as

$$P_{\text{out}}^{\kappa}(\gamma_{\text{th}}) = \mathbb{E}_{I_{\text{agg}}^{\kappa},G_0}\left\{\Pr\left(G_0 < \frac{\gamma_{\text{th}}}{\rho} I_{\text{agg}}^{\kappa}\right)\right\} = \mathbb{E}_{I_{\text{agg}}^{\kappa}}\left\{F_{G_0}\left(\frac{\gamma_{\text{th}}}{\rho} I_{\text{agg}}^{\kappa}\right)\right\}, \tag{C.1}$$

where $F_{G_0}(\cdot)$ is the CDF of the fading power gain on the reference link. Since we assume Nakagami-m fading with integer m for the reference link, G_0 follows the Gamma distribution with the mean 1 and the shape parameter m, and its CDF is given by $F_{G_0}(g_0) = 1 - \sum_{t=0}^{m-1} \frac{1}{t!}(mg_0)^t \exp(-mg_0)$. Hence, we can re-write (C.1) as

$$\begin{aligned} P_{\text{out}}^{\kappa}(\gamma_{\text{th}}) =& \mathbb{E}_{I_{\text{agg}}^{\kappa}}\left\{1 - \sum_{t=0}^{m-1} \frac{1}{t!}\left(m\frac{\gamma_{\text{th}}}{\rho} I_{\text{agg}}^{\kappa}\right)^t \exp\left(-m\frac{\gamma_{\text{th}}}{\rho} I_{\text{agg}}^{\kappa}\right)\right\} \\ =& 1 - \sum_{t=0}^{m-1} \frac{1}{t!}\mathbb{E}_{I_{\text{agg}}^{\kappa}}\left\{\left(m\frac{\gamma_{\text{th}}}{\rho} I_{\text{agg}}^{\kappa}\right)^t \exp\left(-m\frac{\gamma_{\text{th}}}{\rho} I_{\text{agg}}^{\kappa}\right)\right\}. \end{aligned} \tag{C.2}$$

Note the MGF of I_{agg}^{κ} is $\mathcal{M}_{I_{\text{agg}}^{\kappa}}(s) = \mathbb{E}_{I_{\text{agg}}^{\kappa}}\left\{\exp\left(-sI_{\text{agg}}^{\kappa}\right)\right\}$ and its t-th derivative with respect to s is $\frac{\mathrm{d}^t}{\mathrm{d}s^t}\mathcal{M}_{I_{\text{agg}}^{\kappa}}(s) = \mathbb{E}_{I_{\text{agg}}^{\kappa}}\left\{\frac{\mathrm{d}^t \exp\left(-sI_{\text{agg}}^{\kappa}\right)}{\mathrm{d}s^t}\right\} = \mathbb{E}_{I_{\text{agg}}^{\kappa}}\left\{\left(-I_{\text{agg}}^{\kappa}\right)^t \exp\left(-sI_{\text{agg}}^{\kappa}\right)\right\}$. By substituting $s = m\frac{\gamma_{\text{th}}}{\rho}$, we have

$$\left.\frac{\mathrm{d}^t}{\mathrm{d}s^t}\mathcal{M}_{I_{\text{agg}}^{\kappa}}(s)\right|_{s=m\frac{\gamma_{\text{th}}}{\rho}} = \mathbb{E}_{I_{\text{agg}}^{\kappa}}\left\{\left(-I_{\text{agg}}^{\kappa}\right)^t \exp\left(-m\frac{\gamma_{\text{th}}}{\rho} I_{\text{agg}}^{\kappa}\right)\right\}. \tag{C.3}$$

Substituting (C.3) into (C.2), we have

$$P_{\text{out}}^{\kappa}(\gamma_{\text{th}}) = 1 - \sum_{t=0}^{m-1} \frac{(-s)^t}{t!} \left.\frac{\mathrm{d}^t}{\mathrm{d}s^t}\mathcal{M}_{I_{\text{agg}}^{\kappa}}(s)\right|_{s=m\frac{\gamma_{\text{th}}}{\rho}}. \tag{C.4}$$

C.2 Derivation of Proposition 2: MGF of the Interference at BS

Proof. For the considered mode selection scheme, the p-DUE is in D2D mode if and only if $\rho_D R_d^{\alpha_D} R_c^{-\alpha_C} < \xi$ (equivalently, $R_c > R_d^{\frac{\alpha_D}{\alpha_C}} \left(\frac{\rho_D}{\xi}\right)^{\frac{1}{\alpha_C}} \triangleq r'_d$). Defining $\tilde{\mathcal{R}_D} \triangleq \min\left(\mathcal{R}_D, \mathcal{R}^{\frac{\alpha_C}{\alpha_D}} \left(\frac{\xi}{\rho_D}\right)^{\frac{1}{\alpha_D}}\right)$, we can then express I^{BS} as

$$I^{\text{BS}} = \begin{cases} G\rho_D R_d^{\alpha_D} R_c^{-\alpha_C}, & (r'_d \le R_c < \mathcal{R}, 0 \le R_d < \tilde{\mathcal{R}_D}); \\ 0, & (0 \le R_c < r'_d, 0 \le R_d < \tilde{\mathcal{R}_D}); \\ 0, & (0 \le R_c < \mathcal{R}, \tilde{\mathcal{R}_D} \le R_d < \mathcal{R}_D). \end{cases} \tag{C.5}$$

Using the definition of MGF, we have

$$\begin{aligned}
\mathcal{M}_{I^{\text{BS}}}(s) &= \int_0^{\tilde{\mathcal{R}_D}} \int_{r'_d}^{\mathcal{R}} \int_0^{\infty} \exp\left(-sg\rho_D r_d^{\alpha_D} r_c^{-\alpha_C}\right) f_G(g) f_{R_c}(r_c) f_{R_d}(r_d)\, \mathrm{d}g\, \mathrm{d}r_c\, \mathrm{d}r_d \\
&+ \int_0^{\tilde{\mathcal{R}_D}} \int_0^{r'_d} \int_0^{\infty} f_G(g) f_{R_c}(r_c) f_{R_d}(r_d)\, \mathrm{d}g\, \mathrm{d}r_c\, \mathrm{d}r_d + \int_{\tilde{\mathcal{R}_D}}^{\mathcal{R}_D} \int_0^{\mathcal{R}} \int_0^{\infty} f_G(g) f_{R_c}(r_c) f_{R_d}(r_d)\, \mathrm{d}g\, \mathrm{d}r_c\, \mathrm{d}r_d \\
&= 1 - \int_0^{\tilde{\mathcal{R}_D}} \left({}_2F_1\left[1, \frac{2}{\alpha_C}; 1 + \frac{2}{\alpha_C}; -\frac{\mathcal{R}^{\alpha_C}}{s\rho_D r_d^{\alpha_D}}\right] - \frac{r_d^{2\frac{\alpha_D}{\alpha_C}}\, {}_2F_1\left[1, \frac{2}{\alpha_C}; 1 + \frac{2}{\alpha_C}; -\frac{1}{s\xi}\right]}{\mathcal{R}^2 (\xi/\rho_D)^{\frac{2}{\alpha_C}}} \right) f_{R_d}(r_d)\, \mathrm{d}r_d \\
&= 1 + \frac{{}_2F_1\left[1, \frac{2}{\alpha_C}; 1 + \frac{2}{\alpha_C}; \frac{-1}{s\xi}\right]}{\mathcal{R}_D^2 \mathcal{R}^2 \tilde{\mathcal{R}_D}^{-2-\frac{2\alpha_D}{\alpha_C}} (\xi/\rho_D)^{\frac{2}{\alpha_C}}} \frac{\alpha_C}{\alpha_D + \alpha_C} \\
&- \begin{cases} \left[\frac{\alpha_C\, {}_2F_1\left[1, \frac{2}{\alpha_C}; 1 + \frac{2}{\alpha_C}; \frac{-\mathcal{R}^{\alpha_C}}{s\rho_D x^{\alpha_D}}\right] + \alpha_D\, {}_2F_1\left[1, \frac{-2}{\alpha_D}; 1 - \frac{2}{\alpha_D}; \frac{-\mathcal{R}^{\alpha_C}}{s\rho_D x^{\alpha_D}}\right]}{x^{-2}\mathcal{R}_D^2(\alpha_C + \alpha_D)} \right] \Bigg|_0^{\tilde{\mathcal{R}_D}}, & \alpha_D \neq 2; \\ \frac{2\tilde{\mathcal{R}_D}^2\, \text{MeijerG}\left[\left\{\left\{0, \frac{\alpha_C - 2}{\alpha_C}\right\}, \{2\}\right\}, \left\{\{0,1\}, \left\{\frac{-2}{\alpha_C}\right\}\right\}, \frac{\mathcal{R}^{\alpha_C}}{s\rho_D \tilde{\mathcal{R}_D}^2}\right]}{\mathcal{R}_D^2 \alpha_C}, & \alpha_D = 2; \end{cases}
\end{aligned} \tag{C.6}$$

where the final result is obtained using [152] and Mathematica software. □

C.3 Derivation of Proposition 3: MGF of the Interference from p-DUE

Proof. For a DRx located at distance d away from the BS, the interference from an i.u.d. p-DUE, I^{DRx}, is similar to (C.5) except that $G\rho_D R_d^{\alpha_D} R_c^{-\alpha_C}$ is replaced by $\frac{G\rho_D R_d^{\alpha_D}}{(R_c^2 + d^2 - 2R_c d\cos\theta)^{\frac{\alpha_D}{2}}}$, where θ is the angle formed between the Y_0-BS line and p-DUE-BS line, which is uniformly distributed between 0 and 2π (see Figure 4.1). Using the definition of MGF and simplifying,

we have

$$\mathcal{M}_{I^{\mathrm{DRx}}}(s,d) = 1 - \int_0^{\tilde{\mathcal{R}}_D} \int_{r_d'}^{\mathcal{R}} \int_0^{\pi} \frac{s\rho_D r_d^{\alpha_D}}{s\rho_D r_d^{\alpha_D} + (r_c^2 + d^2 - 2r_c d\cos\theta)^{\frac{\alpha_D}{2}}} \frac{1}{\pi} f_{R_c}(r_c) f_{R_d}(r_d)\, \mathrm{d}\theta\, \mathrm{d}r_c\, \mathrm{d}r_d, \tag{C.7}$$

where $r_d' \triangleq R_d^{\frac{\alpha_D}{\alpha_C}} \left(\frac{\rho_D}{\xi}\right)^{\frac{1}{\alpha_C}}$.

Due to the complicated expression of I^{DRx}, the closed-form results (or semi-closed form) exist only for the cases of $\alpha_D = 2$ or $\alpha_D = 4$.

• Case of $\alpha_D = 2$: Substituting $\alpha_D = 2$ into (C.7), we get

$$\begin{aligned}
\mathcal{M}_{I^{\mathrm{DRx}}}(s,d) &= 1 - \int_0^{\tilde{\mathcal{R}}_D} \int_{r_d'}^{\mathcal{R}} \int_0^{\pi} \frac{s\rho_D r_d^2}{s\rho_D r_d^2 + r_c^2 + d^2 - 2r_c d\cos\theta} \frac{1}{\pi} f_{R_c}(r_c) f_{R_d}(r_d)\, \mathrm{d}\theta\, \mathrm{d}r_c\, \mathrm{d}r_d \\
&= 1 - \int_0^{\tilde{\mathcal{R}}_D} \int_{r_d'}^{\mathcal{R}} \frac{s\rho_D r_d^2}{\sqrt{(s\rho_D r_d^2 + r_c^2 + d^2)^2 - 4r_c^2 d^2}} \frac{2r_c}{\mathcal{R}^2} f_{R_d}(r_d)\, \mathrm{d}r_c\, \mathrm{d}r_d \\
&= 1 - \int_0^{\tilde{\mathcal{R}}_D} \frac{s\rho_D r_d^2}{\mathcal{R}^2} \ln \left(\frac{\beta_1\left(r_d^2, s\rho_D, \mathcal{R}^2 - d^2, 4d^2 s\rho_D\right)}{\sqrt{\left(\left(\frac{r_d^2\rho_D}{\xi}\right)^{\frac{2}{\alpha_C}} + s\rho_D r_d^2 - d^2\right)^2 + 4d^2 s\rho_D r_d^2} + \left(\frac{r_d^2\rho_D}{\xi}\right)^{\frac{2}{\alpha_C}} + s\rho_D r_d^2 - d^2} \right) \frac{2r_d}{\mathcal{R}_D^2} \mathrm{d}r_d
\end{aligned} \tag{C.8a}$$

$$= 1 - \frac{s\rho_D \left[\Psi\left(x^2, s\rho_D, \mathcal{R}^2 - d^2, 4d^2 s\rho_D\right) - \Psi\left(x^2, s\rho_D + \frac{\rho_D}{\xi}, -d^2, 4d^2 s\rho_D\right)\right]\Big|_0^{\tilde{\mathcal{R}}_D}}{\mathcal{R}_D^2 \mathcal{R}^2}, (\alpha_C = 2), \tag{C.8b}$$

where the second and third steps come from (2.553) and (2.261) in [152], respectively, and last step is obtained using Mathematica. $\beta_1(x,a,b,c) = ax + b + \sqrt{(ax+b)^2 + cx}$, $\int_x x\beta_1(x,a,b,c)\mathrm{d}x = \Psi(x,a,b,c)$ and

$$\begin{aligned}
\Psi(x,a,b,c) = \frac{-x^2}{8} + \frac{(10ab + 3c - 2a^2 x)\sqrt{(ax+b)^2 + cx}}{16} + \frac{x^2}{2} \ln\left(\beta_1(x,a,b,c)\right) \\
- \frac{(16a^2b^2 + 16abc + 3c^2) \ln\left(c + 2a^2 x + 2a\left(b + \sqrt{(ax+b)^2 + cx}\right)\right)}{32a^4}.
\end{aligned} \tag{C.9}$$

• Case of $\alpha_D = 4$: Similar to $\alpha_D = 2$ case, via substituting $\alpha_D = 4$ into (C.7) and using

(2.553) and (2.261) in [152], we have

$$\mathcal{M}_{I^{\mathrm{DRx}}}(s,d)=1-\int_0^{\tilde{\mathcal{R}}_D}\int_{r_d'}^{\mathcal{R}}\int_0^{\pi}\frac{s\rho_D r_d^4}{2\mathbf{i}\sqrt{s\rho_D r_d^4}}\left(\frac{1}{r_c^2+d^2-2r_c d\cos\theta-\mathbf{i}\sqrt{s\rho_D r_d^4}}\right.$$
$$\left.-\frac{1}{r_c^2+d^2-2r_c d\cos\theta+\mathbf{i}\sqrt{s\rho_D r_d^4}}\right)\frac{2r_c\,\mathrm{d}\theta\,\mathrm{d}r_c}{\pi\mathcal{R}^2}f_{R_d}(r_d)\,\mathrm{d}r_d$$
$$=1-\int_0^{\tilde{\mathcal{R}}_D}\frac{\sqrt{s\rho_D r_d^4}}{2\mathbf{i}\mathcal{R}^2}\int_{r_d'}^{\mathcal{R}}\left(\frac{2r_c}{\sqrt{(r_c^2+d^2-\mathbf{i}\sqrt{s\rho_D r_d^4})^2-4r_c^2d^2}}\right.$$
$$\left.-\frac{2r_c}{\sqrt{(r_c^2+d^2+\mathbf{i}\sqrt{s\rho_D r_d^4})^2-4r_c^2d^2}}\right)\mathrm{d}r_c f_{R_d}(r_d)\,\mathrm{d}r_d$$
$$=1-\int_0^{\tilde{\mathcal{R}}_D}\mathrm{Im}\left\{\ln\frac{\beta_1\left(r_d^2,-\mathbf{i}\sqrt{s\rho_D},\mathcal{R}^2-d^2,-4\mathbf{i}\sqrt{s\rho_D}d^2\right)}{\sqrt{\left(\left(\frac{r_d^4\rho_D}{\xi}\right)^{\frac{2}{\alpha_C}}-\mathbf{i}\sqrt{s\rho_D}r_d^2-d^2\right)^2-4\mathbf{i}\sqrt{s\rho_D}d^2r_d^2}+\left(\frac{r_d^4\rho_D}{\xi}\right)^{\frac{2}{\alpha_C}}-\mathbf{i}\sqrt{s\rho_D}r_d^2-d^2}}\right\}$$
$$\times\frac{\sqrt{s\rho_D r_d^4}}{\mathcal{R}^2}\frac{2r_d}{\mathcal{R}_D^2}\mathrm{d}r_d \tag{C.10a}$$
$$=1-\frac{\mathrm{Im}\left\{\left[\Psi\left(x^2,-\mathbf{i}\sqrt{s\rho_D},\mathcal{R}^2-d^2,-4\mathbf{i}\sqrt{s\rho_D}d^2\right)-\Psi\left(x^2,\sqrt{\frac{\rho_D}{\xi}}-\mathbf{i}\sqrt{s\rho_D},-d^2,-4\mathbf{i}\sqrt{s\rho_D}d^2\right)\right]\Big|_0^{\tilde{\mathcal{R}}_D}\right\}}{(\sqrt{s\rho_D})^{-1}\mathcal{R}_D^2\mathcal{R}^2},$$
$$(\alpha_C=4), \tag{C.10b}$$

where the third step comes from the fact that the two integrated terms in the second step are conjugated such that $\frac{a-a*}{2\mathbf{i}}=\mathrm{Im}\{a\}$.

Thus, we arrive at the result in Proposition 3. □

C.4 Derivation of Corollary 4: MGF of the Interference from CUE

Proof. Since there is no constraint on the CUE, the i.u.d. CUE will always generate interference (e.g., $I_{\mathrm{C}}^{\mathrm{DRx}}=G\rho_{\mathrm{BS}}R_z^{\alpha_C}\left(R_z^2+d^2-2R_z d\cos\theta\right)^{-\frac{\alpha_D}{2}}$) to this typical DRx. As before, we can only derive the analytical result for $\alpha_D=2$ or 4.

• Case of $\alpha_D=2$: According to the definition of MGF and the expression of $I_{\mathrm{C}}^{\mathrm{DRx}}$, we have

$$\mathcal{M}_{I_C^{\mathrm{DRx}}}(s,d) = 1 - \int_0^{\mathcal{R}}\int_0^{\pi} \frac{r_z s\rho_{\mathrm{BS}} r_z^{\alpha_C}}{s\rho_{\mathrm{BS}} r_z^{\alpha_C} + (r_z^2 + d^2 - 2r_z d\cos\theta)^{\frac{\alpha_D}{2}}} \frac{1}{\pi}\frac{2r_z}{\mathcal{R}^2}\,\mathrm{d}\theta\,\mathrm{d}r_z \tag{C.11a}$$

$$= 1 - \frac{s\rho_{\mathrm{BS}}}{\mathcal{R}^2}\int_0^{\mathcal{R}} \frac{2r_z^{\alpha_C+1}dr_z}{\sqrt{(s\rho_{\mathrm{BS}} r_z^{\alpha_C} + r_z^2 + d^2)^2 - 4r_z^2 d^2}}\,\mathrm{d}r_z \tag{C.11b}$$

$$= 1 - \frac{s\rho_{\mathrm{BS}}\left[\beta_2\left(x^2, (s\rho_{\mathrm{BS}}+1)^2, d^2(s\rho_{\mathrm{BS}}-1), 4d^4 s\rho_{\mathrm{BS}}\right)\right]\Big|_0^{\mathcal{R}}}{\mathcal{R}^2(s\rho_{\mathrm{BS}}+1)^3}, \quad (\alpha_C = 2), \tag{C.11c}$$

where $\beta_2(x,a,b,c) = \sqrt{(ax+b)^2+c} - b\ln\left(ax+b+\sqrt{(ax+b)^2+c}\right)$.

• Case of $\alpha_D = 4$: Similarly, substituting $\alpha_D = 4$ into (C.11a), we get

$$\mathcal{M}_{I_C^{\mathrm{DRx}}}(s,d) = 1 - \int_0^{\mathcal{R}} \mathrm{Im}\left\{\frac{r_z^{\alpha_C/2}}{\sqrt{\left(r_z^2 + d^2 - \mathbf{i}\sqrt{s\rho_{\mathrm{BS}} r_z^{\alpha_C}}\right)^2 - 4r_z^2 d^2}}\right\}\frac{2r_z\sqrt{s\rho_{\mathrm{BS}}}}{\mathcal{R}^2}\,\mathrm{d}r_z \tag{C.12a}$$

$$= 1 - \mathrm{Im}\left\{\frac{\sqrt{s\rho_{\mathrm{BS}}}\left[\beta_2\left(x^2, 1-\mathbf{i}\sqrt{s\rho_{\mathrm{BS}}}, -d^2\frac{1+\mathbf{i}\sqrt{s\rho_{\mathrm{BS}}}}{1-\mathbf{i}\sqrt{s\rho_{\mathrm{BS}}}}, \frac{-4\mathbf{i}\sqrt{s\rho_{\mathrm{BS}}}d^4}{(1-\mathbf{i}\sqrt{s\rho_{\mathrm{BS}}})^2}\right)\right]\Big|_0^{\mathcal{R}}}{\mathcal{R}^2(1-\mathbf{i}\sqrt{s\rho_{\mathrm{BS}}})^2}\right\}, \quad (\alpha_C = 4). \tag{C.12b}$$

Note the step in (C.11c) and step in (C.12b) come from [152, (2.264)]. □

C.5 Derivation of Proposition 4: Average Number of Successful D2D Transmissions

Proof. Using the definition in Section 4.3.1.1, the average number of successful D2D transmissions can be mathematically written as

$$\bar{M} = \mathbb{E}_\Phi\left\{\sum_{X_i\in\Phi} \mathbf{1}(X_j \in \Phi^{\mathrm{DUE}})\mathbf{1}(\mathrm{SIR}^{\mathrm{DRx}}(X_j, Y_j) > \gamma_{\mathrm{th}})\right\}. \tag{C.13}$$

As mentioned in Section 4.2.3, the location of underlay DRxs (i.e., whose corresponding p-DUE is in underlay D2D mode) follows the PPP. According to the reduced Campbell

measure [71], we can re-write (C.13) as

$$\begin{aligned}\bar{M} &= \int_{\mathcal{A}} \mathbf{1}(X_0 \in \Phi^{\mathrm{DUE}}) \mathrm{Pr}^{!}_{X_0}\left(\mathrm{SIR}^{\mathrm{DRx}}(X_0, Y_0) > \gamma_{\mathrm{th}}\right) \lambda \, \mathrm{d}X_0 \\ &= \int_{\mathcal{A}^{\mathrm{DRx}}} \mathbf{1}(Y_0 \in \Phi_u^{\mathrm{DRx}}) \left(1 - P_{\mathrm{out}}^{\mathrm{DRx}}(\gamma_{\mathrm{th}}, Y_0)\right) \lambda^{\mathrm{DRx}}(Y_0) \, \mathrm{d}Y_0 \\ &= \int_0^{\mathcal{R}+\mathcal{R}_D} p_{\mathrm{D2D}}(d) \left(1 - P_{\mathrm{out}}^{\mathrm{DRx}}(\gamma_{\mathrm{th}}, d)\right) \lambda^{\mathrm{DRx}}(d) 2\pi d \, \mathrm{d}d, \end{aligned} \tag{C.14}$$

where $\mathrm{Pr}^{!}_{X}(\cdot)$ is the reduced Palm distribution, $\mathcal{A}^{\mathrm{DRx}}$ is the network region for DRxs (e.g., a disk region with radius $\mathcal{R} + \mathcal{R}_D$). The second step in (C.14) results from the Slivnyak's theorem and the fact that we interpret this reduced Campbell measure from the point view of DRx, while the last step in (C.14) is based on the isotropic property of the underlay network region and the independent thinning property of PPP. □

C.6 Derivation of Proposition 5: Node Density of DRxs

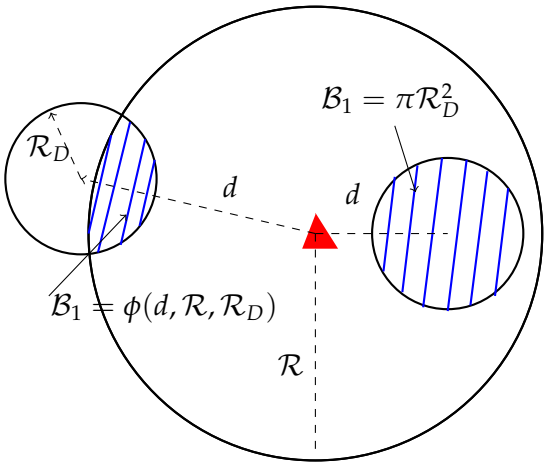

Figure C.1: Illustration of results in Proposition 5.

Proof. Rather than considering that there is a DRx uniformly distributed around the p-DUE, we can consider that for each DRx, there is a p-DUE which is uniformly distributed inside the disk region formed around DRx. If the network region is infinite, the p-DUE's node density inside the region $\pi\mathcal{R}_D^2$ is λ. As a result, the node density for DRx is λ.

However, since we are considering a finite region (i.e., a disk region), the p-DUE's node density is no longer λ at certain locations (e.g., the cell edge). Hence, the DRx's node density is not λ. Instead, the node density becomes $\lambda \frac{\mathcal{B}_1}{\pi\mathcal{R}_D^2}$, which depends on the location of DRx, where $\mathcal{B}_1$ denotes the overlap region between the cell network region $\pi\mathcal{R}^2$ and the disk region $\pi\mathcal{R}_D^2$ centered at the DRx which is d away from BS.

As illustrated in Figure C.1, when $d \in [0, \mathcal{R} - \mathcal{R}_D)$, the disk region formed around DRx is always inside the network region. That is to say, $\mathcal{B}_1$ is always $\pi\mathcal{R}_D^2$. Thus, we have $\lambda^{\text{DRx}}(d) = \lambda$ within the considered range. However, for the case that $d \in [\mathcal{R} - \mathcal{R}_D, \mathcal{R} + \mathcal{R}_D)$, the $\mathcal{B}_1$ becomes $\psi(d, \mathcal{R}, \mathcal{R}_D)$, where $\psi(d, \mathcal{R}, \mathcal{R}_D)$ is the overlap region formed by two disk with radii $\mathcal{R}$ and $\mathcal{R}_D$ which is separated by distance d and its formulation is presented in (4.11) in Lemma 1. Then we have $\lambda^{\text{DRx}}(d) = \lambda \frac{\psi(d,\mathcal{R},\mathcal{R}_D)}{\pi\mathcal{R}_D^2}$. For the rest of range (i.e., $d \geq \mathcal{R} + \mathcal{R}_D$), $\lambda^{\text{DRx}}(d) = 0$. Hence, we arrive at the result in Proposition 5. □

C.7 Derivation of Proposition 6: the Probability of being in D2D Mode

Proof. Assume that a DRx is located at distance d away from the BS. Similar to the derivation of Proposition 5, we consider that, for this DRx, there is a p-DUE uniformly surrounding it[1].

According to the considered mode selection scheme, this DRx is in underlay if its corresponding p-DUE satisfies $\rho_D R_d^{\alpha_D} < \xi R_c^{\alpha_C}$. Due to the analytical complexity, we can only find the exact result for the same path-loss case, while an approximate result can be derived for different path-loss values.

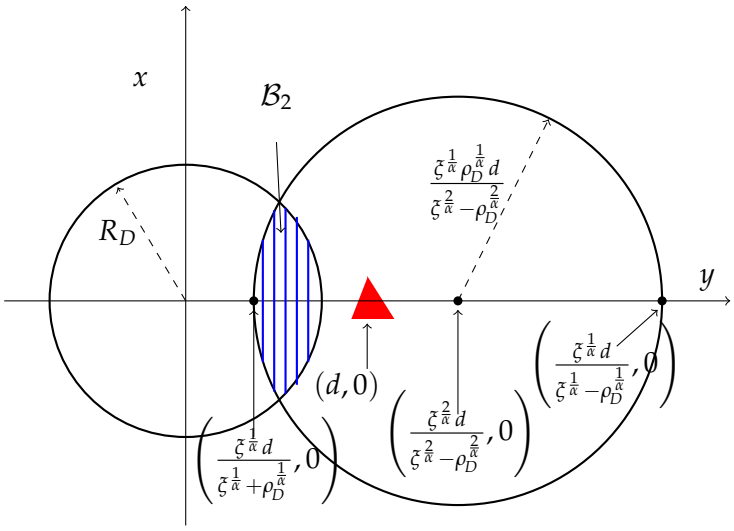

Figure C.2: Illustration of results in Proposition 6.

[1] In fact, at the cell edge, the possible location of p-DUE is no longer a disk region. In this analysis, we consider the case where the radius of the network region is large compared to $\mathcal{R}_D$ such that, for those DRx in the range of $[\mathcal{R} - \mathcal{R}_D, \mathcal{R} + \mathcal{R}_D]$, $p_{\text{D2D}}(d) = 1$. However, our result can be easily extended to the other possible scenarios. For the sake of brevity, we do not show those results here.

C.7.1 Same Path-loss Exponent

Let us consider the case $\alpha_C = \alpha_D \triangleq \alpha$. Note that the maximum range for R_d is $\mathcal{R}_D$, while the minimum range of R_c is $\max(0, d - \mathcal{R}_D)$. Assuming $d > \mathcal{R}_D$, if $\rho_D \mathcal{R}_D^{\alpha}$ is less than $\xi (d - \mathcal{R}_D)^{\alpha}$ (equivalently, $d \geq \left(1 + \left(\frac{\rho_D}{\xi}\right)^{\frac{1}{\alpha}}\right)\mathcal{R}_D$), the probability that a p-DUE is in D2D mode is 1. Because for any possible location of p-DUE in the disk region centered at DRx, the p-DUE's distance to the BS is always greater than $\mathcal{R}_D$ (i.e., the p-DUE's maximum distance to its DRx). Consequently, for the case that $d \geq \left(1 + \left(\frac{\rho_D}{\xi}\right)^{\frac{1}{\alpha}}\right)\mathcal{R}_D$, $p_{\mathrm{D2D}}(d)$ is always 1.

Under the scenario that $d < \left(1 + \left(\frac{\rho_D}{\xi}\right)^{\frac{1}{\alpha}}\right)\mathcal{R}_D$, the analysis is more complicated. Let us consider the case of $\xi > \rho_D$. The location of DRx is assumed to be at the origin and the BS is d away from the DRx. For example, the coordinate of BS is $(d, 0)$, as shown in Figure C.2. Let (x, y) denote the coordinate of p-DUE. This p-DUE is not in D2D mode if the following requirement is met, i.e., $\rho_D \left(x^2 + y^2\right)^{\frac{\alpha}{2}} > \xi \left((d - x)^2 + y^2\right)^{\frac{\alpha}{2}}$. Note that $R_d = \sqrt{x^2 + y^2}$ and $R_c = \sqrt{(d - x)^2 + y^2}$. After rearranging this inequality, we have

$$\left(x - \frac{\xi^{\frac{2}{\alpha}} d}{\xi^{\frac{2}{\alpha}} - \rho_D^{\frac{2}{\alpha}}}\right)^2 + y^2 < \left(\frac{\xi^{\frac{1}{\alpha}} \rho_D^{\frac{1}{\alpha}} d}{\xi^{\frac{2}{\alpha}} - \rho_D^{\frac{2}{\alpha}}}\right)^2. \tag{C.15}$$

The above expression can be interpreted as follows: if p-DUE is inside a disk region centered at $\left(\frac{\xi^{\frac{2}{\alpha}} d}{\xi^{\frac{2}{\alpha}} - \rho_D^{\frac{2}{\alpha}}}, 0\right)$ with radius $\frac{\xi^{\frac{1}{\alpha}} \rho_D^{\frac{1}{\alpha}} d}{\xi^{\frac{2}{\alpha}} - \rho_D^{\frac{2}{\alpha}}}$, this P-DUE is not in D2D mode. Moreover, since the p-DUE is always surrounding around its DRx, the p-DUE is confined within the disk region centered at origin with radius $\mathcal{R}_D$. Combining these two requirements, we obtain that when the p-DUE is inside the overlap region of these two disk regions (i.e., the shaded area in Figure C.2, denoted as $\mathcal{B}_2$), this p-DUE is not in D2D mode. Hence, we have the probability that a p-DUE is in D2D mode is $1 - \frac{\mathcal{B}_2}{\pi \mathcal{R}_D^2}$. Note that $\mathcal{B}_2 = \psi\left(\frac{\xi^{\frac{2}{\alpha}} d}{\xi^{\frac{2}{\alpha}} - \rho_D^{\frac{2}{\alpha}}}, \mathcal{R}_D, \frac{\xi^{\frac{1}{\alpha}} \rho_D^{\frac{1}{\alpha}} d}{\xi^{\frac{2}{\alpha}} - \rho_D^{\frac{2}{\alpha}}}\right)$ if $d \geq \left(1 - \left(\frac{\rho_D}{\xi}\right)^{\frac{1}{\alpha}}\right)\mathcal{R}_D$, while $\mathcal{B}_2 = \pi \left(\frac{\xi^{\frac{1}{\alpha}} d}{\xi^{\frac{1}{\alpha}} - \rho_D^{\frac{1}{\alpha}}}\right)^2$ for $d < \left(1 - \left(\frac{\rho_D}{\xi}\right)^{\frac{1}{\alpha}}\right)\mathcal{R}_D$, where $\psi(\cdot, \cdot, \cdot)$ is defined in (4.11) in Lemma 1.

Likewise, we can derive $p_{\mathrm{D2D}}(d)$ for $\xi \leq \rho_D$ using the same approach. For the sake of brevity, we do not present the derivation here.

C.7.2 Different Path-loss Exponent

We can directly write the probability of being in D2D mode as

$$\begin{aligned} p_{\mathrm{D2D}}(d) &= \Pr\left(\rho_D R_d^{\alpha_D} R_c^{-\alpha_C} < \xi\right) \overset{(a)}{\approx} \Pr\left(H < \frac{\xi R_c^{\alpha_C}}{\rho_D R_d^{\alpha_D}}\right) \\ &= \Pr\left(H < \frac{\xi\left(R_d^2 + d^2 - 2R_d d\cos(\theta)\right)^{\alpha_C/2}}{\rho_D R_d^{\alpha_D}}\right) \\ &\overset{(b)}{\approx} \mathbb{E}_{R_d,\theta}\left\{\left(1 - \exp\left(-\frac{N\xi\left(R_d^2 + d^2 - 2R_d d\cos(\theta)\right)^{\alpha_C/2}}{(N!)^{1/N}\rho_D R_d^{\alpha_D}}\right)\right)^N\right\}, \end{aligned} \tag{C.16}$$

where (a) comes from the introduction of a dummy random variable H, which follows the Gamma distribution with parameter N, and the fact the normalized Gamma distribution converges to identity when its parameter goes to infinity [153], and (b) comes from the approximation of a Gamma distribution [154].

It is not easy to find the closed-form result for this probability. Instead, we consider an approximation, in which the distance between BS and p-DUE R_c is approximated by the distance between BS and DRx d. Hence, by substituting $\sqrt{R_d^2 + d^2 - 2R_d d\cos(\theta)}$ by d in the above expression and using the Binomial theorem, we get

$$\begin{aligned} p_{\mathrm{D2D}}(d) &\approx 1 + \sum_{n=1}^{N}(-1)^n\binom{N}{n}\int_0^{\mathcal{R}_D}\left(1 - \exp\left(-\frac{nN\xi d^{\alpha_C}}{(N!)^{1/N}\rho_D r_d^{\alpha_D}}\right)\right)\frac{2r_d}{\mathcal{R}_D^2}\,\mathrm{d}r_d \\ &= 1 + \sum_{n=1}^{N}(-1)^n\binom{N}{n}\frac{2d^{2\frac{\alpha_C}{\alpha_D}}\left(nN\xi\right)^{\frac{2}{\alpha_D}}\Gamma\left[-\frac{2}{\alpha_D}, \frac{d^{\alpha_C} nN\xi}{(N!)^{1/N}\rho_D \mathcal{R}_D^{\alpha_D}}\right]}{\mathcal{R}_D^2\alpha_D\left((N!)^{1/N}\rho_D\right)^{\frac{2}{\alpha_D}}}. \end{aligned} \tag{C.17}$$

Thus, we obtain the probability of being in D2D mode in Proposition 6. □

Bibliography

[1] J. G. Andrews, S. Buzzi, W. Choi, S. V. Hanly, A. Lozano, A. C. K. Soong, and J. C. Zhang, "What will 5G be?" *IEEE J. Sel. Areas Commun.*, vol. 32, no. 6, pp. 1065–1082, Jun. 2014. (cited on page 1)

[2] J. Gozalvez, "5G tests and demonstrations," *IEEE Trans. Veh. Commun.*, vol. 10, no. 2, pp. 16–25, Jun. 2015. (cited on page 1)

[3] C.-L. I, C. Rowell, S. Han, Z. Xu, G. Li, and Z. Pan, "Toward green and soft: a 5G perspective," *IEEE Commun. Mag.*, vol. 52, no. 2, pp. 66–73, Feb. 2014. (cited on page 1)

[4] F. Boccardi, R. W. Heath, A. Lozano, T. L. Marzetta, and P. Popovski, "Five disruptive technology directions for 5G," *IEEE Commun. Mag.*, vol. 52, no. 2, pp. 74–80, Feb. 2014. (cited on pages 1 and 105)

[5] K. Zheng, T. Taleb, A. Ksentini, C.-L. I, T. Magedanz, and M. Ulema, "Research standards: advanced cloud virtualization techniques for 5G networks [guest editorial]," *IEEE Commun. Mag.*, vol. 53, no. 6, pp. 16–17, Jun. 2015. (cited on page 2)

[6] Qualcomm. (2015, Oct.) 1000x data challenge: small cells. [Online]. Available: https://www.qualcomm.com/1000x/small-cells (cited on page 2)

[7] T. Camp, J. Boleng, and V. Davies, "A survey of mobility models for ad hoc network research," *Wirel. Commun. Mob. Comput.*, vol. 2, no. 5, pp. 483–502, 2002. (cited on page 2)

[8] H. Hartenstein and K. P. Laberteaux, "A tutorial survey on vehicular ad hoc networks," *IEEE Commun. Mag.*, vol. 46, no. 6, pp. 164–171, Jun. 2008. (cited on page 2)

[9] C. K. Toh, *Ad Hoc Mobile Wireless Networks*. United States: Prentice Hall Publishers, 2002. (cited on page 2)

[10] "Spectrum policy task force report," *FCC Doc. ET Docket*, no. 02-135, Nov. 2002. (cited on page 2)

[11] S. Haykin, "Cognitive radio: Brain-empowered wireless communications," *IEEE J. Sel. Areas Commun.*, vol. 23, no. 2, pp. 201–220, Feb. 2005. (cited on page 2)

[12] I. F. Akyildiz, W. Y. Lee, M. C. Vuran, and S. Mohanty, "Next generation/ dynamic spectrum access / cognitive radio wireless networks: A survey," *Comput. Networks J.*, pp. 2127–2159, Sep. 2006. (cited on page 2)

[13] Q. Zhao and B. Sadler, "A survey of dynamic spectrum access," *IEEE Signal Process. Mag.*, vol. 24, no. 3, pp. 79–89, May 2007. (cited on page 2)

[14] P. Agyapong, M. Iwamura, D. Staehle, W. Kiess, and A. Benjebbour, "Design considerations for a 5G network architecture," *IEEE Commun. Mag.*, vol. 52, no. 11, pp. 65–75, Nov. 2014. (cited on page 2)

[15] A. Asadi, Q. Wang, and V. Mancuso, "A survey on device-to-device communication in cellular networks," *IEEE Commun. Surveys Tuts.*, vol. 16, no. 4, pp. 1801–1819, Fourth quarter 2014. (cited on pages 2 and 14)

[16] M. N. Tehrani, M. Uysal, and H. Yanikomeroglu, "Device-to-device communication in 5G cellular networks: challenges, solutions, and future directions," *IEEE Commun. Mag.*, vol. 52, no. 5, pp. 86–92, May 2014. (cited on page 2)

[17] A. A. Nasir, X. Zhou, S. Durrani, and R. Kennedy, "Relaying protocols for wireless energy harvesting and information processing," *IEEE Trans. Wireless Commun.*, vol. 12, no. 7, pp. 3622–3636, Jul. 2013. (cited on pages 2 and 16)

[18] H. Tabassum, E. Hoassain, A. Ogundipe, and D. I. Kim, "Wireless-powered cellular networks: Key challenges and solution techniques," *IEEE Commun. Mag.*, vol. 53, no. 6, pp. 63–71, Jun. 2015. (cited on page 2)

[19] A. D. Wyner, "Shannon-theoretic approach to a Gaussian cellular multiple-access channel," *IEEE Trans. Inform. Theory*, vol. 40, no. 6, pp. 1713–1727, Nov. 1994. (cited on page 3)

[20] H. S. Dhillon, R. K. Ganti, F. Baccelli, and J. G. Andrews, "Modeling and analysis of k-tier downlink heterogeneous cellular networks," *IEEE J. Sel. Areas Commun.*, vol. 30, no. 3, pp. 550–560, Apr. 2012. (cited on page 4)

[21] H. ElSawy, E. Hossain, and M. Haenggi, "Stochastic geometry for modeling, analysis, and design of multi-tier and cognitive cellular wireless networks: A survey," *IEEE Commun. Surveys Tuts.*, vol. 15, no. 3, pp. 996–1019, Thirdquarter 2013. (cited on pages 4, 7, 8, 9, 52, and 105)

[22] D. Stoyan, W. Kendall, and J. Mecke, *Stochastic Geometry and Its Applications*, 2nd ed. John Wiley and Sons, 1996. (cited on pages 4 and 7)

[23] E. S. Sousa and J. A. Silvester, "Optimum transmission ranges in a direct-sequence spread-spectrum multihop packet radio network," *IEEE J. Sel. Areas Commun.*, vol. 8, no. 5, pp. 762–771, Jun. 1990. (cited on pages 4 and 10)

[24] M. Souryal, B. Vojcic, and R. L. Pickholtz, "Ad hoc, multihop CDMA networks with route diversity in a Rayleigh fading channel," in *Proc. IEEE MILCOM*, vol. 2, Oct. 2001, pp. 1003–1007. (cited on pages 4 and 10)

[25] J. Venkataraman, M. Haenggi, and O. Collins, "Shot noise models for outage and throughput analyses in wireless ad hoc networks," in *Proc. IEEE MILCOM*, Oct. 2006, pp. 1–7. (cited on pages 4 and 10)

[26] P. Cardieri, "Modeling interference in wireless ad hoc networks," *IEEE Commun. Surveys Tuts.*, vol. 12, no. 4, pp. 551–572, Fourthquarter 2010. (cited on pages 4 and 10)

[27] S. P. Weber, X. Yang, J. G. Andrew, and G. de Veciana, "Transmission capacity of wireless ad hoc networks with outage constraints," *IEEE Trans. Inform. Theory*, vol. 51, no. 12, pp. 4091–4102, Dec 2005. (cited on pages 4, 10, and 11)

[28] S. P. Weber, J. G. Andrews, and N. Jindal, "An overview of the transmission capacity of wireless networks," *IEEE Trans. Commun.*, vol. 58, no. 12, pp. 3593–3604, Dec. 2010. (cited on pages 4, 10, and 11)

[29] J. G. Andrews and S. P. Webber, *Transmission Capacity of Wireless Networks*. NOW: Foundations and Trends in Networking, 2012. (cited on pages 4, 10, and 11)

[30] S. P. Weber, J. G. Andrew, X. Yang, and G. de Veciana, "Transmission capacity of wireless ad hoc networks with successive interference cancellation," *IEEE Trans. Inform. Theory*, vol. 53, no. 8, pp. 2799–2814, Aug. 2007. (cited on pages 4 and 11)

[31] A. M. Hunter, J. G. Andrews, and S. P. Weber, "Transmission capacity of ad hoc networks with spatial diversity," *IEEE Trans. Wireless Commun.*, vol. 7, no. 12, pp. 5058–5071, Dec. 2008. (cited on pages 4, 11, 17, 27, 38, and 54)

[32] F. Baccelli and B. Blaszczyszyn, *Stochastic Geometry and Wireless Networks in Foundations and Trends in Networking*. NOW: Foundations and Trends in Networking, 2010. (cited on pages 4, 7, and 8)

[33] N. Jindal, S. P. Weber, and J. G. Andrews, "Fractional power control for decentralized wireless networks," *IEEE Trans. Wireless Commun.*, vol. 7, no. 12, pp. 5482–5492, Dec. 2008. (cited on pages 4 and 11)

[34] X. Zhang and M. Haenggi, "Random power control in Poisson networks," *IEEE Trans. Commun.*, vol. 60, no. 9, pp. 2602–2611, Sep. 2012. (cited on pages 4 and 11)

[35] X. Zhang and M. Haenggi, "Delay-optimal power control policies," *IEEE Trans. Wireless Commun.*, vol. 11, no. 10, pp. 3518–3527, Oct. 2012. (cited on pages 4 and 11)

[36] A. Ghasemi and E. S. Sousa, "Interference aggregation in spectrum-sensing cognitive wireless networks," *IEEE J. Sel. Topics Signal Process.*, vol. 2, no. 1, pp. 41–56, Feb. 2008. (cited on pages 4, 12, 50, and 51)

[37] M. G. Khoshkholgh, K. Navaie, and H. Yanikomeroglu, "Outage performance of the primary service in spectrum sharing networks," *IEEE Trans. Mobile Comput.*, vol. 12, no. 10, pp. 1955–1971, Aug. 2013. (cited on pages 4 and 12)

[38] C. han Lee and M. Haenggi, "Interference and outage in Poisson cognitive networks," *IEEE Trans. Wireless Commun.*, vol. 11, no. 4, pp. 1392–1401, Apr. 2012. (cited on pages 4, 12, 13, 50, and 59)

[39] N. Mahmood, F. Yilmaz, M. Alouini, and G. Oien, "Cognitive interference modeling with applications in power and admission control," in *Proc. IEEE DYSPAN*, Oct. 2012, pp. 434–439. (cited on pages 4, 5, 12, 13, 50, 53, 57, and 59)

[40] A. S. Kahlon, S. Periyalwar, H. Yanikomeroglu, and S. S. Szyszkowicz, "Outage in a cellular network overlaid with an ad hoc network: The uplink case," in *Proc. IEEE PIMRC*, Sep. 2011, pp. 588–592. (cited on page 4)

[41] X. Lin, J. G. Andrews, and A. Ghosh, "Spectrum sharing for device-to-device communication in cellular networks," *IEEE Trans. Wireless Commun.*, vol. 13, no. 12, pp. 6727–6740, Dec. 2014. (cited on pages 4, 14, 70, 71, and 80)

[42] Q. Ye, M. Al-Shalash, C. Caramanis, and J. G. Andrews, "Resource optimization in device-to-device cellular systems using time-frequency hopping," *IEEE Trans. Wireless Commun.*, vol. 13, no. 10, pp. 5467–5480, Oct. 2014. (cited on pages 4 and 14)

[43] X. Lin, R. Ratasuk, A. Ghosh, and J. G. Andrews, "Modeling, analysis, and optimization of multicast device-to-device transmissions," *IEEE Trans. Wireless Commun.*, vol. 13, no. 8, pp. 4346–4359, Aug. 2014. (cited on pages 4 and 14)

[44] S. Stefanatos, A. Gotsis, and A. Alexiou, "Operational region of D2D communications for enhancing cellular network performance," *IEEE Trans. Wireless Commun.*, vol. 14, no. 11, pp. 5984–5997, Nov. 2015. (cited on pages 4, 14, and 80)

[45] J. Liu, S. Zhang, H. Nishiyama, N. Kato, and J. Guo, "A stochastic geometry analysis of D2D overlaying multi-channel downlink cellular networks," in *Proc. IEEE INFOCOM*, Apr. 2015, pp. 46–54. (cited on pages 4 and 14)

[46] H. ElSawy, E. Hossain, and M.-S. Alouini, "Analytical modeling of mode selection and power control for underlay D2D communication in cellular networks," *IEEE Trans. Commun.*, vol. 62, no. 11, pp. 4147–4161, Nov. 2014. (cited on pages 4, 14, 70, 71, and 80)

[47] D. Marshall, S. Durrani, J. Guo, and N. Yang, "Performance comparison of device-to-device mode selection schemes," in *Proc. IEEE PIMRC*, Aug. 2015, pp. 1536–1541. (cited on pages 4, 14, 70, and 80)

[48] M. Peng, Y. Li, T. Q. S. Quek, and C. Wang, "Device-to-device underlaid cellular networks under Rician fading channels," *IEEE Trans. Wireless Commun.*, vol. 13, no. 8, pp. 4247–4259, Aug. 2014. (cited on pages 4 and 14)

[49] N. Lee, X. Lin, J. G. Andrews, and R. W. Heath, "Power control for D2D underlaid cellular networks: Modeling, algorithms, and analysis," *IEEE J. Sel. Areas Commun.*, vol. 33, no. 1, pp. 1–13, Jan. 2015. (cited on pages 4, 14, 70, and 80)

[50] G. George, K. Ratheesh, and A. L. Mungara, "An analytical framework for device-to-device communication in cellular networks," *IEEE Trans. Wireless Commun.*, vol. 14, no. 11, pp. 6297–6310, Nov. 2015. (cited on pages 4, 14, 70, and 80)

[51] Z. Ding and H. Poor, "Cooperative energy harvesting networks with spatially random users," *IEEE Signal Process. Lett.*, vol. 20, no. 12, pp. 1211–1214, Dec. 2013. (cited on pages 4, 15, and 16)

[52] I. Krikidis, "Simultaneous information and energy transfer in large-scale networks with-/without relaying," *IEEE Trans. Commun.*, vol. 62, no. 3, pp. 900–912, Mar. 2014. (cited on pages 4, 15, and 16)

[53] H. Xia, B. Natarajan, and C. Liu, "Feasibility of simultaneous information and energy transfer in LTE-A small cell networks," in *Proc. IEEE CCNC*, Jan. 2014, pp. 20–25. (cited on pages 4 and 15)

[54] S. Lee, R. Zhang, and K. Huang, "Opportunistic wireless energy harvesting in cognitive radio networks," *IEEE Trans. Wireless Commun.*, vol. 12, no. 9, pp. 4788–4799, Sep. 2013. (cited on pages 4, 15, and 16)

[55] K. Huang and V. K. N. Lau, "Enabling wireless power transfer in cellular networks: Architecture, modeling and deployment," *IEEE Trans. Wireless Commun.*, vol. 13, no. 2, pp. 902–912, Feb. 2014. (cited on pages 4, 15, and 16)

[56] I. Flint, X. Lu, N. Privault, D. Niyato, and P. Wang, "Performance analysis of ambient RF energy harvesting: A stochastic geometry approach," in *Proc. IEEE GLOBECOM*, Dec. 2014, pp. 1448–1453. (cited on pages 4, 15, and 16)

[57] S. Srinivasa and M. Haenggi, "Modeling interference in finite uniformly random networks," in *Proc. IEEE ITW*, Jun. 2007. (cited on pages 5, 11, 13, 17, 25, 34, 53, 54, and 57)

[58] S. Srinivasa and M. Haenggi, "Distance distributions in finite uniformly random networks: Theory and applications," *IEEE Trans. Veh. Technol.*, vol. 59, no. 2, pp. 940–949, Feb. 2010. (cited on pages 5, 11, 32, 35, and 107)

[59] J. Chen, M. Ding, and Q. T. Zhang, "Interference statistics and performance analysis of MIMO ad hoc networks in Binomial fields," *IEEE Trans. Veh. Technol.*, vol. 61, no. 5, pp. 2033–2043, Jun. 2012. (cited on pages 5 and 11)

[60] M. Vu, S. S. Ghassemzadeh, and V. Tarokh, "Interference in a cognitive network with beacon," in *Proc. IEEE WCNC*, Mar. 2008, pp. 876–881. (cited on pages 5, 12, and 53)

[61] M. Derakhshani and T. Le-Ngoc, "Aggregate interference and capacity-outage analysis in a cognitive radio network," *IEEE Trans. Veh. Technol.*, vol. 61, no. 1, pp. 196–207, Jan. 2012. (cited on pages 5, 12, 51, and 53)

[62] L. Vijayandran, P. Dharmawansa, T. Ekman, and C. Tellambura, "Analysis of aggregate interference and primary system performance in finite area cognitive radio networks," *IEEE Trans. Commun.*, vol. 60, no. 7, pp. 1811–1822, Jul. 2012. (cited on pages 5, 12, 13, 52, 53, 57, and 59)

[63] A. Rabbachin, T. Q. S. Quek, H. Shin, and M. Z. Win, "Cognitive network interference," *IEEE J. Sel. Areas Commun.*, vol. 29, no. 2, pp. 480–493, Jan. 2011. (cited on pages 5, 12, 13, 48, 50, 52, 53, 57, 58, and 59)

[64] E. Hossain, M. Rasti, H. Tabassum, and A. Abdelnasser, "Evolution towards 5G multi-tier cellular wireless networks: An interference management perspective," *IEEE Wireless Commun.*, vol. 21, no. 3, pp. 118–127, Jun. 2014. (cited on pages 5 and 13)

[65] Z. Khalid and S. Durrani, "Distance distributions in regular polygons," *IEEE Trans. Veh. Technol.*, vol. 62, no. 5, pp. 2363–2368, Jun. 2013. (cited on pages 6, 18, 32, 33, 35, 53, 56, 107, and 108)

[66] R. Pure and S. Durrani, "Computing exact closed-form distance distributions in arbitrarily-shaped polygons with arbitrary reference point," *The Mathematica Journal*, vol. 17, Jun. 2015. (cited on page 6)

[67] A. Goldsmith, S. A. Jafar, I. Maric, and S. Srinivasa, "Breaking spectrum gridlock with cognitive radios: An information theoretic perspective," *Proc. IEEE*, vol. 97, no. 5, pp. 894–914, May 2009. (cited on pages 6 and 12)

[68] J. G. Andrews, F. Baccelli, and R. K. Ganti, "A tractable approach to coverage and rate in cellular networks," *IEEE Trans. Commun.*, vol. 59, no. 11, pp. 3122–3134, Nov. 2011. (cited on page 7)

[69] M. Haenggi, J. G. Andrews, F. Baccelli, O. Dousse, and M. Franceschetti, "Stochastic geometry and random graphs for the analysis and design of wireless networks," *IEEE J. Sel. Areas Commun.*, vol. 27, no. 7, pp. 1029–1046, Sep. 2009. (cited on page 7)

[70] M. Haenggi and R. K. Gant, *Interference in Large Wireless Networks*. NOW: Foundations and Trends in Networking, 2009. (cited on pages 7, 8, 9, and 105)

[71] M. Haenggi, *Stochastic Geometry for Wireless Networks*. Cambridge University Press, 2012. (cited on pages 8, 29, 52, 71, 74, 77, 91, 92, 93, 94, 96, 97, and 122)

[72] P. Brémaud, *Mathematical Principles of Signal Processing: Fourier and Wavelet Analysis*. Springer, 2002. (cited on page 10)

[73] F. Baccelli, B. Blaszczyszyn, and P. Muhlethaler, "Stochastic analysis of spatial and opportunistic ALOHA," *IEEE J. Sel. Areas Commun.*, vol. 27, no. 7, pp. 1105–1119, Sep. 2009. (cited on page 11)

[74] R. Tanbourgi, H. Jäkel, and F. K. Jondral, "Interference and throughput in Poisson networks with isotropically distributed nodes," 2012, submitted. [Online]. Available: http://arxiv.org/abs/1211.4755 (cited on page 11)

[75] D. Torrieri and M. C. Valenti, "The outage probability of a finite ad hoc network in Nakagami fading," *IEEE Trans. Commun.*, vol. 11, no. 60, pp. 3509–3518, Dec. 2012. (cited on pages 11, 17, 25, 35, and 39)

[76] S. Kusaladharma and C. Tellambura, "Impact of beacon misdetection on aggregate interference for hybrid underlay-interweave networks," *IEEE Commun. Lett.*, vol. 17, no. 11, pp. 2052–2055, Nov. 2013. (cited on page 12)

[77] X. Jiang, K.-K. Wong, Y. Zhang, and D. Edwards, "On hybrid overlay-underlay dynamic spectrum access: Double-threshold energy detection and markov model," *IEEE Trans. Veh. Technol.*, vol. 62, no. 8, pp. 4078–4083, Oct. 2013. (cited on page 12)

[78] T. Chu, H. Phan, and H. Zepernick, "Hybrid interweave-underlay spectrum access for cognitive cooperative radio networks," *IEEE Trans. Commun.*, vol. 62, no. 7, pp. 2183–2197, Jul. 2014. (cited on page 12)

[79] Y. Chen and N. C. Beaulieu, "Performance of collaborative spectrum sensing for cognitive radio in the presence of Gaussian channel estimation errors," *IEEE Trans. Commun.*, vol. 57, no. 7, pp. 1944–1947, Jul. 2009. (cited on page 12)

[80] H. Li, H. Dai, and C. Li, "Collaborative quickest spectrum sensing via random broadcast in cognitive radio systems," *IEEE Trans. Wireless Commun.*, vol. 9, no. 7, pp. 2338–2348, Jul. 2010. (cited on page 12)

[81] M. G. Khoshkholgh, K. Navaie, and H. Yanikomeroglu, "Optimal design of the spectrum sensing parameters in the overlay spectrum sharing," *IEEE Trans. Mobile Comput.*, vol. 13, no. 9, pp. 2071–2085, Sep. 2014. (cited on page 12)

[82] C. Zhai, W. Zhang, and P. C. Ching, "Cooperative spectrum sharing based on two-path successive relaying," *IEEE Trans. Commun.*, vol. 61, no. 6, pp. 2260–2270, Jun. 2013. (cited on page 12)

[83] M. Chraiti, H. Hakim, W. Ajib, and H. Boujemaa, "Spectrum sharing techniques for broadcast cognitive radio networks," *IEEE Trans. Wireless Commun.*, vol. 12, no. 11, pp. 5880–5888, Nov. 2013. (cited on page 12)

[84] L. B. Le and E. Hossain, "Resource allocation for spectrum underlay in cognitive radio networks," *IEEE Trans. Wireless Commun.*, vol. 7, no. 12, pp. 5306–5315, Dec. 2008. (cited on pages 12 and 13)

[85] D. I. Kim, L. B. Le, and E. Hossain, "Joint rate and power allocation for cognitive radios in dynamic spectrum access environment," *IEEE Trans. Wireless Commun.*, vol. 7, no. 12, pp. 5517–5527, Dec. 2008. (cited on pages 12 and 13)

[86] T. Le and K. Navaie, "Downlink beamforming in underlay cognitive cellular networks," *IEEE Trans. Commun.*, vol. 62, no. 7, pp. 2212–2223, Jul. 2014. (cited on pages 12 and 13)

[87] E. Salbaroli and A. Zanella, "Interference analysis in a Poisson field of nodes of finite area," *IEEE Trans. Veh. Technol.*, vol. 58, no. 4, pp. 1776–1783, May 2009. (cited on page 13)

[88] J. Guo, S. Durrani, and X. Zhou, "Outage probability in arbitrarily-shaped finite wireless networks," *IEEE Trans. Commun.*, vol. 62, no. 2, pp. 699–712, Feb. 2014. (cited on pages 13, 18, 53, 54, 55, 56, 63, and 73)

[89] X. Lin, J. G. Andrews, A. Ghosh, and R. Ratasuk, "An overview of 3GPP device-to-device proximity services," *IEEE Commun. Mag.*, vol. 52, no. 4, pp. 40–48, Apr. 2014. (cited on pages 13 and 70)

[90] A. Altieri, P. Piantanida, L. Vega, and C. G. Galarza, "On fundamental trade-offs of device-to-device communications in large wireless networks," *IEEE Trans. Wireless Commun.*, vol. 14, no. 9, pp. 4958–4971, Sep. 2015. (cited on page 13)

[91] A. Osseiran, K. Doppler, C. Ribeiro, M. Xiao, M. Skoglund, and J. Manssour, "Advances in device-to-device communications and network coding for IMT-advanced," in *Proc. ICT Mobile Summit*, Jun. 2009, pp. 1–8. (cited on pages 14 and 70)

[92] P. Janis, V. Koivunen, C. Ribeiro, J. Korhonen, K. Doppler, and K. Hugl, "Interference-aware resource allocation for device-to-device radio underlaying cellular networks," in *Proc. IEEE VTC-Spring*, Apr. 2009, pp. 1–5. (cited on page 14)

[93] R. Zhang and C. K. Ho, "MIMO broadcasting for simultaneous wireless information and power transfer," *IEEE Trans. Wireless Commun.*, vol. 12, no. 5, pp. 1989–2001, May 2013. (cited on pages 14, 16, and 70)

[94] G. Yu, L. Xu, D. Feng, R. Yin, G. Y. Li, and Y. Jiang, "Joint mode selection and resource allocation for device-to-device communications," *IEEE Trans. Commun.*, vol. 62, no. 11, pp. 3814–3824, Nov. 2014. (cited on pages 14, 70, and 80)

[95] M. Sheng, Y. Li, X. Wang, J. Li, and Y. Shi, "Energy efficiency and delay tradeoff in device-to-device communications underlaying cellular networks," *IEEE J. Sel. Areas Commun.*, vol. 34, no. 1, pp. 92–106, Jan. 2016. (cited on pages 14 and 70)

[96] H. Min, W. Seo, J. Lee, S. Park, and D. Hong, "Reliability improvement using receive mode selection in the device-to-device uplink period underlaying cellular networks," *IEEE Trans. Wireless Commun.*, vol. 10, no. 2, pp. 413–418, Feb. 2011. (cited on pages 14 and 70)

[97] C.-H. Yu, K. Doppler, C. B. Ribeiro, and O. Tirkkonen, "Resource sharing optimization for device-to-device communication underlaying cellular networks," *IEEE Trans. Wireless Commun.*, vol. 10, no. 8, pp. 2752–2763, Aug. 2011. (cited on pages 14, 70, and 80)

[98] M. Ni, L. Zheng, F. Tong, J. Pan, and L. Cai, "A geometrical-based throughput bound analysis for device-to-device communications in cellular networks," *IEEE J. Sel. Areas Commun.*, vol. 33, no. 1, pp. 100–110, Jan. 2015. (cited on pages 14, 70, and 80)

[99] W. Cheng, X. Zhang, and H. Zhang, "Optimal power allocation with statistical QoS provisioning for D2D and cellular communications over underlaying wireless networks," *IEEE J. Sel. Areas Commun.*, vol. 34, no. 1, pp. 151–162, Jan. 2016. (cited on pages 14, 70, and 80)

[100] L. R. Varshney, "Transporting information and energy simultaneously," in *Proc. IEEE ISIT*, Jun. 2008, pp. 1612–1616. (cited on page 15)

[101] P. Grover and A. Saha, "Shannon meets tesla: Wireless information and power transfer," in *Proc. IEEE ISIT*, Jun. 2010, pp. 2363–2367. (cited on page 15)

[102] X. Lu, P. Wang, D. Niyato, D. I. Kim, and Z. Han, "Wireless networks with RF energy harvesting: A contemporary survey," *IEEE Commun. Surveys Tuts.*, vol. 17, no. 2, pp. 757–789, Secondquarter 2015. (cited on pages 15, 16, 21, 90, and 97)

[103] K. Huang and X. Zhou, "Cutting last wires for mobile communication by microwave power transfer," *IEEE Commun. Mag.*, vol. 53, no. 6, pp. 86–93, Jun. 2015. (cited on pages 15 and 16)

[104] Z. Ding, I. Krikidis, B. Sharif, and H. V. Poor, "Wireless information and power transfer in cooperative networks with spatially random relays," *IEEE Trans. Wireless Commun.*, vol. 13, no. 8, pp. 4440–4453, Aug. 2014. (cited on pages 15 and 16)

[105] H. Ju and R. Zhang, "Throughput maximization in wireless powered communication networks," *IEEE Trans. Wireless Commun.*, vol. 13, no. 1, pp. 418–428, Jan. 2014. (cited on pages 15 and 16)

[106] H. Chen, Y. Li, J. L. Rebelatto, B. F. Uchoa-Filhoand, and B. Vucetic, "Harvest-then-cooperate: Wireless-powered cooperative communications," *IEEE Trans. Signal Process.*, vol. 63, no. 7, pp. 1700–1711, Apr. 2015. (cited on pages 15 and 16)

[107] M. Erol-Kantarci and H. T. Mouftah, "Radio-frequency-based wireless energy transfer in LTE-A heterogenous networks," in *Proc. IEEE ISCC*, Jun. 2014. (cited on page 16)

[108] J. Abate and W. Whitt, "Numerical inversion of Laplace transforms of probability distributions," *ORSA J. Compt.*, vol. 7, no. 1, pp. 36–43, 1995. (cited on pages 17, 25, and 39)

[109] Y.-C. Ko, M.-S. Alouini, and M. K. Simon, "Outage probability of diversity systems over generalized fading channels," *IEEE Trans. Commun.*, vol. 48, no. 11, pp. 1789–1787, Nov. 2000. (cited on pages 17 and 25)

[110] J. Guo, S. Durrani, and X. Zhou, "Performance analysis of arbitrarily-shaped underlay cognitive networks: Effects of secondary user activity protocols," *IEEE Trans. Commun.*, vol. 63, no. 2, pp. 376–389, Feb. 2015. (cited on page 19)

[111] B. Kaufman and B. Aazhang, "Cellular networks with an overlaid device to device network," in *Proc. Asilomar Conf. Signals, Syst. Comput.*, Oct. 2008, pp. 1537–1541. (cited on pages 19 and 71)

[112] T. Peng, Q. Lu, H. Wang, S. Xu, and W. Wang, "Interference avoidance mechanisms in the hybrid cellular and device-to-device systems," in *Proc. IEEE PIMRC*, Sep. 2009, pp. 617–621. (cited on pages 19 and 71)

[113] J. Guo, S. Durrani, X. Zhou, and H. Yanikomeroglu, "Device-to-device communication underlaying a finite cellular network region," 2015 (submitted). [Online]. Available: http://arxiv.org/abs/1510.03162 (cited on page 20)

[114] J. Guo, S. Durrani, X. Zhou, and H. Yanikomeroglu, "Outage probability of ad hoc networks with wireless information and power transfer," *IEEE Wireless Commun. Lett.*, vol. 4, no. 4, pp. 409–412, Aug. 2015. (cited on page 21)

[115] M. K. Simon and M.-S. Alouini, *Digital Communication over Fading Channels*, 2nd ed. Wiley, 2005. (cited on pages 24, 29, 48, 52, 53, 54, and 73)

[116] H. Inaltekin, M. Chiang, H. V. Poor, and S. B. Wicker, "On unbounded path-loss models: effects of singularity on wireless network performance," *IEEE J. Sel. Areas Commun.*, vol. 27, no. 7, pp. 1078–1092, Sep. 2009. (cited on page 24)

[117] S. P. Weber, J. G. Andrews, and N. Jindal, "The effect of fading, channel inversion, and threshold scheduling on ad hoc networks," *IEEE Trans. Inform. Theory*, vol. 53, no. 11, pp. 4127–4149, Nov. 2007. (cited on page 24)

[118] C. A. O'Cinneide, "Euler summation for Fourier series and Laplace transform inversion," *Commun. Statist. -Stochastic Models*, pp. 315–337, 1997. (cited on pages 26 and 39)

[119] M. Yacoub, "The $\kappa - \mu$ and the $\eta - \mu$ distribution," *IEEE Antennas Propag. Mag.*, vol. 49, no. 1, pp. 68–81, Feb. 2007. (cited on page 27)

[120] S. Al-Ahmadi and H. Yanikomeroglu, "On the approximation of the generalized-K distribution by a Gamma distribution for modeling composite fading channels," *IEEE Trans. Wireless Commun.*, vol. 9, no. 2, pp. 706–713, Feb. 2010. (cited on pages 27 and 91)

[121] F. Yilmaz and M.-S. Alouini, "A new simple model for composite fading channels: Second order statistics and channel capacity," in *Proc. ISWCS*, Sep. 2010, pp. 676–680. (cited on page 27)

[122] A. S. Kahlon, S. S. Szyszkowicz, S. Periyalwar, and H. Yanikomeroglu, "Separating the effect of independent interference sources with Rayleigh faded signal link: Outage analysis and applications," *IEEE Wireless Commun. Lett.*, vol. 1, no. 5, pp. 409–411, 2012. (cited on page 27)

[123] R. V. Hogg and A. T. Craig, *Introduction to Mathematical Statistics*, 6th ed. Pearson, 2004. (cited on pages 27 and 30)

[124] M. Abramowitz and I. Stegun, *Handbook of Mathematical Functions with Formulas, Graphs, and Mathematical Tables*, 2nd ed. New York: Dover, 1972. (cited on page 28)

[125] E. W. Weisstein. (2013) Multinomial series. [Online]. Available: http://mathworld.wolfram.com/MultinomialSeries.html (cited on page 28)

[126] F. B. Hildebrand, *Introduction to Numerical Analysis*, 2nd ed. McGraw-Hill, 1974. (cited on page 34)

[127] N. C. Beaulieu and S. S. Soliman, "Exact analysis of multihop amplify-and-forward relaying systems over general fading links," *IEEE Trans. Commun.*, vol. 60, no. 8, pp. 2123–2134, Aug. 2012. (cited on page 38)

[128] A. Abu-Dyya and N. C. Beaulieu, "Outage probabilities of cellular mobile radio systems with multiple Nakagami interferers," *IEEE Trans. Veh. Technol.*, vol. 40, pp. 757–767, Nov. 1991. (cited on page 41)

[129] C. Tellambura, "Cochannel interference computation for arbitrary Nakagami fading," *IEEE Trans. Veh. Technol.*, vol. 48, no. 2, pp. 487–489, Mar. 1999. (cited on page 41)

[130] S. Weber, J. G. Andrews, and N. Jindal, "An overview of the transmission capacity of wireless networks," *IEEE Trans. Commun.*, vol. 58, no. 12, pp. 3593–3604, Dec. 2010. (cited on page 44)

[131] M. Vu, N. Devroye, and V. Tarokh, "On the primary exclusive region of cognitive networks," *IEEE Trans. Wireless Commun.*, vol. 8, no. 7, pp. 3380–3385, Jul. 2009. (cited on page 48)

[132] S. Akoum and R. W. Heath, "Interference coordination: Random clustering and adaptive limited feedback," *IEEE Trans. Signal Process.*, vol. 61, no. 7, pp. 1822–1834, Apr. 2013. (cited on page 51)

[133] H. Wymeersch, J. Lien, and M. Z. Win, "Cooperative localization in wireless networks," *Proc. IEEE*, vol. 97, no. 2, pp. 427–450, Feb. 2009. (cited on page 51)

[134] M. Nakagami, *The m-Distribution, a general formula of intensity of rapid fading*, I. W. C. Hoffman, Ed. Pergamon Press, 1960. (cited on page 53)

[135] J. Guo, S. Durrani, and X. Zhou, "Characterization of aggregate interference in arbitrarilyshaped underlay cognitive networks," in *Proc. IEEE GLOBECOM*, Dec. 2014, pp. 961–966. (cited on page 54)

[136] W. L. Martinez and A. R. Martinez, *Computational Statistics Handbook with Matlab*. Chapman and Hall/CRC, 2001. (cited on page 61)

[137] Z. Liu, T. Peng, S. Xiang, and W. Wang, "Mode selection for device-to-device (D2D) communication under LTE-advanced networks," in *Proc. IEEE ICC*, Jun. 2012, pp. 5563–5567. (cited on page 71)

[138] P. Phunchongharn, E., Hossain, and D. I. Kim, "Resource allocation for device-to-device communications underlaying LTE-advanced networks," *IEEE Trans. Wireless Commun.*, vol. 20, no. 4, pp. 91–100, Aug. 2013. (cited on page 71)

[139] P. Mach, Z. Becvar, and T. Vanek, "In-band device-to-device communication in OFDMA cellular networks: A survey and challenges," *IEEE Commun. Surveys Tuts.*, vol. 17, no. 4, pp. 1885–1922, Fourthquarter 2015. (cited on page 71)

[140] E. W. Weisstein, "Circle-circle intersection," *MathWorld*. [Online]. Available: http://mathworld.wolfram.com/Circle-CircleIntersection.html (cited on page 77)

[141] S. Ali, N. Rajatheva, and M. Latva-aho, "Full duplex device-to-device communication in cellular networks," in *Proc. EuCNC*, Jun. 2014, pp. 1–5. (cited on page 80)

[142] L. Wei, R. Q. Hu, Y. Qian, and G. Wu, "Energy efficiency and spectrum efficiency of multihop device-to-device communications underlaying cellular networks," *IEEE Trans. Veh. Technol.*, vol. 65, no. 1, pp. 367–380, Jan. 2016. (cited on page 80)

[143] A. Al-Hourani, S. Kandeepan, and A. Jamalipour, "Stochastic geometry study on device-to-device communication as a disaster relief solution," *IEEE Trans. Veh. Technol.*, vol. 65, no. 5, pp. 3005–3017, May 2016. (cited on page 80)

[144] X. Zhang and J. G. Andrews, "Downlink cellular network analysis with multi-slope path loss models," *IEEE Trans. Commun.*, vol. 63, no. 5, pp. 1881–1894, May 2015. (cited on page 80)

[145] X. Zhou, R. Zhang, and C. K. Ho, "Wireless information and power transfer: Architecture design and rate-energy tradeoff," *IEEE Trans. Commun.*, vol. 61, no. 11, pp. 4754–4767, Nov. 2013. (cited on page 90)

[146] Y. Gu, H. Chen, Y. Li, and B. Vucetic, "Distributed multi-relay selection in accumulate-then-forward energy harvesting relay networks," 2016 (submitted). [Online]. Available: http://arxiv.org/abs/1602.00339 (cited on page 105)

[147] A. Al-Fuqaha, M. Guizani, M. Mohammadi, M. Aledhari, and M. Ayyash, "Internet of things: A survey on enabling technologies, protocols, and applications," *IEEE Commun. Surveys Tuts.*, vol. 17, no. 4, pp. 2347–2376, Fourthquarter 2015. (cited on page 105)

[148] D. Malak, H. S. Dhillon, and J. G. Andrews, "Optimizing data aggregation for uplink machine-to-machine communication networks," *IEEE Trans. Commun.*, vol. 64, no. 3, pp. 1274–1290, Mar. 2016. (cited on page 105)

[149] E. Björnson, E. G. Larsson, and T. L. Marzetta, "Massive MIMO: ten myths and one critical question," *IEEE Commun. Mag.*, vol. 54, no. 2, pp. 114–123, Feb. 2016. (cited on page 105)

[150] T. S. Rappaport, S. Sun, R. Mayzus, H. Zhao, Y. Azar, K. Wang, G. N. Wong, J. K. Schulz, M. Samimi, and F. Gutierrez, "Millimeter wave mobile communications for 5G cellular: It will work!" *IEEE Access*, vol. 1, pp. 335–349, May 2013. (cited on page 105)

[151] R. K. Ganti and M. Haenggi, "Interference and outage in clustered wireless ad hoc networks," *IEEE Trans. Inform. Theory*, vol. 55, no. 9, pp. 4067–4086, Sep. 2009. (cited on page 105)

[152] I. S. Gradshteyn and I. M. Ryzhik, *Table of Integrals, Series, and Products*, 7th ed. Academic Press, 2007. (cited on pages 118, 119, 120, and 121)

[153] T. Bai and R. W. Heath, "Coverage and rate analysis for millimeter-wave cellular networks," *IEEE Trans. Wireless Commun.*, vol. 14, no. 2, pp. 1100–1114, Feb. 2015. (cited on page 125)

[154] H. Alzer, "On some inequalities for the incomplete Gamma function," *Math. Comput.*, vol. 66, no. 218, pp. 771–778, Apr. 1997. (cited on page 125)